Washington University in St. Louis

Washington University Open Scholarship

Summer 8-15-2019

Joint Reconstruction for Single-Shot Edge Illumination Phase-Contrast Tomography (EIXPCT)

Yujia Chen
Washington University in St. Louis

Follow this and additional works at: https://openscholarship.wustl.edu/eng_etds

Part of the Biomedical Engineering and Bioengineering Commons

WASHINGTON UNIVERSITY IN ST.LOUIS

McKelvey School of Engineering
Department of Biomedical Engineering

Dissertation Examination Committee:
Yuan-Chuan Tai, Chair
Mark A. Anastasio, Co-Chair
Abhinav Jha
Joseph O'Sullivan
Tiezhi Zhang

Joint Reconstruction for Single-Shot Edge Illumination Phase-Contrast Tomography
(EIXPCT)
by
Yujia Chen

A dissertation presented to
The Graduate School
of Washington University in
partial fulfillment of the
requirements for the degree
of Doctor of Philosophy

August 2019
St. Louis, Missouri

Table of Contents

List of Figures

vii

xi

List of Tables

Acknowledgments

Throughout the process of writing the thesis, I have received tremendous help and support from a lot of people. I would first like to thank my advisor, Dr. Mark A. Anastasio, for his insightful guidance and considerate help during every phase of my research training. His expertise was crucial for helping me select the research directions.

I need to thank all the professors who have helped during the entire process, especially Dr. Alessandro Olivo from the University of College London along with his lab members. They helped me understand the core concepts and kindly provided us with experimental datasets for many of my dissertation projects. Dr. Olivo also provided valuable feedback on our co-authored papers and I am truly grateful for that. I also would like to thank all my committee members, who have provided me with valuable comments for my research directions. A special thanks goes to the McDonnell International Scholars Academy, for supporting me financially for my five years of PhD study.

I also want to acknowledge all of my labmates for their helpful discussions throughout all these years. I would like to express my special gratitude to Dr. Kun Wang and Dr. Yang Lou, who have offered me great guidance and help when I was struggling with the challenging projects. Moreover, I would like to thank James Ballard from the writing center for polishing part of my manuscripts.

Finally, I want to thank my husband Zhichao Li and my parents for their support and encouragement. They have accompanied me through all the ups and downs. I am truly grateful.

<div align="right">Yujia Chen</div>

Dedicated to my parents and my husband.

ABSTRACT OF THE DISSERTATION

Joint Reconstruction for Single-Shot Edge Illumination Phase-Contrast Tomography

(EIXPCT)

by

Yujia Chen

Doctor of Philosophy in Biomedical Engineering

Washington University in St. Louis, 2019

Professor Yuan-Chuan Tai, Chair

Professor Mark A. Anastasio, Co-Chair

Edge illumination X-ray phase-contrast tomography (EIXPCT) is an emerging X-ray phase-contrast tomography technique for estimating the complex-valued X-ray refractive index distribution of an object with laboratory-based X-ray sources. Conventional image reconstruction approaches for EIXPCT require multiple images to be acquired at each tomographic view angle. This contributes to prolonged data-acquisition times and elevated radiation doses, which can hinder *in vivo* applications. In this dissertation, a new "single-shot" method without restrictive assumptions related to the object, imaging geometry or hardware is proposed for joint reconstruction (JR) of the real and imaginary-valued components of the refractive index distribution from a tomographic data set that contains only a single image acquired at each view angle. The proposed method is predicated upon a non-linear formulation of the inverse problem that is solved by use of a gradient-based optimization method. The potential usefulness of this method is validated and investigated by use of computer-simulated and experimental EIXPCT data sets. The convexity, cross-talk properties and noise properties of the JR method are also investigated.

One important advantage of EIXPCT is that its flexibility enables novel flexible data-acquisition designs. In this dissertation, two aspects of data-acquisition designs are explored in two separate studies. The first study focuses on where the masks in EIXPCT should be placed during the data-acquisition process. In this study, several promising mask displacement strategies are proposed, such as the constant aperture position (CAP) strategy and the alternating aperture position (AAP) strategies covering different angular ranges. In computer-simulation studies, candidate designs are analyzed and compared in terms of image reconstruction stability and quality. Experimental data are employed to test the designs in real-world applications. All candidate designs are also compared for their implementation complexity. The tradeoff between data acquisition time and image quality is discussed.

The second study focuses on a resolution-enhancement method called dithering. Dithering requires that multiple projection images per tomographic view angle are acquired as the object is moved over sub-pixel distances. The EIXPCT resolution is mainly determined by the grating period of a sample mask, but can be significantly improved by the dithering technique. However, one main drawback of dithering is the increased data-acquisition time. Motivated by the flexibility in data acquisition designs enabled by the JR method, a novel partial dithering strategy for data acquisition is proposed. In this strategy, dithering is implemented at only a subset of the tomographic view angles. This results in spatial resolution that is comparable to that of the conventional full dithering strategy where dithering is performed at every view angle, but the acquisition time is substantially decreased. The effect of dithering parameters on image resolution is explored.

Finally, a bench-top EIXPCT system has been set up in the lab. The components are designed to address the need of *in vivo* imaging of small animal models. However, thick objects such as animals pose unique challenges for the EIXPCT system, including the potential phase-wrapping problem, limited signal sensitivity, and elevated noise. The components of

the system are designed to tackle these challenges, and some initial images obtained from the system show promising potential.

Chapter 1

Introduction

1.1 X-ray phase contrast imaging systems

X-ray phase-contrast tomography (XPCT) is a novel imaging technology utilized to estimate the complex-valued refractive index distribution of an imaged object. The complex-valued refractive index is defined to be $n = 1 - \delta + i\beta$, where δ denotes the refractive index decrement distribution and β denotes the absorption distribution. Compared with traditional CT, which reveals only absorption distribution, β, XPCT utilizes coherent X-rays so that the refractive index information will also be encoded in the measured intensities as interference fringes. Monochromatic X-ray beam with high spatial coherence from a synchrotron radiation (SR) facility is the ideal choice as the source. XPCT system takes advantage of most biological soft tissues' higher contrast of refractive index decrement distributions in comparison to that of absorption distributions. Its sensitivity to both absorption and refraction makes it a powerful tool for visualizing soft tissues due to better soft tissue differentiability.

The refractive index decrement, δ, induces phase shift of X-ray wavefront, which is not directly detectable. Extra setup is also required to encode the phase shift information into detectable wave intensity changes. Depending on the mechanism for encoding phase information, XPCT can be classified into different types.

One typical XPCT system is propagation-base X-ray phase-contrast tomography (PBXPCT) [13, 49, 57]. The X-ray will propagate in free space after interacting with the object to encode the phase information in the detectable intensities. PBXPCT is straight-forward to implement and has relatively weak requirement on source temporal coherence. However, PBXPCT still has strict constraint on the spatial coherence of the radiation source, thus a laboratory-based PBXPCT system usually has to be implemented by a spatially-coherent source like micro-focus X-ray source, and the exposure time can be long due to the limited source power [11, 47].

Another type of XPCT is grating-based X-ray phase-contrast tomography (GBXPCT) [31, 47, 56, 63], which obtains phase information with a grating or shearing interferometer. GBXPCT in general also requires spatial coherence. This requirement may be mitigated by use of an absorption grid placed in close contact with the source [31], but the extra absorption grid may result in longer exposure times. These limitations prevent GBXPCT systems from being of practical use in realistic situations outside the research domain [43].

1.2 Edge-illumination X-ray phase-contrast tomography (EIXPCT) and conventional reconstruction method

Edge illumination X-ray phase-contrast tomography (EIXPCT) is a novel XPCT technology [18, 36, 42, 43, 60]. Among all the XPCT technologies, EIXPCT have relative weak

requirements about both temporal and spatial coherence of the source without additional source grating or collimation [36, 37], so it can be set up with conventional laboratory-based X-ray sources, and still requires relatively short data-acquisition times.

The conventional EIXPCT system setup [36, 60] is shown in Fig. 2.1. The incident X-ray beam from the source is partially blocked by a sample mask. Then, the beam interacts with the object immediately following the sample mask. This process creates phase shifts in the wavefront, which can also be interpreted as refraction of the X-ray beam in geometric optics. After propagation in free space, the X-ray beam is either blocked by the detector mask or detected by the detector. A refracted beam component thus can be either detected or undetected depending on the positions of the two blocking masks. Consequently, the information about refraction angles is encoded in the measurement data. Because the refraction angle is proportional to the first-order derivative of the phase shift [42], the phase information can be retrieved afterwards.

Conventional reconstruction methods for EIXPCT employ a two-step strategy [18, 36]. First, a phase retrieval step is implemented by processing two or more measured intensity images acquired as described above to separate refractive index distribution information from absorption distribution information and obtain the sinograms of both distributions. In the second step, tomographic image reconstruction methods are employed to estimate independently the distributions of both β and δ based on the sinograms from the first step. The most common choice is the filtered back projection (FBP) method. Due to the nature of this approach, at least two images are acquired at each tomographic view angle, which prolongs data-acquisition times and potentially increases the imaging dose.

1.3 Single-shot EIXPCT imaging methods

To simplify and speed up the data-acquisition process, single-shot methods that require only one image per tomographic view angle are highly desirable [10, 12, 60]. Several different methods for single-shot EIXPCT have been proposed.

Some methods exploit special hardware so that with one X-ray exposure, it is possible to obtain information equivalent to that of multiple images. Das et al. proposed a method that employs a polychromatic X-ray source and an energy-sensitive detector [10]. If there are N energy bins, then effectively N images are obtained for one X-ray exposure, compensating for the loss of information normally provided from other mask positions. Endrizzi et. al. presented a similar idea utilizing specially fabricated, "multi-way" masks [16]. The conventional mask places the absorbing septa periodically with equal gaps between any neighboring septa, while the multi-way mask has multiple groups of absorbing septa with equal gaps within each group but non-uniform gaps between groups. The absorbing septa are designed to have a one-to-one correspondence with the detector pixels, so different pixels in the measured image obtained by single-shot imaging can be divided and regrouped into multiple images based on their corresponding septa group, thus achieving the effect of acquiring multiple images per X-ray exposure. These methods can be effective, but their special hardware requirements add to the cost and complexity of the system.

Other single-shot methods employing the basic system setup are available, but they rely on specific assumptions about the object or imaging geometry. For example, the reverse projection technique [19] designed by Hagen et al. makes use of the conjugate-view symmetry in a parallel beam tomography geometry. However, it is not applicable to more general imaging geometries like the widely employed fan-beam and cone-beam geometries. For general geometries, Diemoz et. al. proposed the single-shot reconstruction method that considers

the ratio of the refractive index (δ) and absorption (β) to be a constant for the entire object [12, 14]. The quasi-homogeneous assumption is useful for single-material objects or objects containing multiple materials with similar δ/β ratios, but may fail for complex compositions of materials with vastly varying δ/β ratios. To address this problem, Zamir et al. recently proposed a new reconstruction method capable of reconstructing multi-material objects [59]. However, this method still relies on the prior knowledge of all the materials constituting the object. The method also assumes that one material is encased by another and that the encasing material has a slowly varying projected thickness.

1.4   Outlines for the dissertation

To address the above limitations, in this dissertation, a joint reconstruction (JR) method is proposed that can estimate the complex-valued refractive index from a tomographic data set that contains only a single image acquired at each view angle, which could reduce data-acquisition times and radiation doses, and also potentially allow *in vivo* imaging.

In Chapter 2, I will first review the imaging system and previous reconstruction methods for EIXPCT. In Chapter 3, I will introduce the JR method and will demonstrate its ability of reducing data-acquisition time using both simulation studies and experimental validation. Chapter 4 will provide a more detailed analysis about the numerical properties of the JR method, including convexity, cross-talk effect and noise property.

In Chapter 5 and Chapter 6, I will take advantage of the data-acquisition flexibility provided by the JR algorithm and propose a variety of data-acquisition designs. I will investigate how the reconstructed image quality can be affected by the data-acquisition designs when the JR method is employed. Chapter 5 focuses on the mask displacement strategy, and Chapter 6 focuses on the dithering strategy. Dithering is a technique mainly to help improve

reconstruction resolution. I will introduce the dithering technique in detail and will propose a way to optimize dithering strategy with the help of the JR method.

Moreover, in Chapter 7, I will discuss the design and implementation of an EIXPCT system for an *in vivo* thick-object imaging application. Images of artificial phantoms as well as biological samples will be presented to showcase the system's capability of material differentiation with δ images.

Finally, Chapter 8 will give a summary of the entire dissertation.

Chapter 2

Background

2.1 Edge-illumination X-ray phase-contrast imaging system

A canonical EIXPCT system is depicted in Figure 2.1 [18, 36, 42, 60]. The coordinate $\boldsymbol{r} = (x, y)$ describes a stationary reference coordinate system. We define the stationary coordinate system so that the x-axis is perpendicular to the two masks, while the y-axis is parallel to them. The origin of the reference system corresponds to the assumed origin of tomographic scanning.

A sample mask (or sample aperture) denoted by A_1 is placed between the X-ray source S and the to-be-imaged object that is denoted by O. The object's absorption distribution is denoted as $\beta(\boldsymbol{r})$ and refractive index decrement distribution is denoted as $\delta(\boldsymbol{r})$. The distance from the source to A_1 is denoted as l_{so}. A detector mask (or detector aperture), denoted by A_2, is located immediately in front of the detector and is parallel to the pre-sample mask A_1 and is
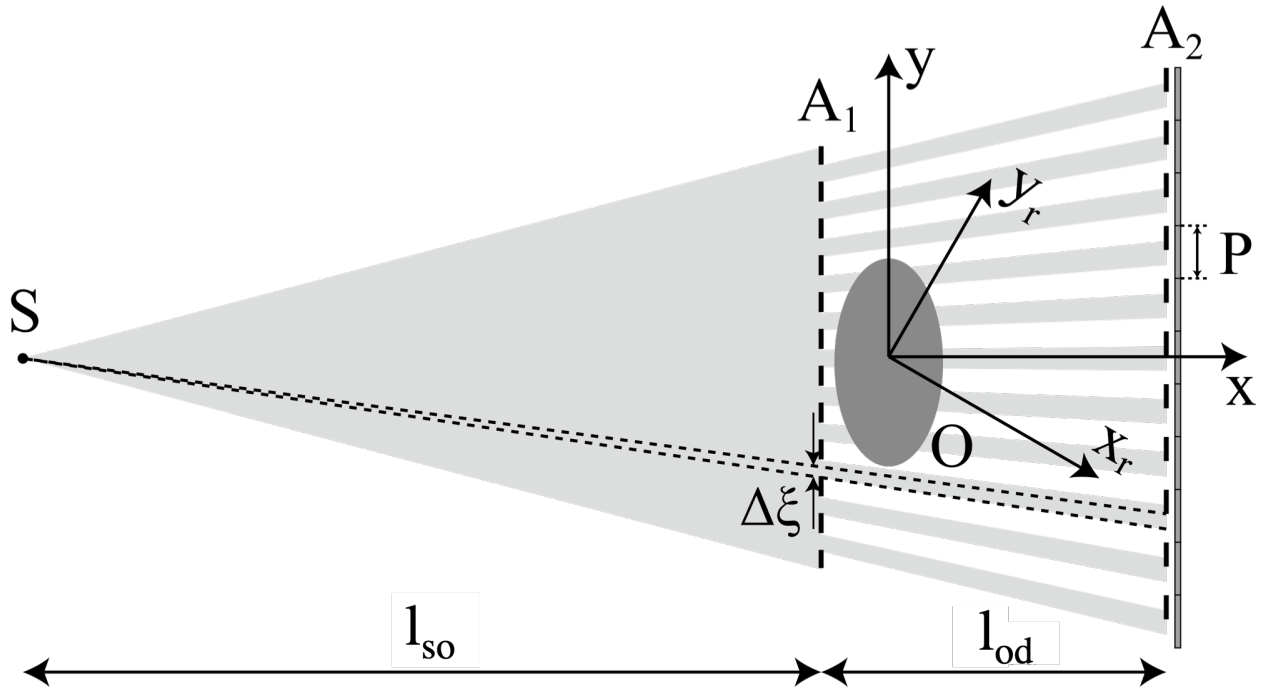
Figure 2.1: A typical experimental setup for an EIXPCT system. S is the X-ray source. Two masks are employed: one sample mask denoted by A_1, and one detector mask denoted by A_2 that has exactly the same period as the detector's pixel size P. The distance between the sample mask and the source is denoted by l_{so}, and that between the detector and the sample mask is denoted by l_{od}. The object can be rotated and the tomographic view angle is denoted by θ. The detector pixel's location is denoted by d. The sample mask A_1 can be moved vertically and the relative position of the sample mask to the detector mask is described by $\Delta\xi$.

at a distance l_{od} from it. The incident X-ray beam from the source is partially blocked by a sample mask. Then, the beam interacts with the object immediately following the sample mask. This process creates phase shifts in the wavefront, which can also be interpreted as refraction of the X-ray beam in geometric optics. After propagation in free space, the X-ray beam is either blocked by the detector mask or detected by the detector. A refracted beam component thus can be either detected or undetected depending on the positions of the two blocking masks. Consequently, the information about refraction angles is encoded in the measurement data. The relative positions of the two masks along the y_r-axis can be changed by moving the sample mask. Translating A_1 by $\Delta\xi$ results in the measurement of different deflected X-ray beam components. In this way, the differential phase information is encoded in the measured X-ray wave intensity, and thus can be retrieved afterwards.

2.2 EIXPCT imaging physics

The imaging process can be modeled based on wave optics [36]. Firstly, we model the transmission of the two masks. Denote the absorption coefficient of the mask material to be μ_{ca}. A common choice for the material is gold. For a sample mask A_1 with the thickness of T_1 and a period of P_1, the transmission properties are described as

$$\mathcal{T}_1(y + nP_1) = \begin{cases} 1 & |y| < \eta_1 P_1/2 \\ \exp(-\mu_{ca}T_1) & \text{otherwise} \end{cases}. \tag{2.1}$$

For the detector mask A_2, the thickness is denoted as T_2 and its period is designed to be the same as the detector pitch P. The transmission properties are described as

$$\mathcal{T}_2(y + nP) = \begin{cases} 1 & |y| < \eta_2 P/2 \\ \exp(-\mu_{ca}T_2) & \text{otherwise} \end{cases}. \tag{2.2}$$

9

Firstly, consider a monochromatic source where the wavelength of the incident X-ray beam is λ and the incident wavefield is U_0. The model will be generalized to a polychromatic source later. A transmittance function can be employed to describe the interaction between the X-ray and the imaged object:

$$T(y) = \exp\left(-\frac{2\pi}{\lambda}B(y)\right)\exp\left(-i\frac{2\pi}{\lambda}\psi(y)\right),\qquad(2.3)$$

where

$$B(y) = \int \beta(x,y)dx,\qquad(2.4)$$

and

$$\psi(y) = \int \delta(x,y)dx.\qquad(2.5)$$

The wavefield at the detector plane can be derived based on a paraxial approximation to the Fresnel-Kirchhoff diffraction integral [35, 36]:

$$U(y) = C\int_{-\infty}^{\infty}\sqrt{\mathcal{T}_1(M(\xi-\Delta\xi))}T(\xi)\exp\left(i\frac{\pi\xi^2}{\lambda}\frac{l_{so}+l_{od}}{l_{so}l_{od}}\right)\exp\left(-i\frac{2\pi\xi y}{\lambda l_{od}}\right)d\xi,\qquad(2.6)$$

where M denotes the magnification coefficient that is defined to be $(l_{so}+l_{od})/l_{so}$, and

$$C = \frac{U_0}{i\lambda l_{so}l_{od}(l_{so}+l_{od})}\exp(ik(l_{so}+l_{od}))exp\left(i\frac{\pi y^2}{\lambda l_{od}}\right)\qquad(2.7)$$

In reality, signals received inside a detector pixel are integrated to form the final measured intensity. Without loss of generality, the signal of the pixel bounded by $|y| < P/2$ can be written as

$$I = \int_{-P/2}^{P/2}\mathcal{T}_2(y)|U(y)|^2dy.\qquad(2.8)$$

It is computationally intractable to perform the direct integration, but this challenge can be mitigated by adopting an approximation for the transmittance function and rewriting

Equation (2.3) as

$$T(y) \approx \exp\left(-i\frac{2\pi}{\lambda}(\psi(0) + \psi'(0)y) - \frac{2\pi}{\lambda}B(0)\right),$$ (2.9)

where ψ' is the derivative of ψ with respect to y. The first order asymptotic solution of Equation (2.8) is given by

$$I = \frac{|U_0|^2}{(l_{so} + l_{od})^2}\exp\left(-\frac{4\pi}{\lambda}B(0)\right)\int_{-P/2}^{P/2}\mathcal{T}_2(y)\mathcal{T}_1(l_{od}\psi'(0) + y - M\Delta\xi)dy.$$ (2.10)

Now, a polychromatic source is considered and the source focal spot is assumed to has a non-negative distribution $S(y)$. Moreover, the detector's sensitivity to X-rays with varying energies is represented by a function $\sigma(E)$. The actual measured intensity is again written as

$$I = \frac{|U_0|^2}{(l_{so} + l_{od})^2}\int_{\text{spectrum}}\exp\left(-\frac{4\pi}{\lambda}B(0)\right)$$ (2.11)
$$\int_{-P/2}^{P/2}\mathcal{T}_2(y)\left[\mathcal{T}_1(l_{od}\psi'(0) + y - M\Delta\xi) * S(y\frac{l_{so}}{l_{od}})\right]dy\sigma(E)dE,$$

where $*$ denotes the convolution.

Finally, previous work has shown that a polychromatic system can be approximated by a monochromatic system at effective energy with a good degree of accuracy [36, 38]. Thus, Equation (2.11) can be further simplified to

$$I = \frac{|U_0|^2}{(l_{so} + l_{od})^2}\exp\left(-\frac{4\pi}{\lambda}\bar{B}\right)\int_{-P/2}^{P/2}\bar{\mathcal{T}}_2(y)\left[\bar{\mathcal{T}}_1(l_{od}\bar{\psi}' + y - M\Delta\xi) * S(y\frac{l_{so}}{l_{od}})\right]dy,$$ (2.12)

where the overlines represent that the quantities are evaluated at the effective energy, and the spatial dependences of $\bar{B}$ and $\bar{\psi}'$ have been omitted for simplicity. In the absence of a

sample, the above equation is called the illumination curve:

$$I_{TC}(\Delta\xi) = \frac{|U_0|^2}{(l_{so} + l_{od})^2} \int_{-P/2}^{P/2} \bar{\mathcal{T}}_2(y) \left[\bar{\mathcal{T}}_1(y - M\Delta\xi) * S(y\frac{l_{so}}{l_{od}}) \right] dy. \tag{2.13}$$

Then, the imaging model can be much simplified by using the illumination curve:

$$I = \exp\left(-\frac{4\pi}{\lambda}\bar{B}\right) I_{TC}(\Delta\xi - l_{od}\bar{\psi}'/M) \tag{2.14}$$

To describe the tomographic version of the imaging model, a rotating coordinate system (x_r, y_r) is introduced. The rotating coordinate system is attached to the rotation table and will be utilized to describe the tomographic measurements. The rotating coordinate system is related to the reference system as $x_r = x\cos\theta - y\sin\theta$, $y_r = y\cos\theta + x\sin\theta$. Here, θ denotes the tomographic view angle that is measured from the positive x-axis, y_r denotes the detector coordinate, and the positive x_r-axis denotes the direction of the incident of the X-ray beam, assuming an incident X-ray plane-wave or spherical wave in the paraxial limit. The origin of both coordinate systems is the rotation center in the tomographic scan.

Let $\mathcal{H}$ denote the two-dimensional (2D) Radon transform operator, and $\mathcal{D}$ denote the first-order derivative of the 2D Radon transform with respect to the detector coordinate y_r. The tomographic imaging model can be readily adapted from Equation (2.14) by replacing $\bar{B}$ and $\bar{\psi}'$ by $\mathcal{H}(\beta)$ and $\mathcal{D}(\delta)$. To emphasize the fact that the function obtained after the Radon transform operator is a function of tomographic view angle θ and the detector coordinate y_r, these notations will be modified to $\mathcal{H}(\theta, y_r; \beta)$ and $\mathcal{D}(\theta, y_r; \delta)$.

Now, the tomographic imaging model can be expressed as[36]

$$I(\theta, y_r; \beta, \delta) = \exp\left(-\frac{4\pi}{\lambda}\mathcal{H}(\theta, y_r; \beta)\right) I_{TC}\left(\Delta\xi - \frac{l_{od}}{M}\mathcal{D}(\theta, y_r; \delta)\right), \tag{2.15}$$

where $I(\theta, y_r; \beta, \delta)$ denotes the normalized measured X-ray wave intensity. For simplicity, the arguments of functions $\beta(\boldsymbol{r})$ and $\delta(\boldsymbol{r})$ are dropped. In practice, for a thin object, $\phi(\theta, y_r; \delta)$ is often small enough for Equation (2.15) to be linearized by use of a Taylor expansion [36] as

$$I(\theta, y_r; \beta, \delta) = \exp\left(-\frac{4\pi}{\lambda}\mathcal{H}(\theta, y_r; \beta)\right)\left[I_{TC}(\Delta\xi) - \frac{l_{od}}{M}I'_{TC}(\Delta\xi)\mathcal{D}(\theta, y_r; \delta)\right], \qquad (2.16)$$

where $I'_{TC}(\Delta\xi)$ denotes the first-order derivative of the illumination curve at mask position $\Delta\xi$.

2.3 Reconstruction methods for EIXPCT

2.3.1 Conventional two-step reconstruction methods

The conventional reconstruction method employs a two-step approach [36] – a phase retrieval step followed by a tomographic reconstruction step. In the phase retrieval step, the absorption information is separated from the refractive information. To achieve this, the symmetry of the illumination curve is utilized. Figure 2.2 shows a typical illumination curve I_{TC} as introduced in Equation (2.15). Users of the EIXPCT system have the freedom to select mask displacement $\Delta\xi$ to maximize useful information. Typically, the two half-maximum locations ($\Delta\xi_1$ and $\Delta\xi_2$) are selected because the derivatives of the illumination curve at these two locations are the largest. As a result, the contrast of the refractive index decrement signal is maximized in the measured intensity signals. The illumination levels at these two locations ($I_{TC}(\Delta\xi_1)$ and $I_{TC}(\Delta\xi_2)$) are the same but the derivatives ($I'_{TC}(\Delta\xi_1)$ and $I'_{TC}(\Delta\xi_2)$) are the negative of each other, i.e.:

$$I_{TC}(\Delta\xi_1) = I_{TC}(\Delta\xi_2) \qquad (2.17)$$

$$I'_{TC}(\Delta\xi_1) = -I'_{TC}(\Delta\xi_2) \qquad (2.18)$$
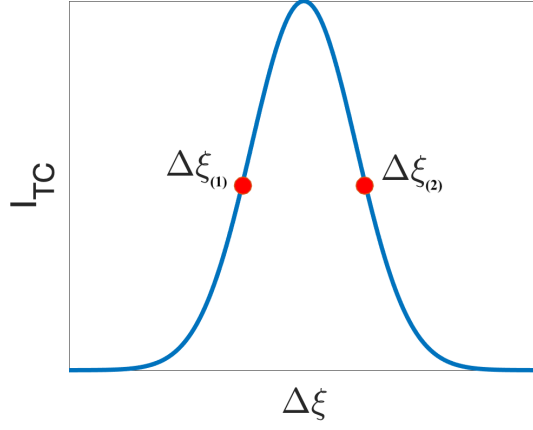
Figure 2.2: A typical illumination curve. The exposures are usually acquired at the two marked locations corresponding to half-maximum illumination level.

When two measurements are obtained at these two mask displacements, the two measured intensities are expressed as:

$$I(\theta, y_r, \Delta\xi_1) = \exp\left(-\frac{4\pi}{\lambda}\int_{\theta,y_r}\beta dl\right) \cdot \left[I_{TC}(\Delta\xi_1) - \frac{l_{od}l_{so}}{l_{so}+l_{od}}I'_{TC}(\Delta\xi_1)\frac{\partial}{\partial x}\int_{\theta,y_r}\delta dl\right], \quad (2.19)$$

$$I(\theta, y_r, \Delta\xi_2) = \exp\left(-\frac{4\pi}{\lambda}\int_{\theta,y_r}\beta dl\right) \cdot \left[I_{TC}(\Delta\xi_1) + \frac{l_{od}l_{so}}{l_{so}+l_{od}}I'_{TC}(\Delta\xi_1)\frac{\partial}{\partial x}\int_{\theta,y_r}\delta dl\right]. \quad (2.20)$$

We can easily transform the above two equations into the following ones where one equation is only related to absorption distribution β and the other one is only related to refractive index decrement distribution δ:

$$\exp\left(-\frac{4\pi}{\lambda}\int_{\theta,y_r}\beta dl\right) = \frac{I(\theta, y_r, \Delta\xi_1) + I(\theta, y_r, \Delta\xi_2)}{I_{TC}(\Delta\xi_1)}, \quad (2.21)$$

and

$$\frac{\partial}{\partial x}\int_{\theta,y_r}\delta dl = \frac{I(\theta, y_r, \Delta\xi_2) - I(\theta, y_r, \Delta\xi_1)}{I(\theta, y_r, \Delta\xi_1) + I(\theta, y_r, \Delta\xi_2)} \cdot \frac{(l_{so}+l_{od})I_{TC}(\Delta\xi_1)}{l_{od}l_{so}I'_{TC}(\Delta\xi_1)}. \quad (2.22)$$

Thus, the projected absorption and refraction information can be analytically separated. In the second tomographic reconstruction step, inverse Radon transformation techniques are applied to solve for the β and δ distributions respectively [27, 44].

The most typical method is the filtered back projection (FBP) algorithm. Consider that phase retrieval is implemented at N tomographic view angles equally distributed within some tomographic angular scanning range with an angular spacing $\Delta\theta$. The FBP algorithm can estimate the absorption distributions as

$$\beta(x,y) = \frac{1}{2\pi} \sum_{i=0}^{N} \Delta\theta_i b(\theta_i, x\cos(\theta_i) + y\sin(\theta_i)) h(x\cos(\theta_i) + y\sin(\theta_i)), \qquad (2.23)$$

where

$$b(\theta, y_r) = \int_{\theta,y_r} \beta dl, \qquad (2.24)$$

and θ_i $(i = 1, 2, ..., N)$ are the tomographic view angle values for the N views. Here, $h(y_r)$ is the Radon kernel whose Fourier transform is $|\omega|$, where ω denotes the frequency [27]. The refractive index decrement distribution, δ, can be estimated in a similar way.

Because the two-step approach requires the explicit phase retrieval, for each tomographic view angle, measurementts must be taken at both mask displacements, making it a multi-shot method that prolongs data-acquisition times and imposes higher doses.

2.3.2   Single-shot data-acquisition methods

Throughout the years, reconstruction methods for single-shot data-acquisition has been proposed, as introduced in Sec. 1.3. Among these technologies, the reverse projection method [19] may be the easiest to implement without restrictive assumptions on the imaged object. This method employs the same experimental set up as described in Sec. 2.1. The method

makes the assumption that the X-ray beams are approximately parallel. Thus, the system can utilize the symmetric property of the tomographic scan. Consider two measured intensity data points that correspond to exactly the same X-ray trajectory, but taken from opposite directions. The two measurements can be modeled as:

$$I(\theta, y_r, \Delta\xi_1) = \exp\left(-\frac{4\pi}{\lambda}\int_{\theta,y_r}\beta dl\right) \cdot \left[I_{TC}(\Delta\xi_1) - \frac{l_{od}l_{so}}{l_{so} + l_{od}}I'_{TC}(\Delta\xi_1)\frac{\partial}{\partial x}\int_{\theta,y_r}\delta dl\right], \quad (2.25)$$

$$I(\theta + \pi, -y_r, \Delta\xi_1) = \exp\left(-\frac{4\pi}{\lambda}\int_{\theta+\pi,-y_r}\beta dl\right) \cdot \left[I_{TC}(\Delta\xi_1) - \frac{l_{od}l_{so}}{l_{so} + l_{od}}I'_{TC}(\Delta\xi_1)\frac{\partial}{\partial x}\int_{\theta+\pi,-y_r}\delta dl\right]$$

$$(2.26)$$

$$= \exp\left(-\frac{4\pi}{\lambda}\int_{\theta,y_r}\beta dl\right) \cdot \left[I_{TC}(\Delta\xi_1) + \frac{l_{od}l_{so}}{l_{so} + l_{od}}I'_{TC}(\Delta\xi_1)\frac{\partial}{\partial x}\int_{\theta,y_r}\delta dl\right].$$

The right sides of the above two equations are exactly the same as those of Equation (2.19) and Equation (2.20), and thus the following processing steps are the same. The advantage of the reverse projection method is that it is extremely easy to implement and reconstruct. There is no need to move the masks throughout the imaging process. However, it still suffers from the fact that restrictive assumption about the geometry is employed. Although this assumption is generally acceptable for most of currently available EIXPCT systems, the model mismatch between the actual system and the reconstruction algorithm may still lead to potential errors.

Chapter 3

A Joint Reconstruction Method for Edge-Illumination Phase-Contrast Tomography

3.1 Introduction

In this component of research, a new single-shot method for EIXPCT that circumvents limitations of conventional methods will be introduced. It allows fast single-shot imaging without restrictive assumptions so flexible data-acquisition designs are possible. In the proposed method, the phase-retrieval and image reconstruction steps are combined into a single step. Estimates of δ and β are computed directly from the single-shot tomographic measurement data by use of a non-linear joint reconstruction (JR) method. We will evaluate the JR method's feasibility with both simulated and experimental datasets.

3.2 Forward imaging model

3.2.1 Forward imaging model in its continuous form

For the canonical EIXPCT system introduced in Sec. 2.1 and depicted in Figure 2.1 [18, 36]. Sec. 2.2 has thoroughly introduced the imaging process of EIXPCT system and the imaging model can be derived as Equation (2.16).

3.2.2 Forward imaging model in its discrete form

In order to formulate image reconstruction in single-shot EIXPCT as a numerical optimization problem, the imaging model in Equation (2.16) is discretized. Let the vectors $\boldsymbol{\beta} = [\beta_{1,1}, \beta_{1,2}, ..., \beta_{1,N_x}, \beta_{2,1}, ..., \beta_{N_x,N_y}]^T \in \mathbb{R}^N$ and $\boldsymbol{\delta} = [\delta_{1,1}, \delta_{1,2}, ..., \delta_{1,N_x}, \beta_{2,1}, ..., \delta_{N_x,N_y}]^T \in \mathbb{R}^N$ represent the values of $\beta(\mathbf{r})$ and $\delta(\mathbf{r})$ sampled at the $N = N_x N_y$ vertices $\boldsymbol{r}_{i,j} = (x_i, y_j)$ ($i = 1, 2, ..., N_x$ and $j = 1, 2, ..., N_y$) of a Cartesian grid. Consider that Q samples of the wavefield intensity corresponding to sampled values of y_r are acquired at each of P tomographic view angles. The vector $\boldsymbol{I}(\boldsymbol{\beta}, \boldsymbol{\delta}) \in \mathbb{R}^{PQ}$ contains a lexicographical ordering of these values. The notation $[\cdot]_i$ will be employed to denote the i-th component of the vector enclosed by the brackets.

Discrete representations of the 2D Radon transform and its first-order derivative will be denoted as $\boldsymbol{H} \in \mathbb{R}^{PQ \times N}$ and $\boldsymbol{D} \in \mathbb{R}^{PQ \times N}$, respectively. Finally, let $\boldsymbol{\Delta \xi} \in \mathbb{R}^P$ denote the collection of aperture offsets employed at the different tomographic view angles. Is should be noted that in previously proposed single-shot methods, the aperture offset was assumed to be fixed for all view angles. However, as described below, the proposed image reconstruction method will permit exploration of more general single-shot data-acquisition protocols in

which the aperture offset varies with view angle. The quantity $[\boldsymbol{\Delta\xi}]_{\lceil \frac{i}{Q} \rceil}$ corresponds to the aperture offset employed at the tomographic view angle corresponding to the measurement $[\boldsymbol{I}(\boldsymbol{\beta},\boldsymbol{\delta})]_i$, where $\lceil \frac{i}{Q} \rceil$ defines the smallest integer larger than $\frac{i}{Q}$. In terms of these quantities, a discrete version of the imaging model can be expressed as

$$[\boldsymbol{I}(\boldsymbol{\beta},\boldsymbol{\delta})]_i = \exp\left(-\frac{4\pi}{\lambda}[\boldsymbol{H}\boldsymbol{\beta}]_i\right)\left[I_{TC}([\boldsymbol{\Delta\xi}]_{\lceil \frac{i}{Q} \rceil}) - \frac{l_{od}}{M}I'_{TC}([\boldsymbol{\Delta\xi}]_{\lceil \frac{i}{Q} \rceil})[\boldsymbol{D}\boldsymbol{\delta}]_i\right], \qquad (3.1)$$

where $i = 1, 2, ..., PQ$.

3.3   Joint Reconstruction Method

3.3.1   Joint reconstruction method in its continuous form

In this section, we first derive the JR method in its continuous form based on the continuous forward imaging model Equation (2.16). Equation (2.16) shows that the measured intensity is a function of tomographic view angle θ, detector location y_r, absorption distribution β and refractive index decrement distribution δ. The four parameters of this equation can be classified into two groups: the imaging-process-related group (θ and y_r) and the object-related group (β and δ). The imaging-process-related parameters relate to the imaging configuration, and the object-related parameters relate to the object.

In practice, the object-related parameters β and δ are fixed for a given object, so the measured intensity I can be written as $I(\theta, y_r)$ – simply a function of θ and y_r. From this perspective, the imaging process can be models as an operator $\mathcal{I} : \mathbb{L}^2(\mathbb{R}^2) \otimes \mathbb{L}^2(\mathbb{R}^2) \to \mathbb{L}^2([0, 2\pi) \times \mathbb{R})$ that maps the object properties $\beta(\boldsymbol{r})$ and $\delta(\boldsymbol{r})$ to the measured intensity function $I(\theta, y_r)$. For simplicity, the arguments of functions are dropped, so the mapping relationship can be denoted by $I = \mathcal{I}(\beta, \delta)$. Using the two operators introduced earlier ($\mathcal{H} : \mathbb{L}^2(\mathbb{R}^2) \to \mathbb{L}^2([0, 2\pi) \times \mathbb{R})$

and $\mathcal{D} : \mathbb{L}^2(\mathbb{R}^2) \to \mathbb{L}^2([0, 2\pi) \times \mathbb{R}))$ to denote the 2D Radon transformation and the derivative of Radon transformation along the y coordinate, the imaging process can be written as

$$\mathcal{I}(\beta, \delta) = \exp\left(-\frac{4\pi}{\lambda}\mathcal{H}(\beta)\right)\left[I_{TC}(\Delta\xi) - \frac{l_{od}}{M}I'_{TC}(\Delta\xi)\mathcal{D}(\delta)\right]. \tag{3.2}$$

The inverse problem is to solve for the absorption distribution β and refractive index distribution δ given measurement data. In this section, the problem is described in a continuous setting. Let I_m denoted the measured intensity where the tomographic view angle ranges from 0 to 2π and the detector position $y \in (-\infty, \infty)$ (the arguments (θ, y_r) is dropped here for simplicity and notation consistency). In contrast to the FBP method that is typically employed in the conventional two-step method, in the JR method, the absorption and refractive index distributions are estimated by solving an optimization problem. The cost function to be minimized is considered to be of the form

$$f(\beta, \delta) = \|I_m - \mathcal{I}(\beta, \delta)\|^2 + R(\beta, \delta). \tag{3.3}$$

Here, $R(\beta, \delta)$ is a regularization term that can be designed freely.

A gradient descent algorithm can be employed to solve the optimization problem. The gradients of the cost function with respect to the absorption and refractive index distributions are [9]:

$$\frac{\partial f}{\partial \beta} = 2\mathcal{I}'^*_\beta[I_m - \mathcal{I}(\beta, \delta)] + R'_\beta(\beta, \delta), \tag{3.4}$$

$$\frac{\partial f}{\partial \delta} = 2\mathcal{I}'^*_\delta[I_m - \mathcal{I}(\beta, \delta)] + R'_\delta(\beta, \delta), \tag{3.5}$$

where $\mathcal{I}'_\beta$ and $\mathcal{I}'_\delta$ denote the gradient of $\mathcal{I}(\beta, \delta)$ with respect to β and δ. The quantities $\mathcal{I}'^*_\beta$ and $\mathcal{I}'^*_\delta$ denote the adjoint operators corresponding to $\mathcal{I}'_\beta$ and $\mathcal{I}'_\delta$, respectively. Similarly, R'_β

and R'_δ denote the gradient of $R(\beta, \delta)$ with respect to β and δ, respectively. The operators $\mathcal{I}'^*_\beta$ and $\mathcal{I}'^*_\delta$ can be analytically calculated as

$$\mathcal{I}'^*_\beta = -\frac{4\pi}{\lambda}\mathcal{H}^* \left[I_{TC}(\Delta\xi) - \frac{l_{od}}{M} I'_{TC}(\Delta\xi)\mathcal{D}(\delta) \right] \exp\left(-\frac{4\pi}{\lambda}\mathcal{H}(\beta) \right), \qquad (3.6)$$

$$\mathcal{I}'^*_\delta = -\mathcal{D}^* \left[\frac{l_{od}}{M} I'_{TC}(\Delta\xi) \right] \exp\left(-\frac{4\pi}{\lambda}\mathcal{H}(\beta) \right), \qquad (3.7)$$

where $\mathcal{H}^*$ and $\mathcal{D}^*$ are the adjoints of $\mathcal{H}$ and $\mathcal{D}$. The derivation process is given in Appendix A.

3.3.2 Joint reconstruction method in its discrete form

The description of the JR method in the continuous form has demonstrated the essence of this method, but to really solve a reconstruction problem utilizing digital computers in practice, a discretized reconstruction method is necessary. Based on the discrete imaging model, JR of $\boldsymbol{\beta}$ and $\boldsymbol{\delta}$ can be formulated as a numerical optimization problem. Let $\boldsymbol{I}_m$ and $\boldsymbol{I}(\boldsymbol{\beta}, \boldsymbol{\delta})$ denote the measured intensity data and the intensity data simulated by use of Equation (3.1) for a specified choice of $\boldsymbol{\delta}$ and $\boldsymbol{\beta}$, respectively. Penalized least squares estimates of $\boldsymbol{\delta}$ and $\boldsymbol{\beta}$ can be jointly determined as

$$(\tilde{\boldsymbol{\beta}}, \tilde{\boldsymbol{\delta}}) = \arg\min_{\boldsymbol{\beta},\boldsymbol{\delta}} f(\boldsymbol{\beta}, \boldsymbol{\delta}) = \arg\min_{\boldsymbol{\beta},\boldsymbol{\delta}} ||\boldsymbol{I}_m - \boldsymbol{I}(\boldsymbol{\beta}, \boldsymbol{\delta})||^2 + R(\boldsymbol{\beta}, \boldsymbol{\delta}), \qquad (3.8)$$

where $R(\boldsymbol{\beta}, \boldsymbol{\delta})$ is a penalty function that imposes regularization on the estimates. The first term in the objective function in Equation (3.8) - the data fidelity term - is non-convex. However, as demonstrated below, this will not prevent accurate image reconstruction. In this work, the penalty function was taken to be of the form $R(\boldsymbol{\beta}, \boldsymbol{\delta}) = l_1 R_\beta(\boldsymbol{\beta}) + l_2 R_\delta(\boldsymbol{\delta})$, where l_1 and l_2 denote regularization parameters, and $R_\beta(\boldsymbol{\beta})$ and $R_\delta(\boldsymbol{\delta})$ are differentiable functions.

The gradients of the objective function $f(\boldsymbol{\beta}, \boldsymbol{\delta})$ with respect to the vectors $\boldsymbol{\beta}$ and $\boldsymbol{\delta}$ are given by

$$\nabla_{\boldsymbol{\beta}} f(\boldsymbol{\beta}, \boldsymbol{\delta}) = 2\boldsymbol{I}'^{*}_{\boldsymbol{\beta}}(\boldsymbol{I}(\boldsymbol{\beta}, \boldsymbol{\delta}) - \boldsymbol{I}_m) + l_1 \nabla_{\boldsymbol{\beta}} R_{\beta}(\boldsymbol{\beta}), \tag{3.9}$$

$$\nabla_{\boldsymbol{\delta}} f(\boldsymbol{\beta}, \boldsymbol{\delta}) = 2\boldsymbol{I}'^{*}_{\boldsymbol{\delta}}(\boldsymbol{I}(\boldsymbol{\beta}, \boldsymbol{\delta}) - \boldsymbol{I}_m) + l_2 \nabla_{\boldsymbol{\delta}} R_{\delta}(\boldsymbol{\delta}), \tag{3.10}$$

where $\boldsymbol{I}'^{*}_{\boldsymbol{\beta}} \in \mathbb{R}^{N \times PQ}$ and $\boldsymbol{I}'^{*}_{\boldsymbol{\delta}} \in \mathbb{R}^{N \times PQ}$ denote the adjoint operators corresponding to the derivatives of $\boldsymbol{I}(\boldsymbol{\beta}, \boldsymbol{\delta})$ with respect to $\boldsymbol{\beta}$ and $\boldsymbol{\delta}$, respectively. The adjoint operators, applied to a small vector $\boldsymbol{\epsilon} \in \mathbb{R}^{PQ}$, can be computed as

$$\boldsymbol{I}'^{*}_{\tilde{\boldsymbol{\beta}}} \boldsymbol{\epsilon} = -\frac{4\pi}{\lambda} \boldsymbol{H}^{*} \boldsymbol{x} \text{ and } \boldsymbol{I}'^{*}_{\tilde{\boldsymbol{\delta}}} \boldsymbol{\epsilon} = -\boldsymbol{D}^{*} \boldsymbol{y}, \tag{3.11}$$

where

$$[\boldsymbol{x}]_i = \left(I_{TC}([\boldsymbol{\Delta}\boldsymbol{\xi}]_{\lceil \frac{i}{Q} \rceil}) - \frac{l_{od}}{M} I'_{TC}([\boldsymbol{\Delta}\xi]_{\lceil \frac{i}{Q} \rceil})[\boldsymbol{D}\boldsymbol{\delta}]_i \right) \exp\left(-\frac{4\pi}{\lambda}[\boldsymbol{H}\boldsymbol{\beta}]_i \right) \boldsymbol{\epsilon}_i, \tag{3.12}$$

$$[\boldsymbol{y}]_i = \frac{l_{od}}{M} I'_{TC}([\boldsymbol{\Delta}\xi]_{\lceil \frac{i}{Q} \rceil}) \exp\left(-\frac{4\pi}{\lambda}[\boldsymbol{H}\boldsymbol{\beta}]_i \right) \boldsymbol{\epsilon}_i, \ i = 1, 2, ..., PQ. \tag{3.13}$$

A batch gradient algorithm is proposed for solving Equation (3.8). Pseudocode for the algorithm is provided in Algorithm 1. The iteration stops when the objective function value falls below a specified threshold.

The selection of $R_{\beta}(\boldsymbol{\beta})$ and $R_{\delta}(\boldsymbol{\delta})$ will in general be motivated by several factors. A popular choice is the total variation (TV) semi-norm [48] which encourage the objects to be piece-wise constant and is popular in medical imaging applications [4, 5, 6, 46]. The TV regularizations

Algorithm 1 JR of $\tilde{\boldsymbol{\beta}}$ and $\tilde{\boldsymbol{\delta}}$ using a batch gradient algorithm

---

1: Calibrate the illumination curve
2: Read in measured data $\boldsymbol{I}_m$
3: Initialization: $\tilde{\boldsymbol{\beta}}^{(0)} \leftarrow 0; \tilde{\boldsymbol{\delta}}^{(0)} \leftarrow 0; k \leftarrow 0$
4: **while** stopping criterion is not satisfied **do**
5:     $k \leftarrow k + 1$
6:     Calculate the intensity data $\boldsymbol{I}(\tilde{\boldsymbol{\beta}}^{(k)}, \tilde{\boldsymbol{\delta}}^{(k)})$
7:     Compute cost $||\boldsymbol{I}_m - \boldsymbol{I}(\tilde{\boldsymbol{\beta}}^{(k)}, \tilde{\boldsymbol{\delta}}^{(k)})||^2 + R(\tilde{\boldsymbol{\beta}}^{(k)}, \tilde{\boldsymbol{\delta}}^{(k)})$
8:     $\boldsymbol{d}_{\boldsymbol{\beta}} \leftarrow -\nabla_{\boldsymbol{\beta}}||\boldsymbol{I}_m - \boldsymbol{I}(\tilde{\boldsymbol{\beta}}^{(k)}, \tilde{\boldsymbol{\delta}}^{(k)})||^2 + l_1 \nabla_{\boldsymbol{\beta}} R_{\beta}(\tilde{\boldsymbol{\beta}}^{(k)})$ {$\nabla_{\boldsymbol{\beta}}$ denotes the derivative w.r.t. $\tilde{\boldsymbol{\beta}}$}
9:     $\boldsymbol{d}_{\boldsymbol{\delta}} \leftarrow -\nabla_{\boldsymbol{\delta}}||\boldsymbol{I}_m - \boldsymbol{I}(\tilde{\boldsymbol{\beta}}^{(k)}, \tilde{\boldsymbol{\delta}}^{(k)})||^2 + l_2 \nabla_{\boldsymbol{\delta}} R_{\delta}(\tilde{\boldsymbol{\delta}}^{(k)})$ {$\nabla_{\boldsymbol{\delta}}$ denotes the derivative w.r.t. $\tilde{\boldsymbol{\delta}}$}
10:     $(\tilde{\boldsymbol{\beta}}^{(k+1)}, \tilde{\boldsymbol{\delta}}^{(k+1)}) \leftarrow (\tilde{\boldsymbol{\beta}}^{(k)}, \tilde{\boldsymbol{\delta}}^{(k)}) + \tau(\boldsymbol{d}_{\boldsymbol{\beta}}, \boldsymbol{d}_{\boldsymbol{\delta}})$ { τ is the step size obtained by a line search method}
11: **end while**

---

of $\boldsymbol{\beta}$ and $\boldsymbol{\delta}$ are defined to be

$$R_{\beta}(\boldsymbol{\beta}) = \sum_{i,j} \sqrt{(\boldsymbol{\beta}_{i,j} - \boldsymbol{\beta}_{i-1,j})^2 + (\boldsymbol{\beta}_{i,j} - \boldsymbol{\beta}_{i,j-1})^2}, \qquad (3.14)$$

and

$$R_{\delta}(\boldsymbol{\delta}) = \sum_{i,j} \sqrt{(\boldsymbol{\delta}_{i,j} - \boldsymbol{\delta}_{i-1,j})^2 + (\boldsymbol{\delta}_{i,j} - \boldsymbol{\delta}_{i,j-1})^2}. \qquad (3.15)$$

The problem with TV norm to be used in the batch gradient algorithm is that the TV norm is not differentiable. As a result, a smoothed version of TV norm is employed instead [53]. In this case, the smoothed TV norms are defined to be

$$R_{\beta}(\boldsymbol{\beta}) = \sum_{i,j} \sqrt{(\boldsymbol{\beta}_{i,j} - \boldsymbol{\beta}_{i-1,j})^2 + (\boldsymbol{\beta}_{i,j} - \boldsymbol{\beta}_{i,j-1})^2 + \epsilon}, \qquad (3.16)$$

and

$$R_{\delta}(\boldsymbol{\delta}) = \sum_{i,j} \sqrt{(\boldsymbol{\delta}_{i,j} - \boldsymbol{\delta}_{i-1,j})^2 + (\boldsymbol{\delta}_{i,j} - \boldsymbol{\delta}_{i,j-1})^2 + \epsilon}. \qquad (3.17)$$

where ϵ is a small positive value. Thus, their derivatives are derived as

$$\nabla_{\boldsymbol{\beta}} R_{\beta}(\boldsymbol{\beta}) = \frac{2(\boldsymbol{\beta}_{i,j} - \boldsymbol{\beta}_{i-1,j}) + 2(\boldsymbol{\beta}_{i,j} - \boldsymbol{\beta}_{i,j-1})}{\sqrt{\epsilon + (\boldsymbol{\beta}_{i,j} - \boldsymbol{\beta}_{i-1,j})^2 + (\boldsymbol{\beta}_{i,j} - \boldsymbol{\beta}_{i,j-1})^2}} - \frac{2(\boldsymbol{\beta}_{i+1,j} - \boldsymbol{\beta}_{i,j})}{\sqrt{\epsilon + (\boldsymbol{\beta}_{i+1,j} - \boldsymbol{\beta}_{i,j})^2 + (\boldsymbol{\beta}_{i+1,j} - \boldsymbol{\beta}_{i+1,j-1})^2}}$$
$$- \frac{2(\boldsymbol{\beta}_{i,j+1} - \boldsymbol{\beta}_{i,j})}{\sqrt{\epsilon + (\boldsymbol{\beta}_{i,j+1} - \boldsymbol{\beta}_{i,j})^2 + (\boldsymbol{\beta}_{i,j+1} - \boldsymbol{\beta}_{i-1,j+1})^2}},$$

$$(3.18)$$

and

$$\nabla_{\boldsymbol{\delta}} R_{\delta}(\boldsymbol{\delta}) = \frac{2(\boldsymbol{\delta}_{i,j} - \boldsymbol{\delta}_{i-1,j}) + 2(\boldsymbol{\delta}_{i,j} - \boldsymbol{\delta}_{i,j-1})}{\sqrt{\epsilon + (\boldsymbol{\delta}_{i,j} - \boldsymbol{\delta}_{i-1,j})^2 + (\boldsymbol{\delta}_{i,j} - \boldsymbol{\delta}_{i,j-1})^2}} - \frac{2(\boldsymbol{\delta}_{i+1,j} - \boldsymbol{\delta}_{i,j})}{\sqrt{\epsilon + (\boldsymbol{\delta}_{i+1,j} - \boldsymbol{\delta}_{i,j})^2 + (\boldsymbol{\delta}_{i+1,j} - \boldsymbol{\delta}_{i+1,j-1})^2}}$$
$$- \frac{2(\boldsymbol{\delta}_{i,j+1} - \boldsymbol{\delta}_{i,j})}{\sqrt{\epsilon + (\boldsymbol{\delta}_{i,j+1} - \boldsymbol{\delta}_{i,j})^2 + (\boldsymbol{\delta}_{i,j+1} - \boldsymbol{\delta}_{i-1,j+1})^2}}.$$

$$(3.19)$$

Then, the batch gradient algorithm can be applied to solve the optimization problem defined in Equation (3.8).

The optimization problem can also be solved directly by a fast iterative shrinkage-thresholding algorithm (FISTA)[1] without employing the approximation for the TV penalty. The reconstructed images from the batch gradient algorithm and FISTA were found to be similar based on our experience.

3.4   Simulation Study

Computer-simulation studies were first conducted to demonstrate the feasibility of achieving accurate JR of $\boldsymbol{\beta}$ and $\boldsymbol{\delta}$ from idealized noiseless measurements by use of Algorithm 1. The numerical phantoms shown in Figs. 3.1a and 3.1b were employed to represent $\boldsymbol{\beta}$ and $\boldsymbol{\delta}$. The

phantoms contained 256×256 pixels of size $100 \, \mu m \times 100 \, \mu m$ and the values of $\boldsymbol{\beta}$ and $\boldsymbol{\delta}$ were representative of soft tissue. Both phantoms contained multiple materials.
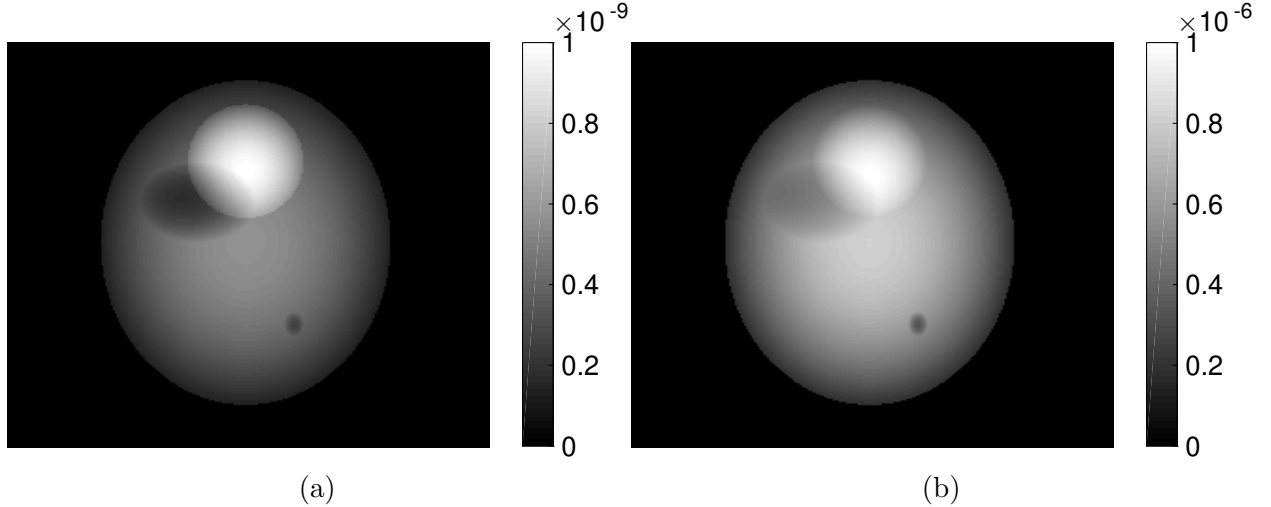
Figure 3.1: Numerical phantoms utilized to represent (a) $\boldsymbol{\beta}$ and (b) $\boldsymbol{\delta}$ in the computer-simulation studies.

Noiseless simulated intensity data were computed by use of Equation (2.15). At each view angle, 400 samples of the wavefield intensity were specified along the detector array. The illumination curve was modeled after experimental measurements [19]. It was specified as a Gaussian distribution $I_{TC} = 0.13 + 0.87 \exp(-\Delta \xi^2 / 1.84 \times 10^{-10})$, where $\Delta \xi$ has units of m and I_{TC} has arbitrary units. The offset $\Delta \xi$ was specified as $\Delta \xi = 9.6 \, \mu m$, as $\Delta \xi \pm 9.6 \, \mu m$ corresponded to the locations of largest derivative of the illumination curve. The assumed imaging parameters were: $l_{so} = 1.6$ m, $l_{od} = 0.4$ m, $\lambda = 10^{-10}$ m.

Two distinct single-shot EIXPCT data sets were computed using the methodology described above. The first data set was a conventional single-shot data in which the aperture offset was constant at 720 evenly spaced view angles that spanned a 2π angular range; this data set will be referred to as the constant aperture position (CAP) plan. The offset value was $\Delta \xi = 9.6 \, \mu m$. The second single-shot data set was non-conventional and its design was
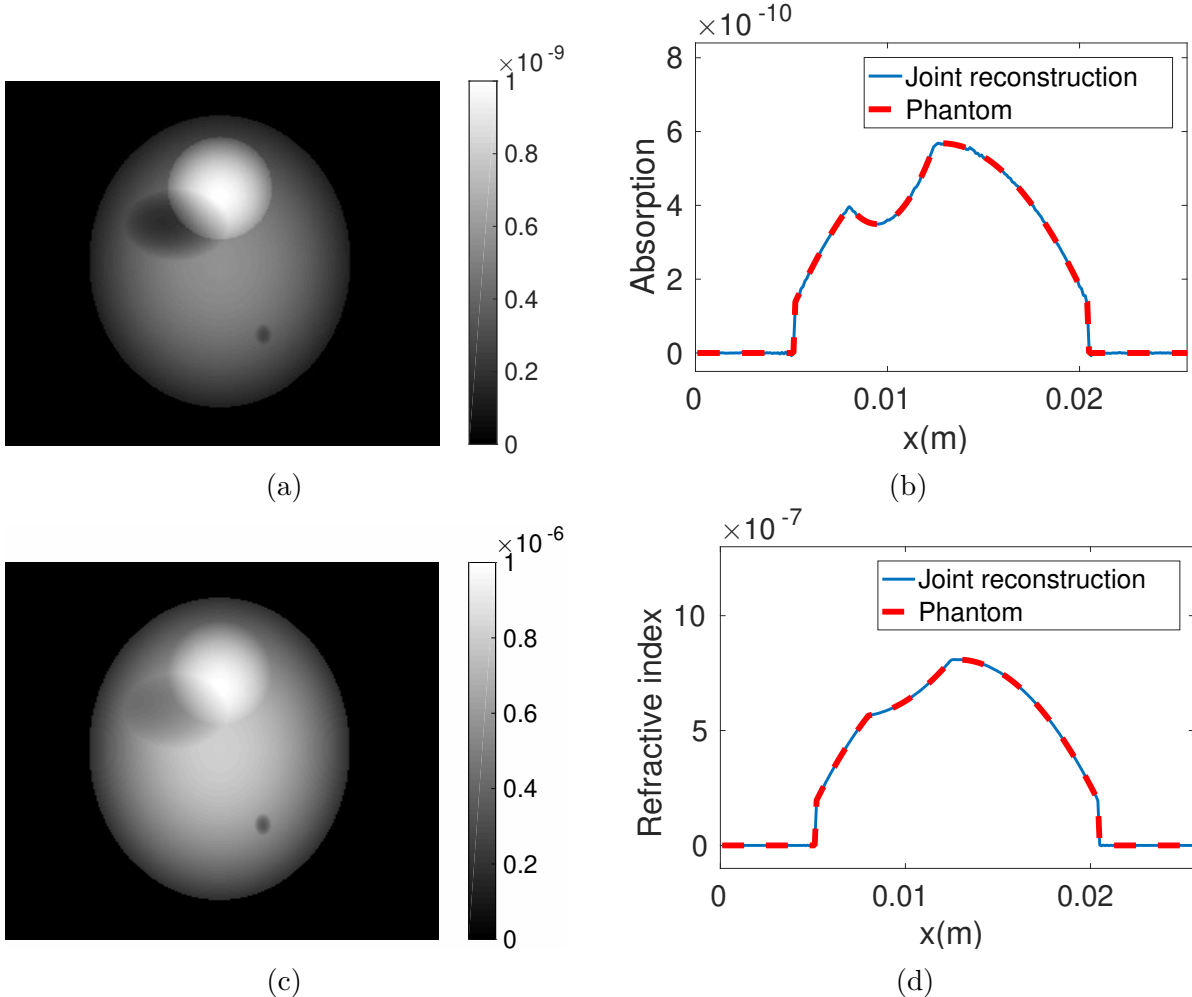
Figure 3.2: Computer-simulation results corresponding to the CAP plan. Reconstructed estimates of $\boldsymbol{\beta}$ (MSE = 1.8×10^{-24}) and $\boldsymbol{\delta}$ (MSE = 1.3×10^{-19}) are shown in subfigures (a) and (c). Line profiles through the reconstructed images and corresponding true phantoms are shown in subfigures (b) and (d).

motivated by the flexibility of the proposed JR method. In this data set, referred to as the alternating aperture position (AAP) plan, intensity data were collected at 360 evenly spaced view angles that spanned a π angular range. However, instead of keeping the aperture offset fixed, it was alternated between $\Delta\xi = 9.6 \ \mu m$ and $\Delta\xi = -9.6 \ \mu m$, changing value at every view angle. The AAP plan addresses the situation when single-shot measurements are not available over a complete 2π range. Images were reconstructed from both data sets by use of Algorithm 1 with $l_1 = l_2 = 0$ (i.e., no regularization).
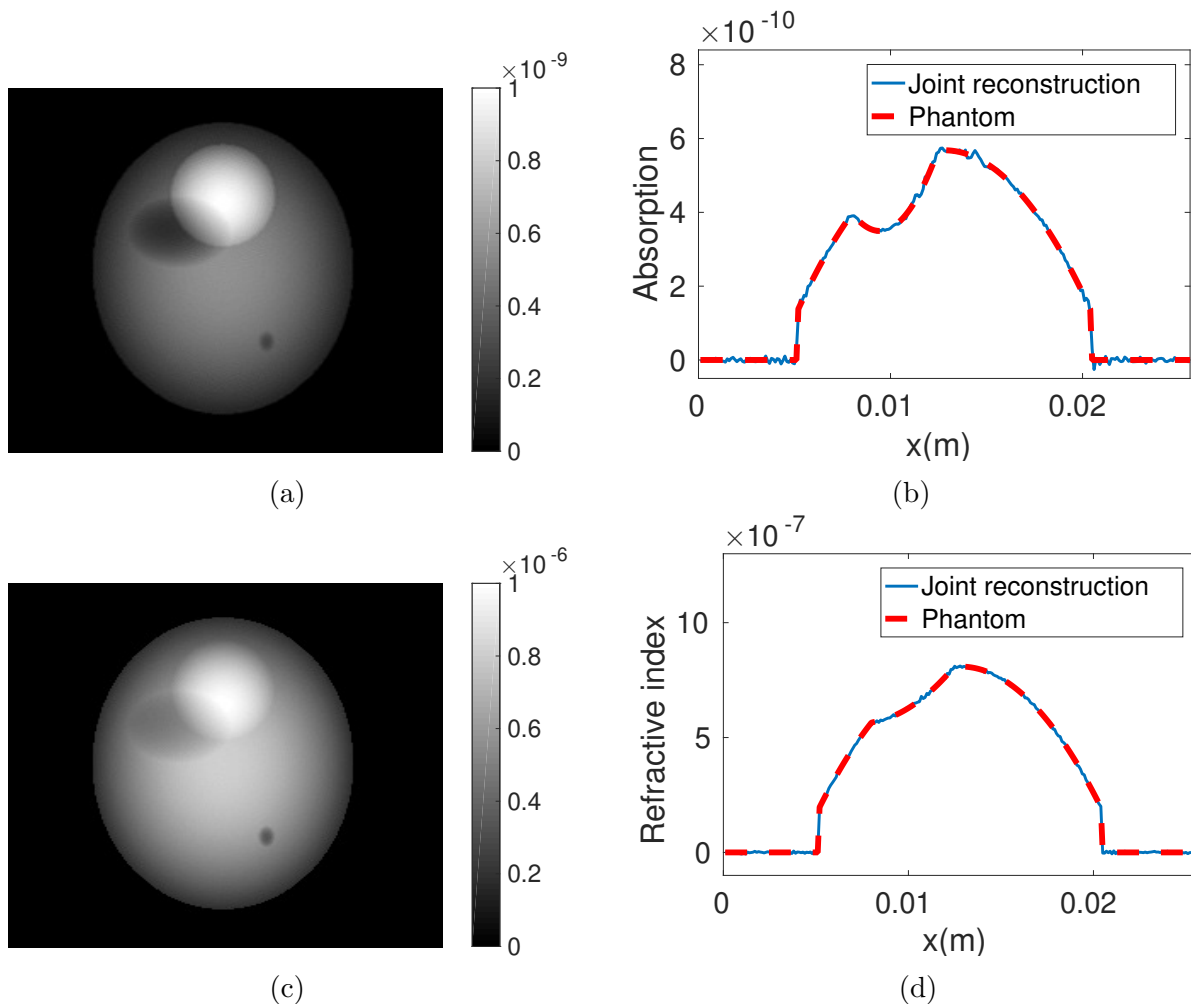
Figure 3.3: Computer-simulation results corresponding to the AAP plan. Reconstructed estimates of $\boldsymbol{\beta}$ (MSE = 3.5×10^{-23}) and $\boldsymbol{\delta}$ (MSE = 7.5×10^{-18}) are shown in subfigures (a) and (c). Line profiles through the reconstructed images and corresponding true phantoms are shown in subfigures (b) and (d).

The reconstructed images and image profiles corresponding to the CAP plan are shown in Figs. 3.2. These results confirm that the JR algorithm can reconstruct highly accurate images from idealized single-shot data. A similar observation holds true for the AAP plan results shown Figure 3.3. The AAP plan results suggest, for the first time, that a full 2π angular scanning range can be traded for a reduced scanning range of (at least) π if additional diversity in the measured data are created by varying the aperture offset as a function of view angle.

27

3.5 Experimental Validation
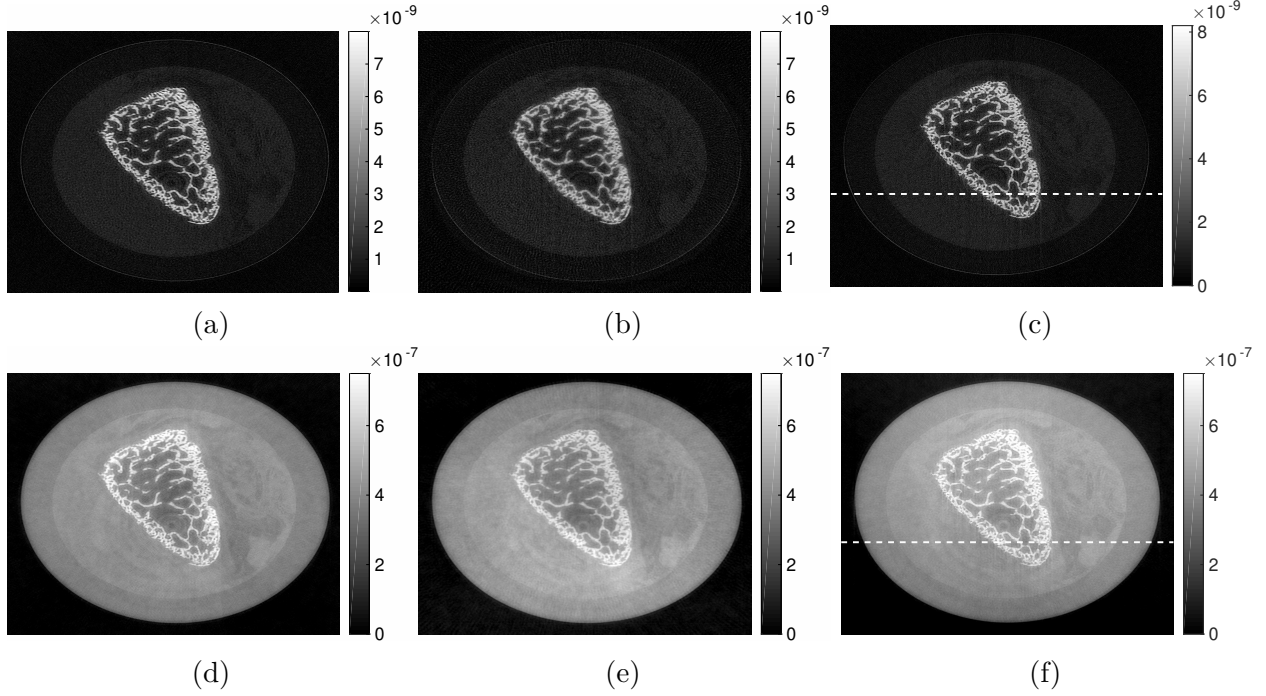
Figure 3.4: Estimates of $\boldsymbol{\beta}$ (top row) and $\boldsymbol{\delta}$ (bottom row) that were jointly reconstructed from the (a),(d) CAP data set, and (b),(e) AAP data set. The corresponding estimates obtained by use of the conventional two-step method are shown in subfigures (c) and(d).

To demonstrate the value of the JR method under realistic conditions, studies that utilized experimental EIXPCT data sets were conducted. The experimental data were acquired in a previous study [19]. The imaged sample corresponded to a chicken bone and the mean X-ray energy was 17 keV. Addition details regarding the imaging system and imaging parameters can be found in reference [19]. As in the computer-simulation studies, intensity data were acquired at 720 view angles that were uniformly distributed over a 2π angular range. At each view angle, two intensity measurements were acquired corresponding to approximately symmetric positions on the illumination curve. A CAP data set was formed by retaining the measurements corresponding to one side of the illumination curve. An AAP data set was
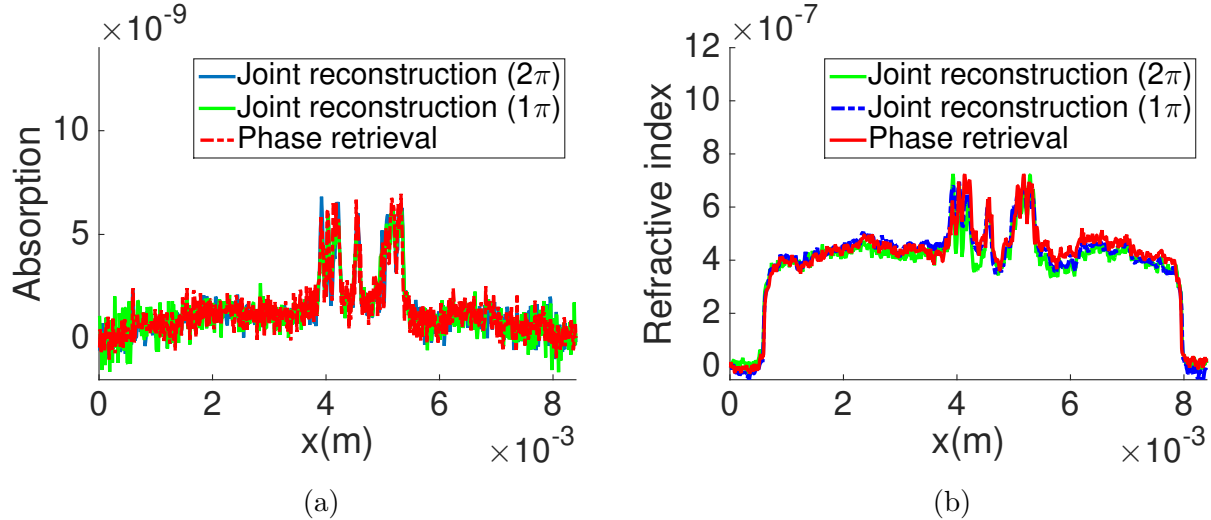
Figure 3.5: Profiles through the reconstructed images for all data-acquisition plans at the white dashed line indicated in Figs. 3.4c and 3.4f. The profiles corresponding to the estimates of $\boldsymbol{\beta}$ and $\boldsymbol{\delta}$ are shown in subfigures (a) and (b), respectively.

formed by keeping either the measurement corresponding to the positive or negative side of the illumination curve, in an alternating fashion as a function of view angle. Images were reconstructed from the CAP and AAP data sets by use of Algorithm 1. The penalty functions $R_\beta(\boldsymbol{\beta})$ and $R_\delta(\boldsymbol{\delta})$ were specified as a smoothed version of the total variation semi-norm [53]. Suitable values of the regularization parameters l_2 and l_1 were manually determined and fixed for use with both data sets. Images were also reconstructed by use of a conventional (non-single-shot) approach in which both images acquired at each view angle were employed to perform phase-retrieval, followed by application of the FBP algorithm to determine estimates of $\boldsymbol{\beta}$ and $\boldsymbol{\delta}$ [19]. In this case, a π angular scanning range was utilized. In all cases, the pixel size of the reconstructed images was 9.9 μm.

The reconstructed images and corresponding image profiles reconstructed from the experimental data sets are displayed in Figs. 3.4 and 3.5. In all of the reconstructed images, the features of the bone structure can be clearly identified. Moreover, as evident from the nearly overlapping image profiles, the images reconstructed from the CAP and AAP single-shot

data sets by use of the JR method are close in quantitative value to those reconstructed by use of the conventional two step approach.

3.6 Conclusion

In summary, a new JR method was proposed for single-shot EIXPCT. The proposed JR method, in effect, combines the phase-retrieval and image reconstruction steps into one. The JR method was formulated as a numerical optimization problem and a gradient-based algorithm was developed for its solution. The proposed method possesses advantages over previously-proposed single-shot methods for EIXPCT. The method does not require the assumption of a single material object [12]. Moreover, it does not require a parallel-beam geometry [19] and can be applied to the case of a cone-beam geometry where the incident beam divergence must be considered. Additionally, the method does not require use of an energy-sensitive detector [10] and can be employed with readily available integrating X-ray detectors. Finally, the flexibility of the method permits exploration of innovative data-acquisition protocols for single-shot EIXPCT, such as the AAP plan, which can relax requirements on the range of angular scanning. Additional studies are required to comprehensively evaluate the numerical and statistical properties of the method.

Chapter 4

Numerical Properties of the Joint Reconstruction Method

4.1 Introduction

The JR method simplifies and speeds up the data-acquisition process and helps reduce doses [9]. This method involves formulation of an optimization problem that is solved by use of a batch gradient descent algorithm. The method imposes no restrictive assumptions on imaging geometry or material composition and requires no special masks or detectors. The effectiveness of the JR method has been validated with both computer-simulated and experimental datasets [9]. However, the numerical properties of the JR method have not been explored systematically. Therefore, the applicability and robustness of this method to a general case situation remain unclear.

The goal of this study is to investigate the numerical properties of the JR method through computer-simulation studies. Three vital aspects are considered. First, the convexity of the

cost function defined in the optimization problem employed in the JR method is analyzed in Section 4.3. Convex optimization problems don't have local minima, so they are guaranteed to converge to a global minimum with the gradient-descent algorithm. On the contrary, a non-convex problem may become trapped in local minima. Studying the convexity property helps understand the robustness of the algorithm.

Second, the cross-talk effect between the two channels (absorption and refractive index) in JR is investigated. In general, for multi-channel reconstruction methods, because the information needed for reconstructing various channels is mixed together in the recorded measurements, mitigating cross-talk between different channels can be a challenge. In the iterative framework employed in the JR method, the estimated value of β (or δ) at one iteration can influence the estimate of δ (or β) at the next iteration. If the cross-talk effect is strong, and one channel takes suboptimal values in the previous iteration, the reconstruction of the other channel may be led in a wrong direction and the values may end up in local minima. In summary, whether the cross-talk effect is negligible or not depends on the ability of the algorithm to accurately reconstruct one channel without reliance on an accurate estimate of the other channel. This is investigated in Section 4.4.

Finally, an analysis of the noise statistics of the reconstructed images is also conducted. This reveals the upper bound for quality of reconstructed images in term of biases and variances. This study is presented in Section 4.5.
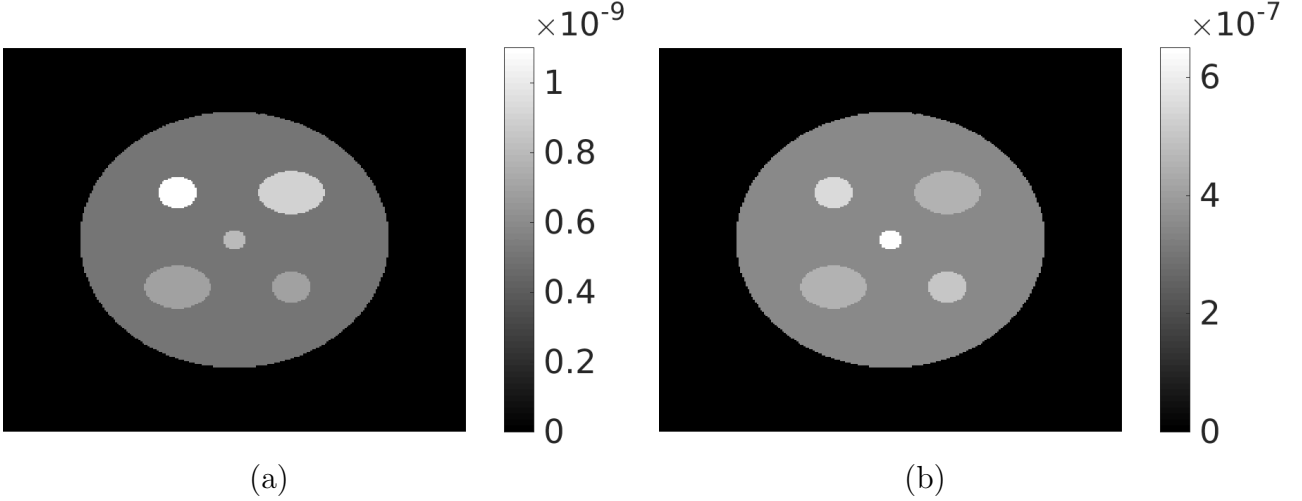
Figure 4.1: The phantoms describing the (a) absorption distribution and (b) refractive index distribution.

4.2 Computer-simulation studies

4.2.1 Numerical phantom design

The numerical properties of the JR method were investigated via computer-simulation studies. A numerical phantom consisting of five ellipses was employed in the studies, as shown in Figure 4.1. The absorption and refractive index describe physical properties of tissues. The β and δ values change when the tissue type changes. While their values differ, the β and δ distributions will share a common set of discontinuities. The β and δ values were designed to be non-homogeneous, which means the β/δ ratio varies for different portions of the object. The physical size of the phantom was 2.56 cm $\times$ 2.56 cm. When digitized, the phantom was modeled as a 256 pixel $\times$ 256 pixel digital object where each pixel had a dimension of 0.01 cm.

Another group of five numerical phantoms was generated separately for the convexity analysis. These phantoms were generated by placing together several randomly generated Gaussian ellipses, where the number of the ellipses, the center, axis lengths, peak absorption and refractive index values for each ellipse were chosen randomly from different Gaussian distributions.

4.2.2 Simulation of measurement data

The measured intensities were simulated based on Equation(2.15). The incident monochromatic X-ray beams had a wavelength of 0.2 nm. Tomographic measurement data were acquired every 0.5 degree. In total, 720 views were imaged, and at each view angle, 400 measured intensities were obtained. Neighboring measurements have a gap of 0.01 cm in between. The illumination curve was modeled based on a previous experimental calibration [19] and was fitted to a Gaussian distribution $I_{TC} = 0.13 + 0.87 \exp(-\Delta\xi^2/(1.74 \times 10^{-10}\mathrm{m}^2))$ (arbitrary unit).

In generation of realistic measurement data, the line integrals in the Radon transform were calculated analytically, so the imaging model best matches the physical imaging process. The model mismatch between the forward model and reconstruction process is a source of reconstruction inaccuracy and is mitigated by the regularization in the reconstruction process. Additionally, white Gaussian noise with a standard deviation equaling 1% of the noise-less measured intensity, which is similar to the noise level in experimental data [19], was added to the measurement data. This Gaussian noise model is employed for complementary metal oxide semiconductor (CMOS) sensors employed in many EIXPCT systems, and is appropriate to describe the aggregation of complicated sources of noise [30]. The noise level is selected for its similarity to experimentally acquired datasets. Noise models can be refined when a specific experimental setup is employed. For example, Poisson noise, or a hybrid noise model considering both Poisson noise and Gaussian noise, may be more appropriate when photon

counting detectors are employed. The use of complicated noise modeel is beyond the scope of this study and will not be analyzed in detail.

For the convexity study where the topology of the optimization problem is of interest, whether or not the measurement data matches the real-world imaging process is irrelevant. Therefore, for ease of discussion and analysis, we generated idealized measurement data based on Equation (3.1), employing the same discretization in the Radon transformation as in the reconstruction algorithm. Noise was not added to idealized measurement data. Consequently, there was no model mismatch between the forward imaging and reconstruction processes.

4.2.3 Implementation of the reconstruction algorithm

In this work, the reconstruction is based on the JR method introduced in Sec. 3.3.2. A smoothed version of the total variation (TV) penalty [53] was utilized as the regularization term $R(\boldsymbol{\beta}, \boldsymbol{\delta})$. The penalty was defined to be a linear combination of the smoothed TV penalty of $\boldsymbol{\beta}$ and $\boldsymbol{\delta}$:

$$R(\boldsymbol{\beta}, \boldsymbol{\delta}) = l_1 R_{TV}(\boldsymbol{\beta}) + l_2 R_{TV}(\boldsymbol{\delta}), \tag{4.1}$$

where l_1 and l_2 are real-valued regularization parameters. The regularization parameters were chosen empirically by parameter sweeping.

The gradient descent algorithm was implemented for the JR method as described in [9]. The absorption and refractive index distributions were discretized into a 256×256 grid with a pixel size of 0.01 cm. A line search strategy [2] was employed for selecting step sizes in each iteration. The algorithm was stopped when the step size value dropped below a threshold of 1×10^{-20}.

4.3 Convexity

Because a gradient-descent algorithm was employed in the reconstruction method, the convexity of the cost function is important for analyzing convergence [2]. Because $R(\boldsymbol{\beta}, \boldsymbol{\delta})$ is typically defined as a convex function, we focus our study on the convexity of the data fidelity term $f_1(\boldsymbol{\beta}, \boldsymbol{\delta}) \equiv \|\boldsymbol{I}_m - \boldsymbol{I}(\boldsymbol{\beta}, \boldsymbol{\delta})\|^2$.

4.3.1 Theoretical analysis of convexity

Because f_1 is a function of $\boldsymbol{\beta}$ and $\boldsymbol{\delta}$, the problem can be analyzed by first investigating the convexity of the two functions: $f_{1\delta}(\boldsymbol{\delta}) \equiv f_1(\boldsymbol{\beta}, \boldsymbol{\delta})$, given a fixed $\boldsymbol{\beta}$, and $f_{1\beta}(\boldsymbol{\beta}) \equiv f_1(\boldsymbol{\beta}, \boldsymbol{\delta})$, given a fixed $\boldsymbol{\delta}$. A necessary but not sufficient condition for the original problem to be convex is that the two functions are convex.

The first function $f_{1\delta}(\boldsymbol{\delta})$ can be expressed as

$$f_{1\delta}(\boldsymbol{\delta}) = \left\| \boldsymbol{I}_m - [c_1 - c_2 \boldsymbol{D}\boldsymbol{\delta}] \right\|^2 , \tag{4.2}$$

where c_1 and c_2 are real-valued vectors independent of $\boldsymbol{\delta}$. This is a convex function, and the proof for convexity is given in Appendix. B.

The second function $f_{1\beta}(\boldsymbol{\beta})$ is

$$f_{1\beta}(\boldsymbol{\beta}) = \left\| \frac{\boldsymbol{I}_m}{c_3} - \exp\left(-\frac{4\pi}{\lambda} \boldsymbol{H}\boldsymbol{\beta} \right) \right\|^2 , \tag{4.3}$$

where c_3 is a positive constant independent of $\boldsymbol{\beta}$. Although $\boldsymbol{H}$ is a linear operator, the exponential operation makes this function non-convex.

Because the second subproblem is non-convex, the original optimization problem is also non-convex and therefore the optimization may become trapped in a local minimum.

4.3.2 Empirical verification of non-convexity

To demonstrate that an inappropriate initial guess can lead the optimization to a local minimum in JR, a simulation test was conducted. The idealized measurement data were simulated for one of the random phantoms and the JR method was applied. No regularization was employed because the idealized measurement data were free of model mismatch and noise. Random initial guesses for $\boldsymbol{\beta}$ and $\boldsymbol{\delta}$ were employed in this study. The initial guess for $\boldsymbol{\beta}$ was a vector whose elements follow the zero-mean Gaussian distribution with standard deviation $\sigma_\beta = 1 \times 10^{-10}$, and the initial guess for $\boldsymbol{\delta}$ was also a vector containing elements following zero-mean Gaussian distribution but with a different standard deviation $\sigma_\delta = 1 \times 10^{-6}$. Because the idealized measurement data were employed, if the problem is convex, a global minimum should be reached by a gradient descent algorithm where the cost is decreased towards to 0. However, for the reconstruction test case, the cost function value at convergence was 0.0049, while a successful reconstruction of the same sample (as described in the next paragraph) can reach a final cost function value of 0.0001. In addition, as shown in Figure 4.2, neither reconstruction profile exactly matches the phantom profile, indicating poor quality of the reconstructed images. The high cost function value at convergence and erroneous image profiles indicate the solution was trapped in a local minimum.

Fortunately, although the optimization problem is non-convex, an accurate reconstruction can still be obtained by use of a suitably defined initial guess. For all phantoms we have ever tested, we have not observed sub-optimal solutions when zero vectors were used as the initial guesses for both $\boldsymbol{\beta}$ and $\boldsymbol{\delta}$. The effectiveness of using zero initial guesses to avoid local minima can be verified by reconstructing random objects. For all of the five random phantoms

(a) 1.65×10^{-15}

(b)

(c) 3.97×10^{-22}

(d)
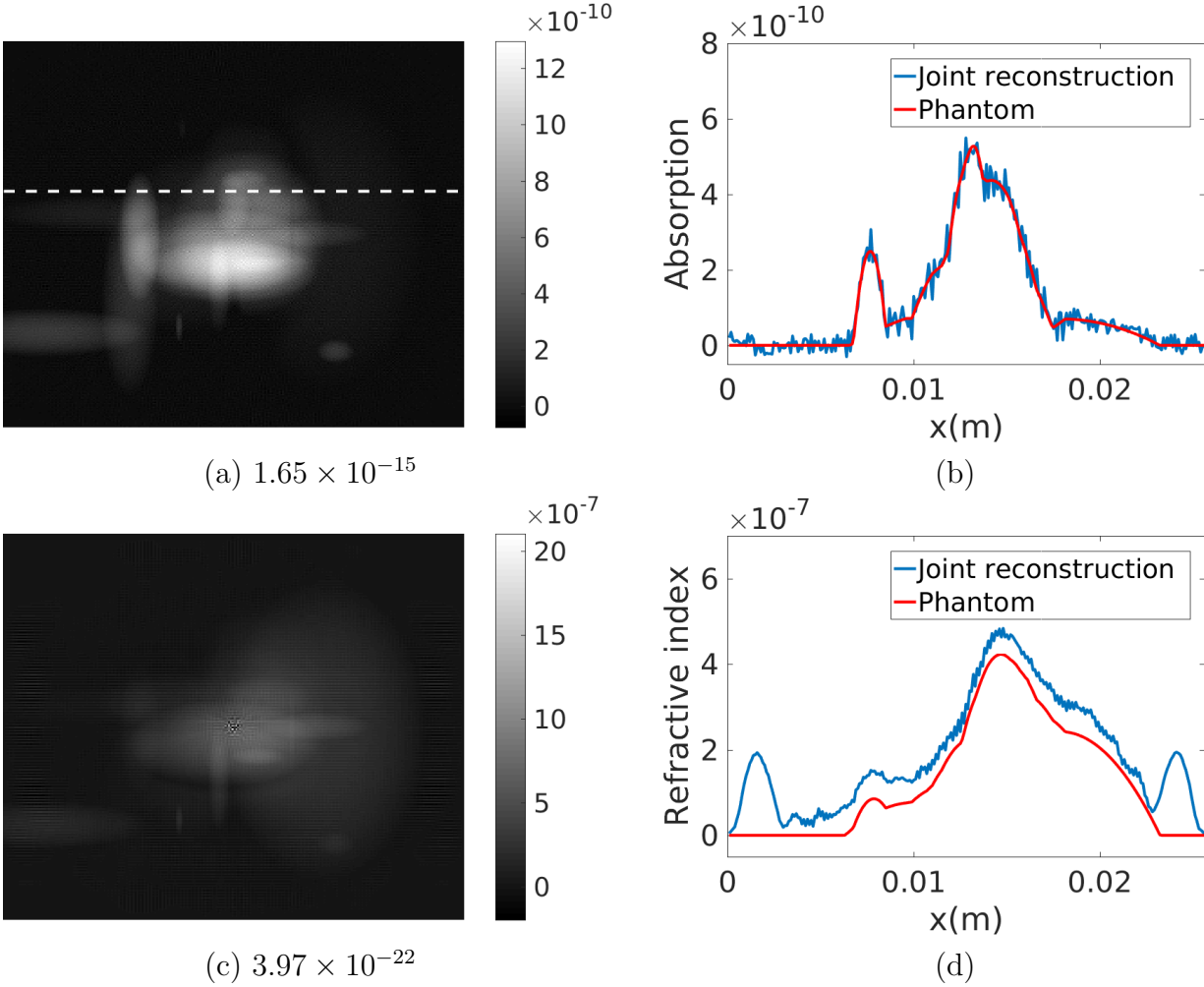
Figure 4.2: The reconstructed images and the corresponding profiles corresponding to a random phantom when a noisy initial guess is employed. (a) The reconstructed absorption distribution. (b) The profiles (at 100-th row as indicated by the dotted line) of the reconstructed and the actual absorption distributions. (c) The reconstructed refractive index distribution. (d) The profiles (at 100-th row) of the reconstructed and the actual refractive index distributions. The mean square errors (MSE) are indicated below the figures.

2.52×10^{-24} 1.15×10^{-19}

1.94×10^{-24} 2.63×10^{-19}

2.35×10^{-24} 3.67×10^{-19}

6.67×10^{-25} 5.92×10^{-19}

1.93×10^{-24} 4.16×10^{-19}

(a)   (b)   (c)   (d)
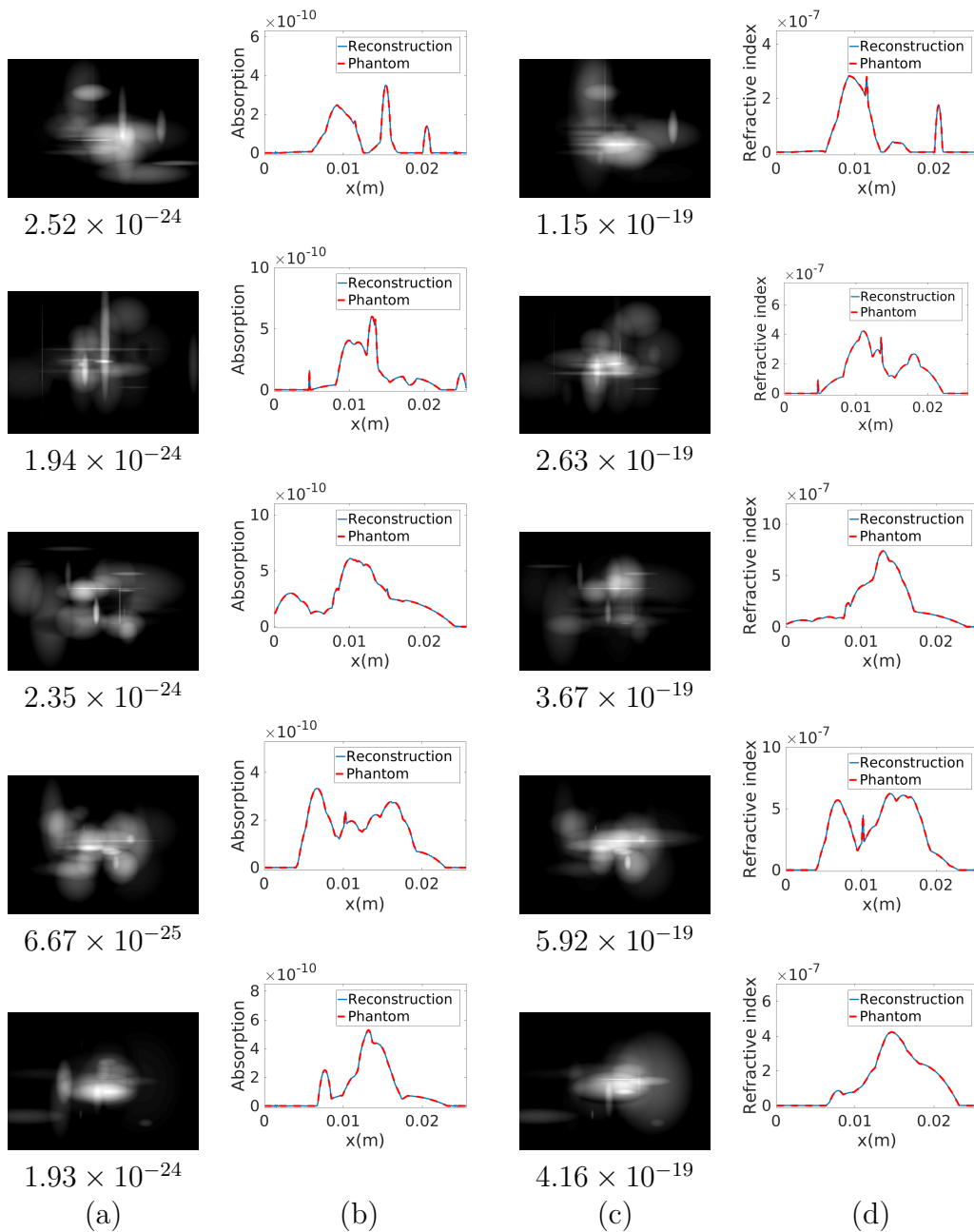
Figure 4.3: The reconstructed images and their corresponding profiles for 5 random phantoms. Each column represents: (a) the reconstructed absorption distribution, (b) the profiles (at 100-th row) of the reconstructed and the actual absorption distributions, (c) the reconstructed refractive index distribution, (d) the profiles (at 100-th row) of the reconstructed and the actual refractive index distributions. The mean square errors (MSE) are indicated below the figures.

described in the previous section, the JR method with no regularization was applied to the idealized measurement data. Both $\boldsymbol{\beta}$ and $\boldsymbol{\delta}$ employed zero vectors as initial guesses. The reconstructed images and their comparison to their corresponding phantoms are given in Figure 4.3. After convergence, all of the reconstructed images look close to the phantom and the image profiles match the phantom profiles well, suggesting that the optimization converged without falling into a local minimum. These reconstructed images demonstrate that the JR method can reliably estimate the absorption and refractive index distributions with a zero initial guess, despite the cost function being non-convex.

4.4 Cross-talk effect

To fully understand how the two reconstruction channels affect each other in the JR method, two studies were designed to investigate the ability of each channel to evolve relatively independently and robustly without much reliance on the other channel.

4.4.1 The effect of error in one channel upon the other channel

This study was designed to investigate how errors in one channel (in the form of noise or blurring) may affect the other. One channel was fixed at a predefined suboptimal object property map, and the other channel was reconstructed by minimizing the functions shown in either Equation (4.2) or Equation (4.3).

The set of realistic measurement data were employed in this test. When reconstructing the refractive index distribution, the absorption distribution was fixed and selected to be the designed phantom with Gaussian noise (denoted by the noisy property map) or Gaussian blurring (denoted by the blurred property map) added. The Gaussian noise had zero mean and a standard deviation of $\sigma_n = 10^{-9}$ rad. The Gaussian blurring kernel was a Gaussian
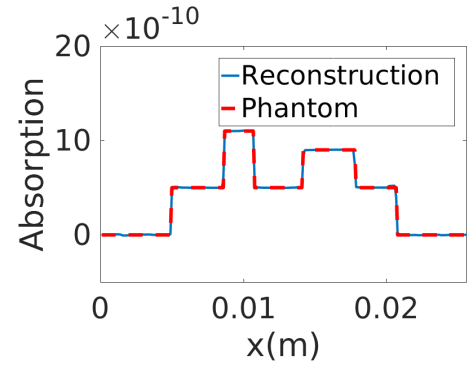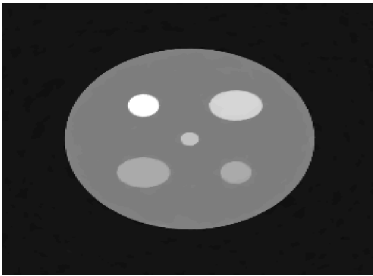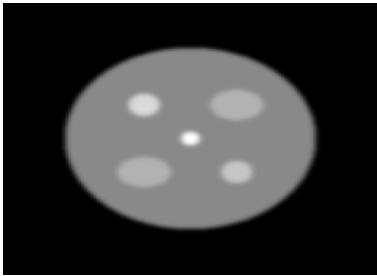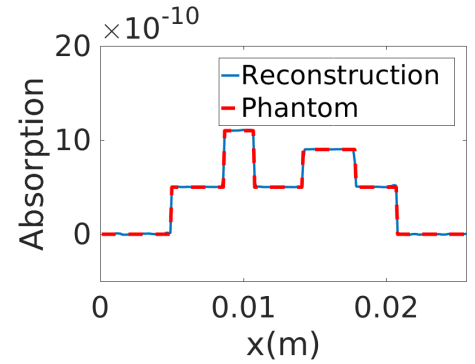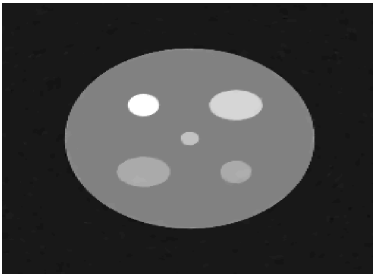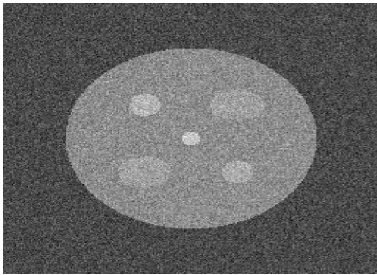
Fixed property map of $\boldsymbol{\delta}$ Reconstructed $\boldsymbol{\beta}$ A profile of reconstructed $\boldsymbol{\beta}$

Figure 4.4: When the refractive index distribution $\boldsymbol{\delta}$ was fixed at a erroneous object property map as shown in the first column (noisy property map in the first row, blurry property map in the second row), the absorption distribution $\boldsymbol{\beta}$ was reconstructed. The reconstructed absorption distribution images are shown in the second column and their corresponding profiles (at 100-th row) are shown in the third column.
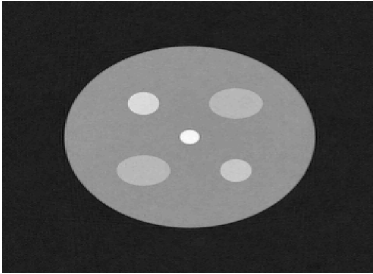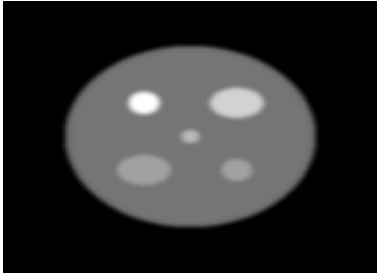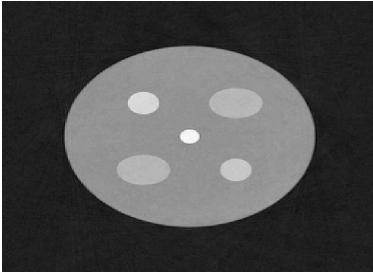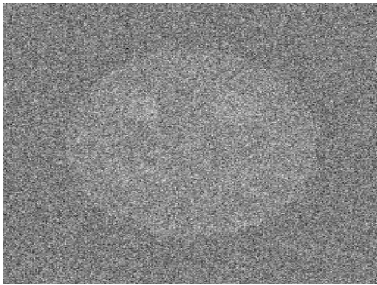
| Fixed property maps of $\boldsymbol{\beta}$ | Reconstructed $\boldsymbol{\delta}$ | A profile of reconstructed $\boldsymbol{\delta}$ |
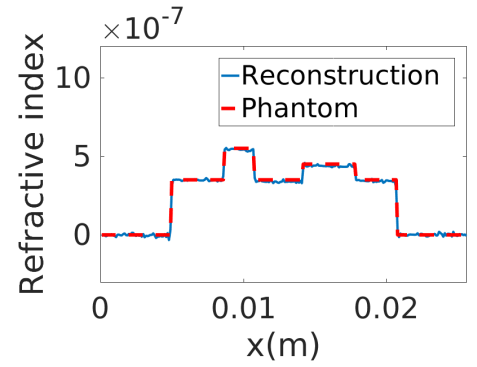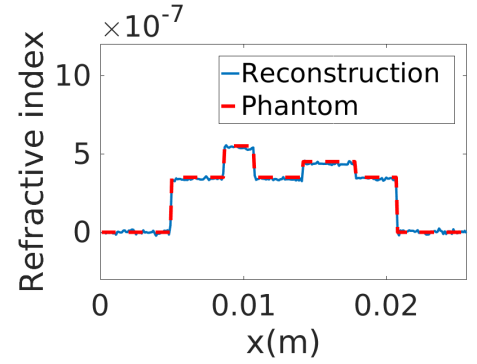
Figure 4.5: When the absorption distribution $\boldsymbol{\beta}$ was fixed at a erroneous object property map as shown in the first column (noisy property map in the first row, blurry property map in the second row), the refractive index distribution $\boldsymbol{\delta}$ was reconstructed. The reconstructed refractive index distribution images are shown in the second column and their corresponding profiles (at 100-th row) are shown in the third column.

function with standard deviation of $\sigma_b = 2 \times 10^{-4}$ m. When reconstructing the absorption distribution, the refractive index distribution was again fixed and selected to be the designed phantom with Gaussian noise or Gaussian blurring added. This time, the Gaussian noise was zero mean and has a standard deviation of $\sigma_n = 10^{-7}$ rad. The Gaussian blurring kernel was the same. The object property maps for the fixed channels were employed because they resemble the intermediate reconstructed images that can be encountered during the iterative reconstruction process with different levels of regularization.

When the refractive index was fixed to be the noisy/blurry object property maps as shown in the first column of Figure 4.4, the reconstructed absorption distributions are shown in the second and third columns of Figure 4.4. Similarly, when the absorption was fixed, the employed object property maps for the absorption and the corresponding reconstructed refractive index distributions are shown in Figure 4.5. Based on the observed reconstructed images, when reconstructing one channel, although the fixed object property maps for the other channel may not be ideal – they either look noisy or blurry – the to-be-reconstructed channel can still obtain a good estimate that is close to the phantom. In conclusion, the error in one channel does not impose a significant influence upon the other channel in the JR method. This observation suggests that the two channels in JR are evolving on relatively independent tracks, indicating the robustness of the method.

4.4.2 The effect of the value of one channel upon the the gradient of the other channel

To further test the hypothesis that cross-talk is weak in JR, the gradients calculated in the gradient descent iterations were considered. For the gradient descent algorithm, the gradients of both channels were calculated based on the values of both channels from the previous

(a) accurate property map

(b) zero property map

(c) noisy property map

(d) blurred property map
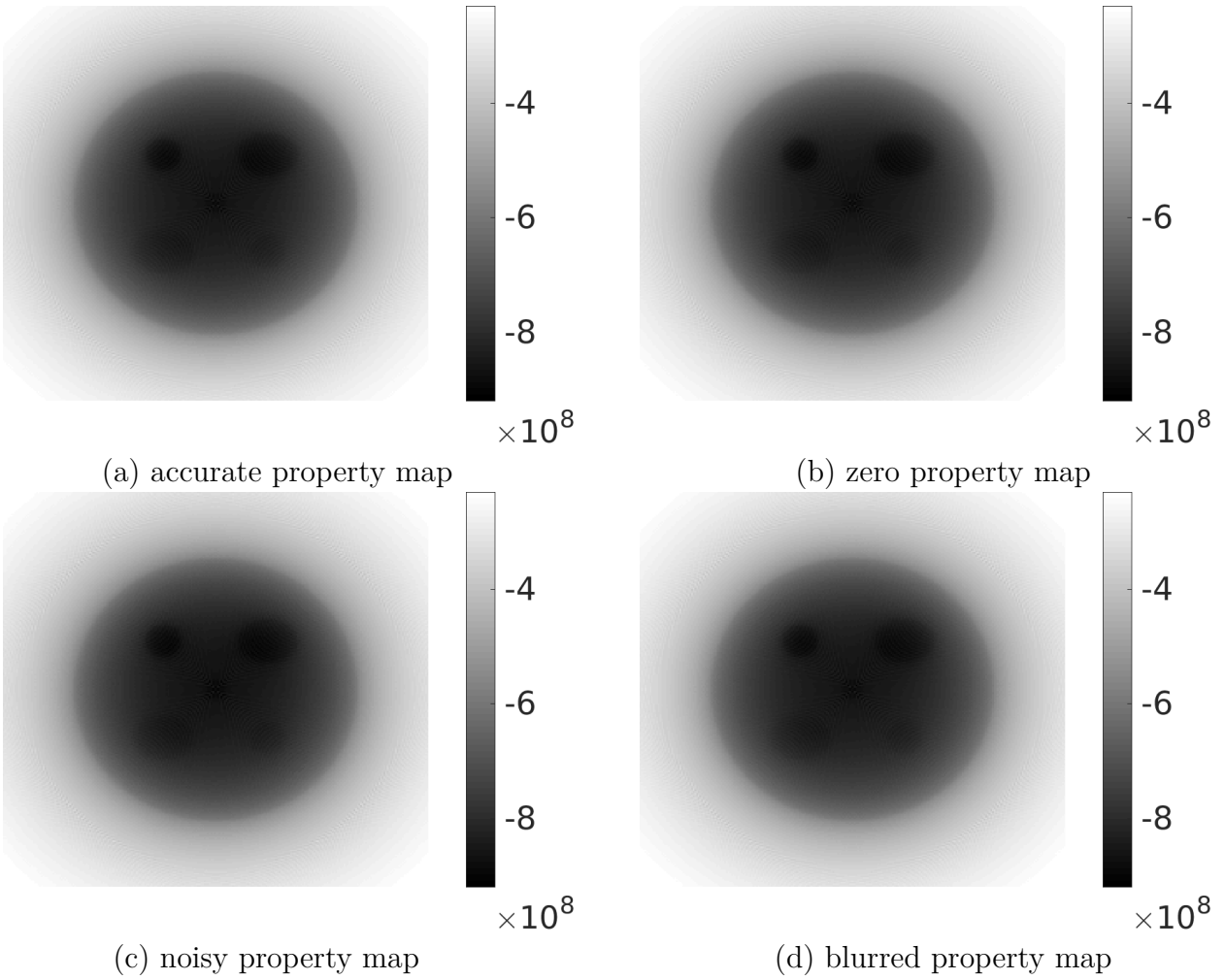
Figure 4.6: When $\boldsymbol{\beta}$ takes a zero vector as the initial guess, the gradient of the JR cost function with respect to $\boldsymbol{\beta}$ are displayed when different fixed property maps are employed for $\boldsymbol{\delta}$

(a) accurate property map

(b) zero property map

(c) noisy property map

(d) blurred property map
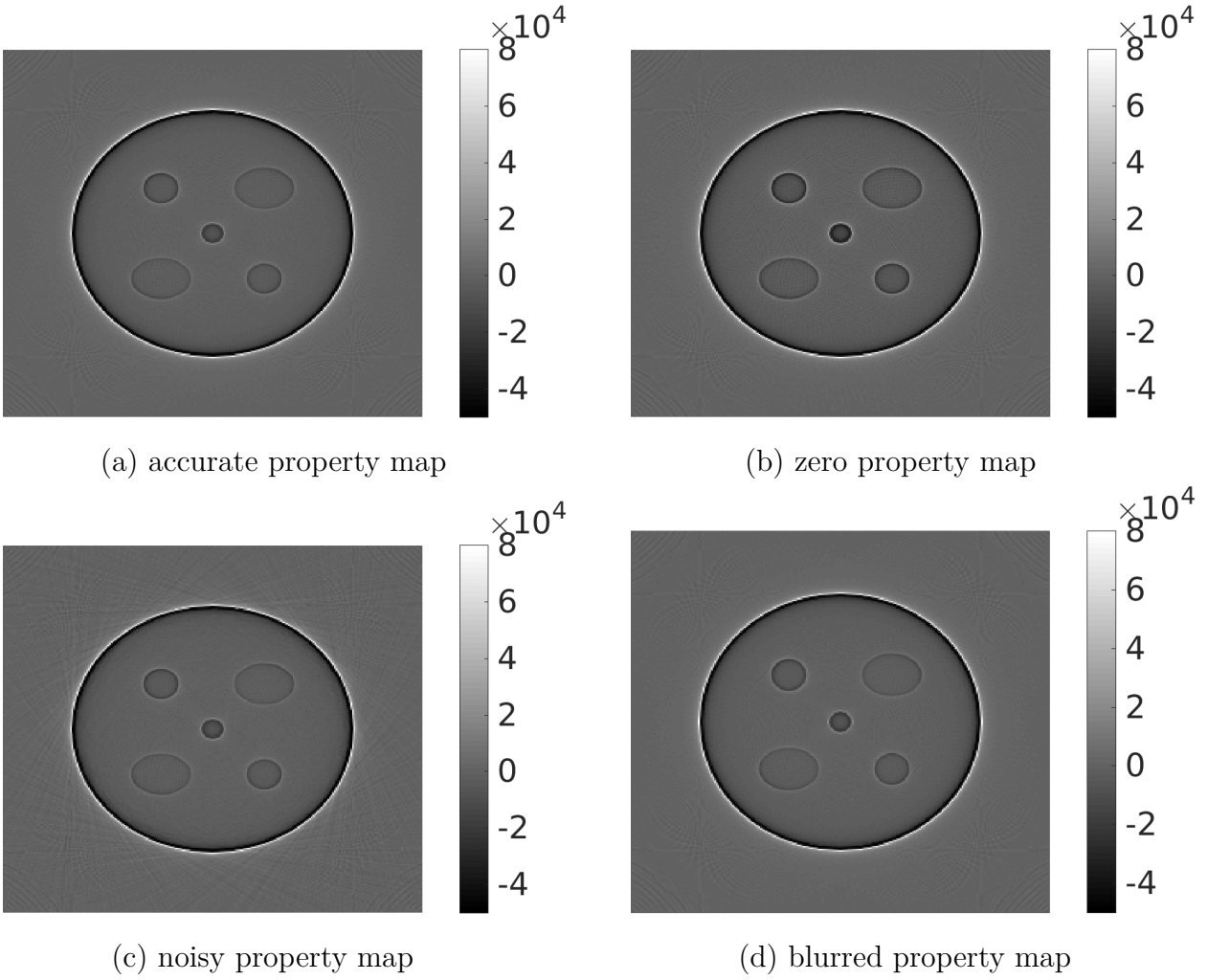
Figure 4.7: When $\boldsymbol{\delta}$ takes a zero vector as the initial guess, the gradient of the JR cost function with respect to $\boldsymbol{\delta}$ are displayed when different fixed property maps are employed for $\boldsymbol{\beta}$
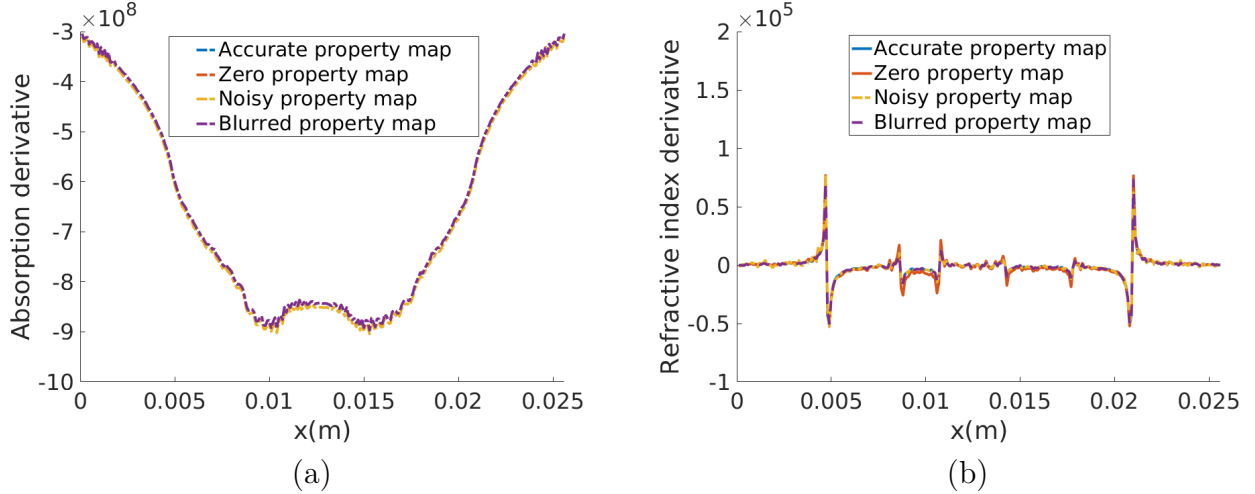
Figure 4.8: Profiles through the gradient maps in (a) Figure 4.6 and (b) Figure 4.7.

iteration. Consequently, if the gradient for one channel is almost independent of the values of the other channel, the two channels can be reasonably treated as independent. In this study, we compared gradients of one channel with a zero initial guess when different object property maps of the other channel were selected: (a) the accurate property map, which takes the values of the designed phantom; (b) the zero property map, which is all 0s for the other channel; (c) the noisy property map and (d) the blurred property map as defined in Sec. 4.4.1. The gradients with respect to $\boldsymbol{\beta}$ are shown in Figure 4.6, and the gradients with respect to $\boldsymbol{\delta}$ are shown in Figure 4.7. A comparison of the profiles of the gradients is given in Figure 4.8. It can be seen that the gradients are almost the same when the other channel employs different object property maps, indicating little cross-talk effect.

4.5   Statistical properties of the images

In this component of study, the biases and variances of images reconstructed by use of the JR method with five different sets of regularization parameters were compared with the biases and variances of images reconstructed by use of the conventional two-step method. For the

46

Table 4.1: The regularization parameters employed in the bias-variance analysis (from no cutoff to large cutoff for CVN-FBP, from small regularization to large regularization for CVN-TV and JR TV, from right to left for all three methods as shown in the figure)

cutoff frequency (CVN-FBP)	TV parameter for $\boldsymbol{\beta}$(CVN-TV)	TV parameter for $\boldsymbol{\delta}$(CVN-TV)	TV parameter for $\boldsymbol{\delta}$ (JR-TV)
1, 0.9, 0.8, 0.7, 0.6, 0.5, 0.4, 0.3	1×10^{-16}, 3×10^{-16}, 1×10^{-15}, 3×10^{-15}, 1×10^{-14}	1×10^{-13}, 3×10^{-13}, 1×10^{-12}, 3×10^{-12}, 1×10^{-11}	4×10^2, 2×10^3, 4×10^3, 1×10^4, 5×10^4

conventional method, we simulated images at two different sample mask positions for a total of 360 view angles in order to guarantee that both the JR method and the conventional method employed the same amount of measured intensity values as input. For the reconstruction step in the two-step approach where the two distributions were obtained with their corresponding sinograms, two methods were employed. The first method was the FBP method, which has been widely used for reconstruction of EIXPCT images. This method is denoted by CVN-FBP. The Ram-Lak filter was employed with high-frequency cutoffs to demonstrate the effect of regularization. The second method employed the gradient descent algorithm to solve two optimization problems with TV regularization for both channels:

$$\hat{\boldsymbol{\beta}} = \arg\min_{\boldsymbol{\beta}} \|\boldsymbol{S}_1 - H\boldsymbol{\beta}\|^2 + l_1' R_{TV}(\boldsymbol{\beta}), \tag{4.4}$$

$$\hat{\boldsymbol{\delta}} = \arg\min_{\boldsymbol{\delta}} \|\boldsymbol{S}_2 - H\boldsymbol{\delta}\|^2 + l_2' R_{TV}(\boldsymbol{\delta}). \tag{4.5}$$

where $\boldsymbol{S}_1$ and $\boldsymbol{S}_2$ are the sinograms corresponding to $\boldsymbol{\beta}$ and $\boldsymbol{\delta}$, respectively, and were obtained in the phase-retrieval step. Different regularization parameters l_1' and l_2' were tested. This method is denoted by CVN-TV. The regularization parameters and cutoff parameters employed are summarized in Table 4.1.

The bias and variances were estimated by analyzing the statistics of an ensemble of reconstructed images. An ensemble of 300 realistic measurement datasets for the same phantom
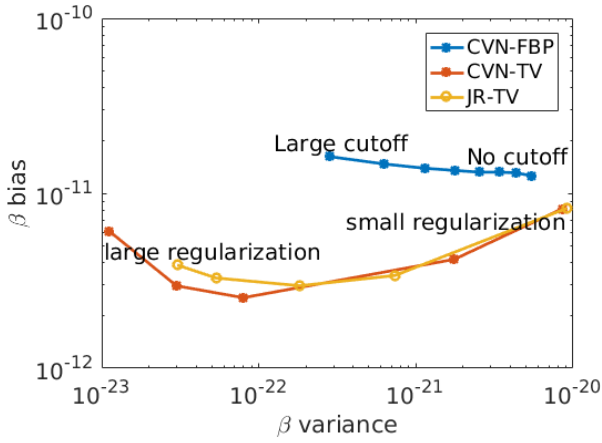
Bias-variance plot for reconstructed $\boldsymbol{\beta}$
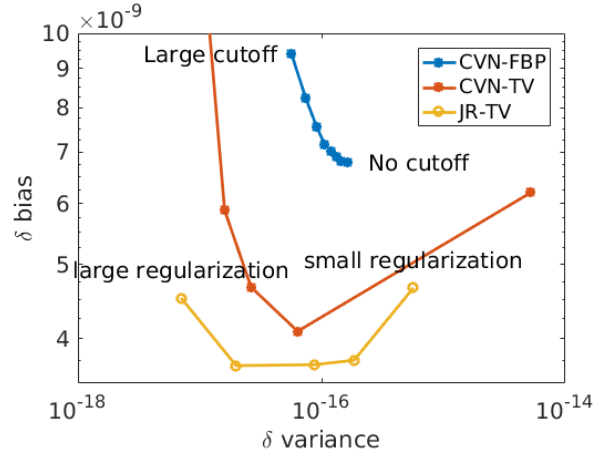
Bias-variance plot for reconstructed $\boldsymbol{\delta}$

Figure 4.9: The bias-variance plot for reconstructed $\boldsymbol{\beta}$ and $\boldsymbol{\delta}$. For the CVN-FBP methods, different high frequency cutoff values were selected for the Ram-Lak filter in the FBP algorithm. For the CVN-TV method, different regularization parameters were employed for the reconstruction of $\boldsymbol{\beta}$ and $\boldsymbol{\delta}$ separately. For the JR method, different sets of regularization parameters were employed. The ratio between the $\boldsymbol{\beta}$ penalty (l_1) and $\boldsymbol{\delta}$ penalty (l_2) was kept constant ($l_2/l_1 = 0.002$). The parameters tested are summarized in Table 4.1. Note that for JR-TV, the ratio of l_1 and l_2 is a constant so only the l_2 parameters are listed.

with different realizations of Gaussian noise added were generated for each test case and reconstructed by the three reconstruction methods. Given the reconstructed $\boldsymbol{\beta}$ and $\boldsymbol{\delta}$ images, the ensemble bias image and variance image are defined as

$$\text{bias}(\{\boldsymbol{u}^k\}) = \left| \frac{1}{K} \sum_{k=1}^{K} \boldsymbol{u}^k - \boldsymbol{u}_0 \right|, \tag{4.6}$$

and

$$\text{var}(\{\boldsymbol{u}^k\}) = \frac{1}{K-1} \sum_{k=1}^{K} \left(\boldsymbol{u}^k - \frac{1}{K} \sum_{k=1}^{K} \boldsymbol{u}^k \right)^2. \tag{4.7}$$

Here, $\boldsymbol{u}$ can be either the reconstructed $\boldsymbol{\beta}$ or $\boldsymbol{\delta}$. The value K is the total number of samples in the ensemble which takes the value of 300 in this study, and $\boldsymbol{u}^k$ denotes the k-th sample $(k = 1, 2, ..., K)$. The notation $\{\boldsymbol{u}^k\}$ represents the whole ensemble of reconstructed $\boldsymbol{\beta}$ or $\boldsymbol{\delta}$, and $\boldsymbol{u}_0$ denotes the corresponding phantom image vector. The $(\cdot)^2$ and $|\cdot|$ operators describes element-wise operations.

To produce scalar-valued summary measures, the bias image and variance image were averaged over all pixels to produce two scalars describing the overall bias and variance level of the reconstructed images. The acquired bias-variances relationships are given in Figure 4.9. For all of the three methods, regularization parameters (or frequency cutoff values) should be carefully selected. Too small of a penalty value leads to high variance while too large penalty leads to high bias. Because both the bias and variance are simultaneously lower for the JR method than for the CVN-FBP method, it can be concluded that JR with proper regularization outperforms the CVN-FBP method in producing reconstructed images with higher quality.

The improvements may either come from the iterative, implicit phase retrieval process in the JR method, or the TV regularization employed. The bias-variance information form the CVN-TV method confirms that both factors are playing a role. First, the fact that CVN-TV

method also outperforms CVN-FBP method suggests that the iterative reconstruction with TV regularization is effective in reducing noise compared with FBP implementing a high frequency cutoff. Second, the JR method has lower noise level of $\boldsymbol{\delta}$ compared with the conventional method even after the conventional method has employed the TV regularization. Note that the noise levels of $\boldsymbol{\beta}$ for CVN-TV and JR-TV are comparable. Therefore, switching from CVN-TV to JR-TV yields a net gain in overall image quality. This shows that the way the JR method separates the absorption and phase information is effective in improving image quality of the reconstructed refractive index distribution. The absorption-phase information separation is iteratively refined in the JR method, which is better than a one-step separation employed in the conventional method. In conclusion, both of the factors help improve image quality in the JR reconstruction.

4.6   Conclusion

In this project, the properties of the proposed JR reconstruction method for EIXPCT were explored. The optimization problem is non-convex, but the accurate reconstructed images of random phantoms suggests that the non-convexity may not be a significant obstacle if zero initial guesses are employed. This conclusion guides the selection of initial guesses in the JR algorithm. During the reconstruction process of JR, the two channels exhibit little cross-talk effect, which suggests the robustness and reliability of the algorithm. Finally, the noise statistics of reconstructed images were studied and compared. JR with proper regularization yields smaller reconstruction error compared with conventional methods due to its iterative nature of implicit phase retrieval as well as its regularization. This observation demonstrates the advantage of the JR method over the conventional two-step approach.

50

Chapter 5

Comparison of Data-Acquisition Designs for use with Non-Linear Joint Reconstruction for Single-Shot Edge Illumination X-ray Phase-Contrast Tomography

On the one hand, the JR method provides a flexible framework for various approaches of acquiring measurement data. On the other hand, the data-acquisition should be optimized so that it can best coupled with the JR method. In this study, several promising data-acquisition designs will be compared based on their implementation complexity and the reconstruction quality with the joint reconstruction method in computer simulation studies. The pros and cons will be comprehensively studied. In this work, to solve the optimization problem, the fast

iterative soft-thresholding algorithm (FISTA) with backtracking is employed. The algorithm is stopped when the step size determined by the backtracking is smaller than an empirically set threshold.

The remainder of the chapter is organized as follows. In Section 5.1, the simulation study and candidate mask-displacement strategies are introduced. Then, in Section 5.3, the tomographic scanning requirements for stably implementing JR using the different mask-displacement strategies are investigated in an idealized situation, and cross-talk is also discussed. Section 5.4 provides a deeper understanding of how the data-acquisition designs affect image quality in terms of contrast-to-noise ratio and resolution. Experimental results corresponding to different data-acquisition designs are presented in Section 5.5. Finally, a summary of the promising data-acquisition designs and their properties is provided in Section 5.6.

5.1 Single-shot mask-displacement strategies and data-acquisition designs

Numerical studies were conducted to assess how data-acquisition designs affect image reconstruction quality when the JR method is employed. Different data-acquisition designs were considered that utilized distinct strategies to specify the mask-displacement $\Delta\xi_\theta$ at each view angle, as introduced in Sec. 2.1. These strategies are referred to as mask-displacement strategies. This section introduces three different single-shot mask-displacement strategies: the constant mask position (CAP) strategy, the alternating mask position (AAP) strategy, and the piece-wise constant mask position (PCAP) strategy[1]. The mask-displacement strategy used for the conventional multiple-shot two-step reconstruction method will be referred to as the conventional (CVN) strategy.

---

[1]Historically, the masks were called apertures, and thus the "A" in the abbreviations stands for the word "aperture". Now, we generally call them masks instead of apertures, but we still keep the same abbreviation.

As described previously, there exist two mask positions for capturing highest contrast refractive index information, and they are located on opposite sides of the illumination curve. These positions correspond to highest absolute values of the derivatives of the illumination curve [36] and will be referred to as Position 1 and 2 below. In the CVN strategy, images are acquired at both of these positions at all tomographic view angles. The single-shot mask-displacement strategies require acquisition of only one image at either of these two mask positions at each tomographic view angle. However, they vary in how the mask positions are specified at each tomographic view angle. In the CAP strategy, the mask position is fixed and does not vary with tomographic view angle. In the AAP strategy, the mask position alternates between the two positions as a function of tomographic view angle. The PCAP strategy requires a more complicated data-acquisition process. The mask is placed at position 1 for v consecutive view angles and v images acquired. Then, it is switched to position 2 for the next v view angles and another v images taken. Then, it is switches back to position 1 for another v view angles, and so on. In this study, two different v values are tested, yielding two versions of PCAP strategies: PCAP-60 for $v = 60$ and PCAP-180 for $v = 180$. The mask-displacement strategies are illustrated in Figure 5.1.

Mask-displacement strategies specify the general data-acquisition strategy. However, to uniquely describe a data-acquisition design, the angular step ($\Delta\theta$), number of tomographic view angles acquired (N), and total angular scanning range (θ_a) need to be specified. For clarification, we denote a data-acquisition design as a combination of a mask-displacement strategy together with the three acquisition parameters ($\Delta\theta, N, \theta_a$). For the single-shot designed considered here, the three parameters have the relationship:

$$\theta_a = N\Delta\theta. \tag{5.1}$$
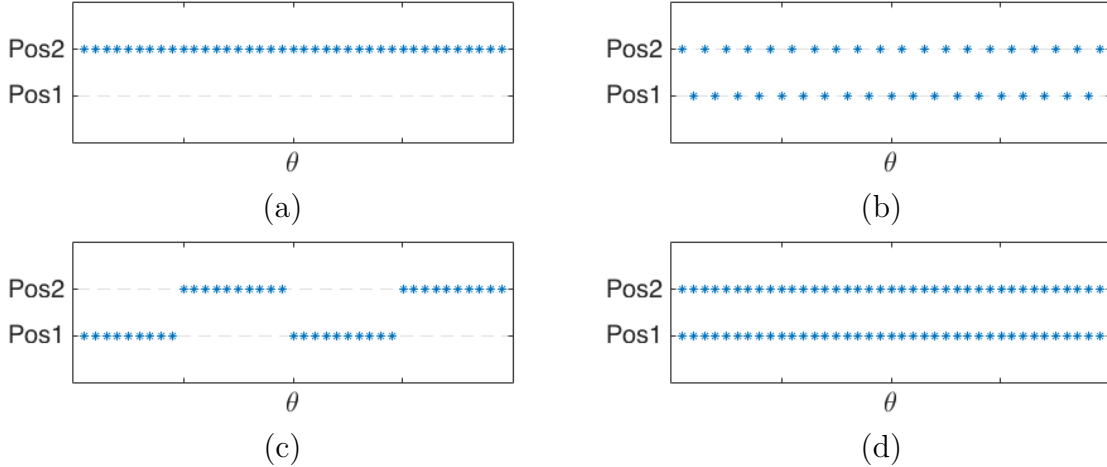
Figure 5.1: Different mask-displacement strategies: (1) CAP strategy, (2) AAP strategy, (3) PCAP strategy, (4) CVN strategy. Each asterisk indicates one image acquired at position 1 or position 2 at the specified tomographic view angle.

Therefore, only two independent parameters are needed. In this study, the angular step is selected to be 0.5° in all test cases. Accordingly, a data-acquisition design can be fully determined by a mask-displacement strategy and the angular scanning range. Data-acquisition designs will be denoted by the notation **strategy(θ_a)**. For example, PCAP-60(1π) specifies the PCAP-60 design with angular scanning range of 1π. Given the fact that $\Delta\theta = 0.5$, in total, 360 projection images are acquired during this data-acquisition process. The mask position is changed every 60 views, or equivalently, every 30°.

5.2   Simulation study design

5.2.1   Phantom designs

Digital and analytical phantoms   Both digital and analytic object phantoms were employed. Here, a digital phantom was modeled as a 2-dimensional (2D) matrix. The line integral data for a digital phantom was implemented as the weighted sum of the pixels' values

along the line trajectory, where the weight for any specific pixel was proportional to the line segment length inside the pixel. Analytical phantoms were formed by a collection of simple geometries where all parameters needed to determine the shapes and locations of the geometries were specified. The line integral data for an analytical phantom were calculated analytically.

First phantom: Analytical geometry phantom   The geometry phantom was an artificial phantom made up of simple shapes, such as ellipses and rectangles, as shown in Figure 5.2a and Figure 5.2b. The largest circle was assigned δ and β values representative of adipose tissue and all the small structures inside were assigned the same δ and β values representative of soft tissues [24]. The bars at the top of the phantom were of dimension 1 mm$\times$200 μm, and the bar at the bottom was 1 mm$\times$300 μm. The ellipses-shaped phantom's major axis was 2 cm, and the minor axis was 1.4 cm. The small ellipse's major axis was 0.8 mm, and the minor axis was 0.6 mm.

Second phantom: digital digimouse phantom   A digital digimouse phantom [15, 54] employed in this study is shown in Figure 5.2c and Figure 5.2d. This phantom had a pixel size of 100 μm$\times$100 μm.

5.2.2   Simulated measurement data

For the analytical phantom, the measurement data were simulated based on Equation (**??**), where an analytical integration step was implemented to compute the Radon transformation. This simulation was closest to a real-world imaging process, where the objects are inherently continuous. For the discrete phantoms, the discrete integration replaced the analytical integration, and all other steps remained the same. To produce noisy measurement data, an uncorrelated Gaussian noise model was employed. The noise model had zero-mean and
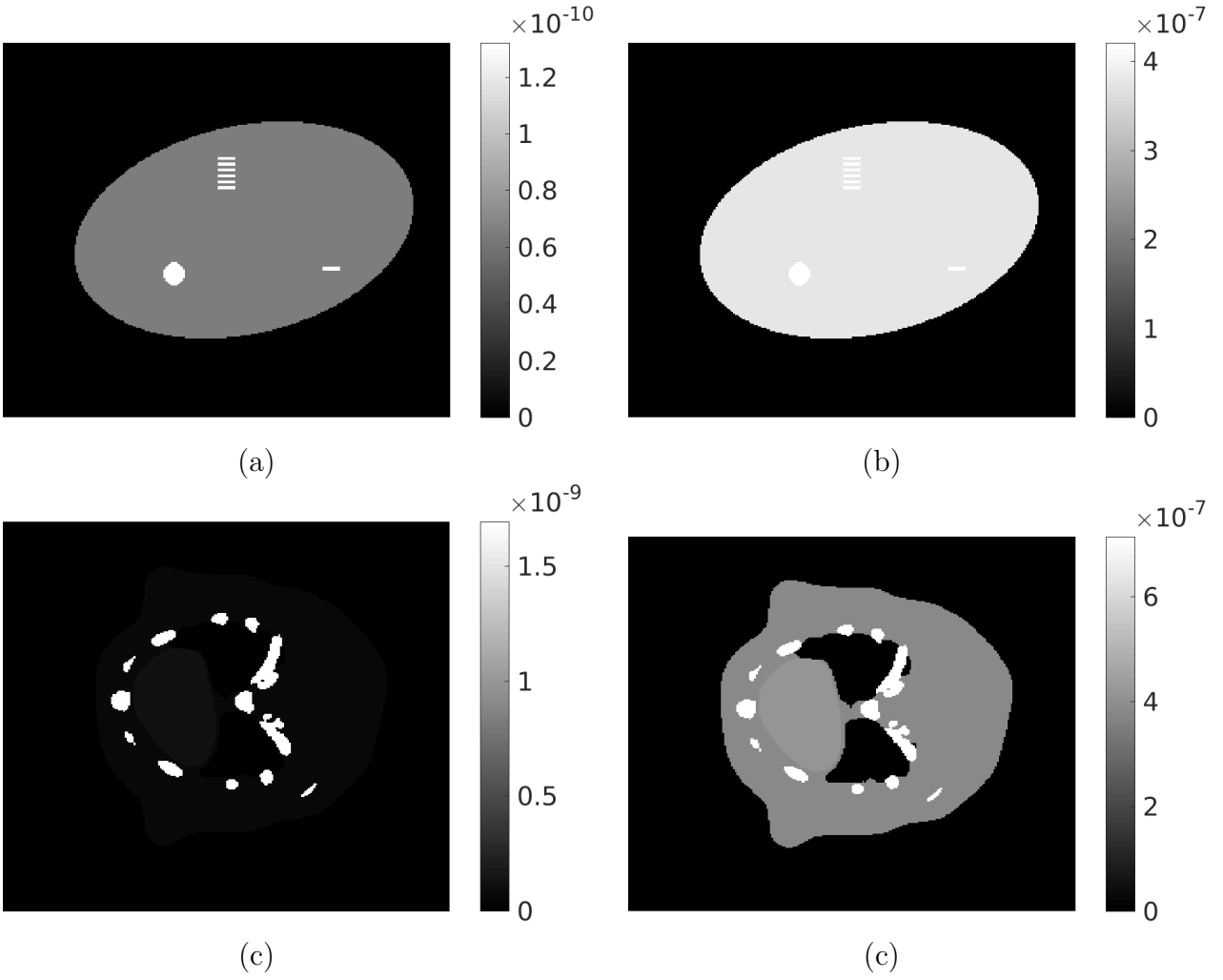
Figure 5.2: The phantoms for (a) (c) absorption distributions and (b) (d) refractive index decrement distributions. (a) and (b) correspond to the geometry phantom; (c) and (d) correspond to the digimouse phantom.

a standard deviation equal to 1% of the noise-less simulated measurement intensity was employed.

5.2.3 Data-acquisition design stability study

In a previous work [7], the optimization problem in Equation (3.8) was shown to be non-convex. In this component of our study, the ability of the JR method to produce accurate image estimates when different data-acquisition designs are employed was investigated.

Effect of tomographic scanning range.   As pointed out in Sec. 5.1, a data-acquisition design requires specifying the mask-displacement strategy as well as the tomographic angular scanning range. The use of different mask-displacement strategies may result in differing requirements over the tomographic angular scanning range. In this part of the study, the minimum required angular scanning range for each mask-displacement strategy was investigated in simulation studies with idealized measurement data. Digital digimouse phantoms were employed as test objects. For each candidate mask-displacement strategy (CAP, AAP, PCAP60, and PCAP180), five sets of simulated measurement data were produced, corresponding to angular range coverages of 180°, 225°, 270°, 315°, and 360°. Reconstructed images were obtained from noise-free measurement data by use of the JR method with no penalty employed. The algorithm was stopped when the stopping criterion was met or at a fixed maximum amount of iterations, whichever was earlier. The reconstructed images were analyzed based on their perceived visual quality as well as on quantitative measurements of their mean square error (MSE) and structural similarity (SSIM) [55]. Smaller MSE values and higher SSIM values indicated more accurate reconstructed images. Promising data-acquisition designs were selected for more detailed analysis.

Cross-talk for each design. The reconstructed $\boldsymbol{\delta}$ and $\boldsymbol{\beta}$ images can be interpreted as two reconstruction channels [51] as described in Chapter 4. Cross-talk refers to image artifacts that occur when the structures in one channel erroneously appear in the other channel. Cross-talk is an important potential problem for any JR method and merits careful study [51]. For the data-acquisition designs identified as promising in the angular range study, cross-talk was assessed. Two sets of cross-talk studies were carried out, with both studies using analytical geometry phantoms.

In the first set of studies, we investigated how errors in one channel could affect the quality of the other channel. In the iterative reconstruction process of the JR method, all subsequent iterations are affected by intermediate reconstruction results. Thus, this study reveals how one channel might evolve when the other channel suffers from suboptimal quality from noise or system inconsistency. Noisy simulated measurement data (1% Gaussian noise) were employed.

Two single-channel reconstruction methods were defined:

$$\tilde{\boldsymbol{\beta}} = \arg\min_{\boldsymbol{\beta} \geq 0} f(\boldsymbol{\beta}, \boldsymbol{\delta}) = \arg\min_{\boldsymbol{\beta} \geq 0} ||\mathbf{I}_m - \mathbf{I}(\boldsymbol{\beta}, \boldsymbol{\delta})||^2 + \alpha_1 R_{TV}(\boldsymbol{\beta}), \quad (5.2)$$

and

$$\tilde{\boldsymbol{\delta}} = \arg\min_{\boldsymbol{\delta} \geq 0} f(\boldsymbol{\beta}, \boldsymbol{\delta}) = \arg\min_{\boldsymbol{\delta} \geq 0} ||\mathbf{I}_m - \mathbf{I}(\boldsymbol{\beta}, \boldsymbol{\delta})||^2 + \alpha_2 R_{TV}(\boldsymbol{\delta}). \quad (5.3)$$

In Equation (5.2) (or Equation (5.3)), $\boldsymbol{\delta}$ (or $\boldsymbol{\beta}$) was fixed but contained errors as described below. The single-channel problems above were solved by use of the FISTA. Ideally, if the two channels are perfectly separable, each channel should be accurately reconstructable regardless of the value assumed for the other one. In this study, when reconstructing $\boldsymbol{\delta}$ via Equation (5.3), $\boldsymbol{\beta}$ was selected to be the actual vector describing the phantom with added Gaussian noise. The Gaussian noise was zero mean and had a standard deviation of 10^{-9}.

When reconstructing $\boldsymbol{\beta}$ via Equation (5.2), $\boldsymbol{\delta}$ was again selected to be the corresponding true phantom with Gaussian noise added. This time, the Gaussian noise was zero mean and had a standard deviation of 10^{-7}. TV regularization was employed, using empirically selected regularization coefficient of $\alpha_1 = 3 \times 10^5$ and $\alpha_2 = 200$.

In the second set of studies, the gradients computed during the reconstruction process were analyzed. If the gradient of $\boldsymbol{\delta}$ computed when solving Equation (3.8) is almost independent of $\boldsymbol{\beta}$, and vise versa, the cross-talk effect is expected to be small. For different data-acquisition designs, we calculated gradients of the $\boldsymbol{\delta}$ channel when $\boldsymbol{\beta}$ was fixed, and analyzed how the value of $\boldsymbol{\beta}$ affects the $\boldsymbol{\delta}$ gradient. To be specific, $\boldsymbol{\delta}$ was selected to be an all-zero vector at the beginning, while $\boldsymbol{\beta}$ took different initial guesses:

- All-zero vector, whose values were all 0s everywhere;

- True phantom vector, which was the ground truth phantom;

- Noisy vector as described above;

- Blurred vector, which was a blurred version of the ground truth phantom. The blurring kernel was a Gaussian function with a standard deviation of $2 \times 10^{-4}\,\mathrm{m}$.

The same approach was employed to analyze how the value of $\boldsymbol{\delta}$ affects the $\boldsymbol{\beta}$ gradient, with the $\boldsymbol{\delta}$ channel taking the same four initial guesses.

Data-acquisition design quality assessment

The candidate data-acquisition designs were compared based on the quality of the reconstructed images. The noise level and resolution of the reconstructed images were analyzed by the MSE analysis and reconstructed profiles for the bar region, respectively.

5.2.4 Experimental validation

Experimental data acquired in a previous study [14] were employed for comparing the data-acquisition designs selected in the computer-simulation studies. The imaged object was a custom-built multiple-component phantom consisting of a hollow plastic cylinder, a plastic rod, a smaller hollow plastic cylinder, rolled plastic paraffin film, and chalk inside a plastic container. A more detailed description of the imaging study and parameters can be found in [14]. Unlike in the previous study, however, ten-step dithering was employed. Due to the dithering, the pixel size in the reconstructed images was 7.9 μ m. The dataset was originally obtained from 720 equally spaced tomographic view angles covering a 2π angular range, and two images were separately obtained at both of the optimal mask positions for each view angle. The original dataset was subsampled to mimic different data-acquisition designs.

5.3 Results: Data-acquisition stability study

5.3.1 Data-acquisition design tomographic scanning requirement in idealized situations

The reconstructed estimates of $\boldsymbol{\delta}$ for different mask-displacement strategies and angular scanning ranges are shown in Figure 5.3. The absorption distribution is of less interest for XPCT imaging, and is thus not shown here. However, it was found that the analysis of the reconstructed refractive index decrement distributions and the absorption distributions led to the same conclusions regarding data-acquisition designs.

The MSE and SSIM values were calculated for the reconstructed $\boldsymbol{\beta}$ and $\boldsymbol{\delta}$, respectively. The relationship between the MSE/SSIM and the angular coverage is shown in Figure 5.4.
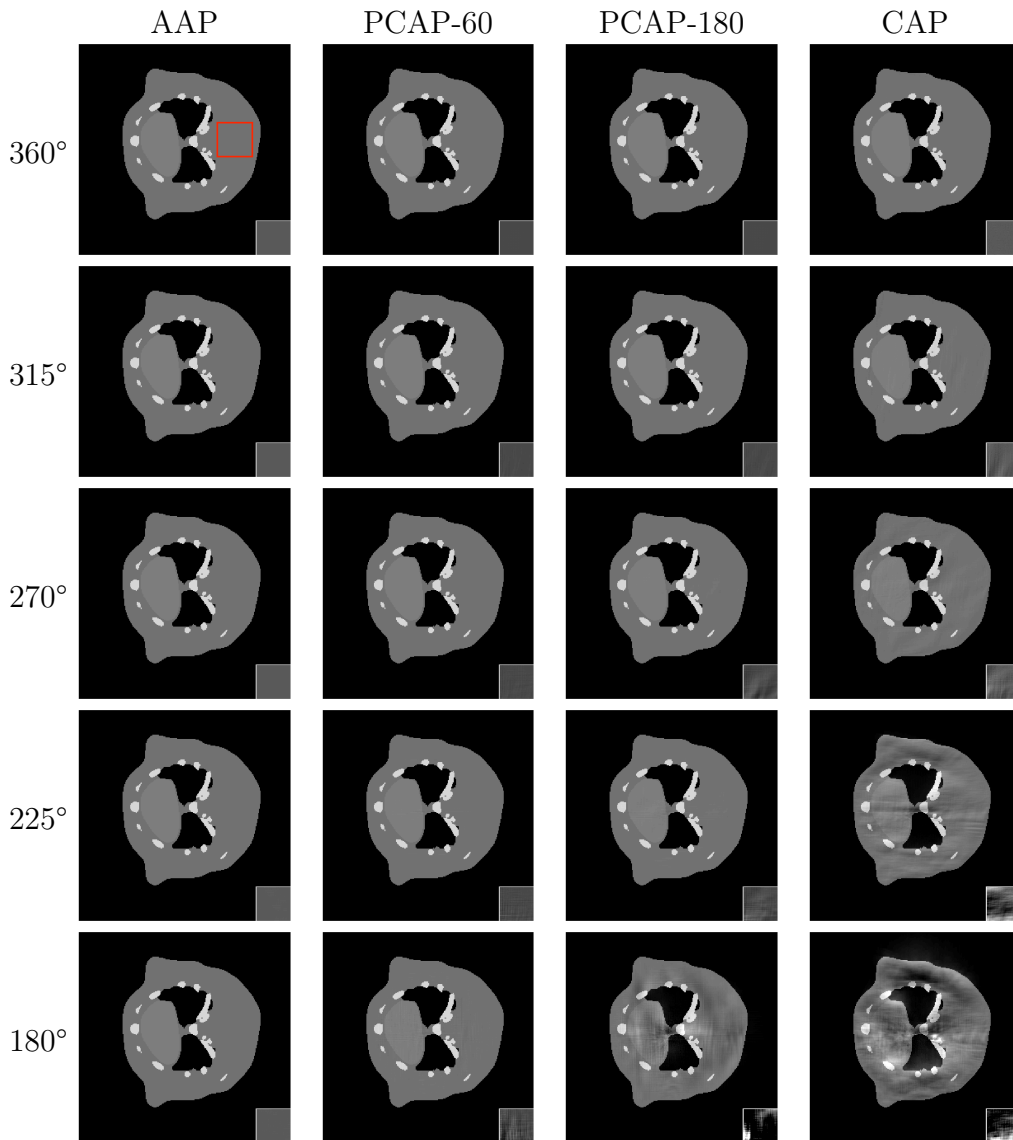
Figure 5.3: The reconstructed estimates of $\boldsymbol{\delta}$ for four different mask-displacement strategies (columns) with different angular ranges (rows). From left to right, the mask position is changed less and less frequently, while the five rows correspond to 180°, 225°, 270°, 315°, and 360°, respectively. All images are displayed in the same gray-scale window. The panel at the bottom-right corner for each reconstructed image is a gray-scale-adjusted view of a uniform region in the reconstructed object, so that fluctuations in intensity can be better visualized.
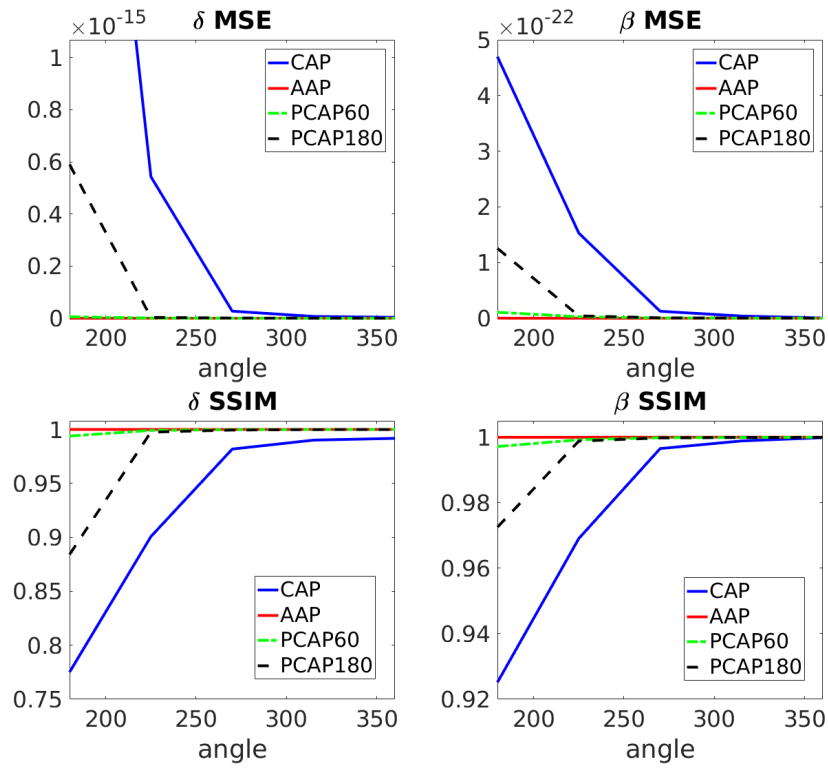
Figure 5.4: The MSE (top row) and SSIM (bottom row) for the reconstructed refractive index decrement distribution $\boldsymbol{\delta}$ and absorption distribution $\boldsymbol{\beta}$ for data-acquisition designs using different mask-displacement strategies and tomographic angular scanning ranges.

For certain data-acquisition designs, image artifacts may appear. In general, the numerical studies suggested that the less frequently the mask is moved and the smaller the total angular coverage, the more artifacts appear in the final reconstructed images. This effect is most prominent with the CAP (1π) design, as shown in Figure 5.3. For some other designs, although the image is free from visually obvious artifacts, it can still contain artifacts. To observe this, a small panel is displayed for each data-acquisition design with a narrower gray-scale window, showing a small region that is supposed to be uniform; this region is marked with the red square in the first image of Figure 5.3. Minor artifacts can be better visualized from the small panel. The quantitative metrics demonstrate a similar trend. Based on Figures 5.3 and 5.4, when the angular coverage increases, all data-acquisition designs result in reduced MSE values and increased SSIM values.

The numerical results suggest that, the more frequently the mask position is changed, the more likely the data-acquisition design is to obtain an artifact-negligible reconstructed image with a smaller angular range coverage. On one extreme, when the AAP strategy is employed, an angular range of 1π was observed to be adequate for obtaining artifact-negligible images. On the other extreme, when the CAP strategy is employed, a 2π angular range was required for artifact-negligible images. The PCAP strategies stand in between.

Since the reconstruction results were obtained from noise-free simulated measurement data utilizing a digital phantom, they reflect the upper-bound performance limit of all these data-acquisition designs. Although many potential designs work well in the idealized setting, only three representative designs were selected for the following in-depth study of the properties: CAP(2π), AAP(2π), and AAP(1π). The differences between the reconstructed images utilizing AAP(2π) and CAP(2π) designs are representative of the effect of decreasing mask movement frequency, and the differences between those utilizing AAP(2π) and AAP(1π) show

63

the effect of decreasing the total angular range. The performance of other data-acquisition designs can be deduced based on the trends revealed by the three representative designs.

5.3.2   Cross-talk effect

The effect of imperfection of one channel on the another channel

For the single-channel reconstruction problem in Equation (5.2), the fixed estimates of $\boldsymbol{\delta}$ as detailed in Sec. 5.2.3 and the corresponding reconstructed $\boldsymbol{\beta}$ are shown in Figure 5.5. For the single-channel reconstruction problem in Equation (5.3), the fixed estimates of $\boldsymbol{\beta}$ and their corresponding reconstructed estimates of $\boldsymbol{\delta}$ are shown in Figure 5.6.

Based on the reconstructed images, although the assigned values for the other channel may not be ideal, the to-be-reconstructed channel was still well estimated. The only exception is for AAP(1π) and a noisy vector assigned for either $\boldsymbol{\beta}$ or $\boldsymbol{\delta}$, where the reconstructed channel is still noisy. This problem, however, can be alleviated by increasing the value of regularization parameter. In conclusion, the quality of one channel does not exert a significant influence on the other channel in the CAP(2π) and AAP(2π) designs. For the AAP(1π) design, the effect exists but can be mitigated by imposing higher regularization.

Impact of crosstalk on cost function gradients

To further understand the cross-talk, the gradients were visualized. For most cases, the gradients of one channel are very similar to each other when the other channel employs different estimates. The $\boldsymbol{\delta}$ gradient is only affected by a noisy $\boldsymbol{\beta}$ vector when the AAP (1π) data-acquisition design is employed, which is best illustrated in the reduced conspicuity of small structures in the AAP (1π) gradient image. This observation suggests that the AAP
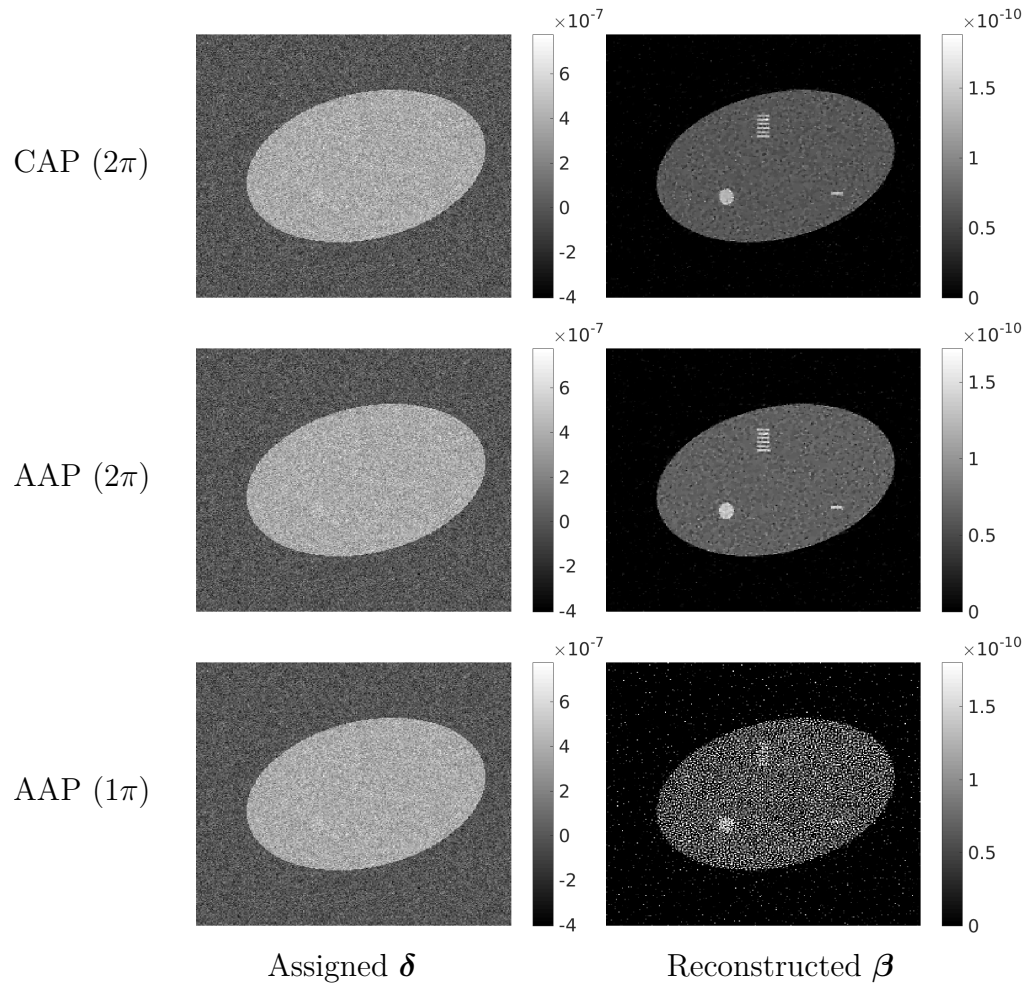
Figure 5.5: Single-channel reconstructed estimates of $\boldsymbol{\beta}$ when imperfect values of $\boldsymbol{\delta}$ are assumed. The left column shows the imperfect assigned values for $\boldsymbol{\delta}$. The right column shows the reconstructed $\boldsymbol{\beta}$ images. Each row corresponds to a data-acquisition design and a specific assigned $\boldsymbol{\delta}$.
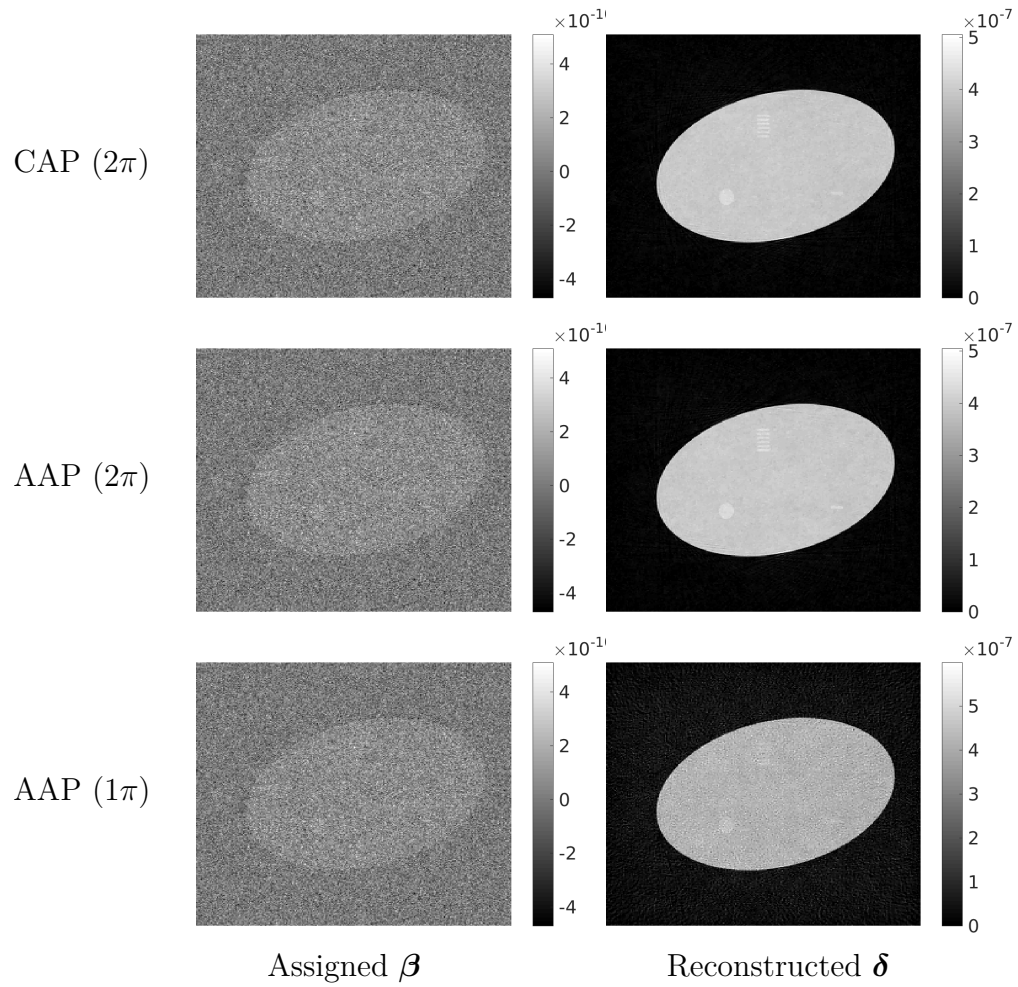
Figure 5.6: Single-channel reconstructed estimates of $\boldsymbol{\delta}$ when imperfect values of $\boldsymbol{\beta}$ are assumed. The left column shows the imperfect assigned values for $\boldsymbol{\beta}$. The right column shows the reconstructed $\boldsymbol{\delta}$ images. Each row corresponds to a data-acquisition design and a specific assigned $\boldsymbol{\beta}$.

CAP(2π)   AAP(2π)   AAP(1π)
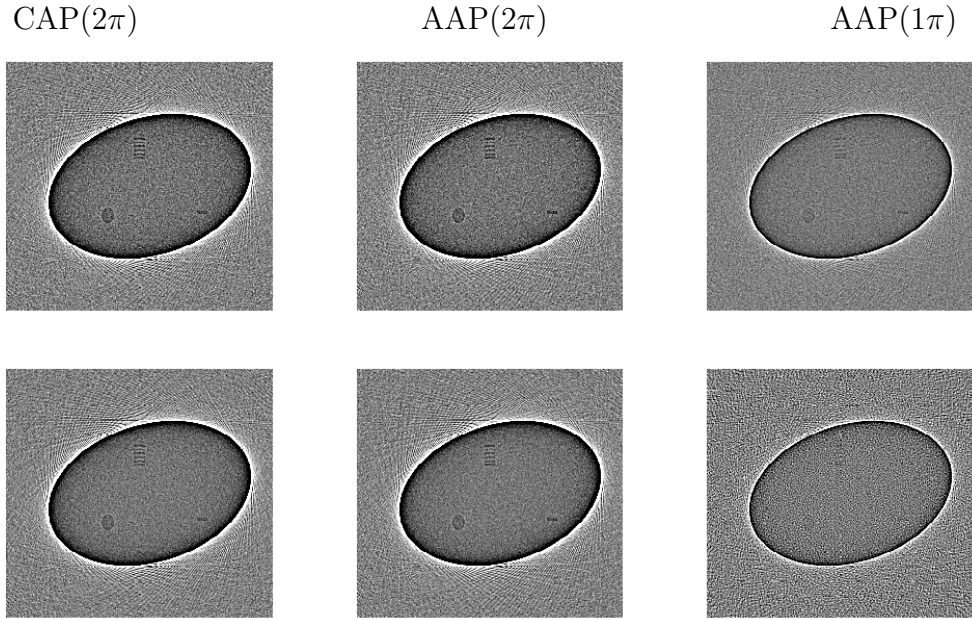
Figure 5.7: The gradient with respect to $\boldsymbol{\delta}$ when $\boldsymbol{\delta} = 0$ and different values are assigned for $\boldsymbol{\beta}$: first row shows when $\boldsymbol{\beta} = 0$; second row shows $\boldsymbol{\beta}$ being the noisy vector defined in Sec.5.2.3.

(1π) design can be affected by cross-talk. In Figure 5.7, the gradients of $\boldsymbol{\delta}$ with $\boldsymbol{\beta}$ being the noisy vector are compared with those with $\boldsymbol{\beta}$ being the all-zero vector. The other $\boldsymbol{\delta}$ gradient images when $\boldsymbol{\beta}$ is the true phantom vector or the blurred vector are not shown here, but are all similar to the results corresponding to the all-zero vector. This finding is consistent with the conclusion from the previous cross-talk effect test, suggesting that the AAP(1π) is more affected by cross-talk, indicating a higher potential for getting trapped in local minima. Thus, special care needs to be taken when choosing the regularization parameters to stabilize the reconstruction.

Table 5.1: Candidate regularization parameters

Distribution	Reg. parameters for AAP(2π) & CAP(2π)	Reg. parameters for AAP(1π)
β	1×10^5, 3×10^5, 1×10^6, 3×10^6, 1×10^7	5×10^4, 1.5×10^5, 5×10^5, 1.5×10^6, 5×10^6
δ	100, 300, 1000, 3000, 10000	50, 150, 500, 1500, 5000

5.4 Data-acquisition quality assessment study

5.4.1 Effect of regularization parameters on image quality

The regularization parameters can significantly affect image quality. Consequently, the effect of regularization parameters is considered first in this section. The trend is similar for all designs, but only the reconstructed images corresponding to the AAP(2π) design are shown here.

The TV regularization parameters for the $\boldsymbol{\beta}$ and $\boldsymbol{\delta}$ distributions were swept on a 2D grid. Five representative regularization values were empirically selected for each of the parameters. The values employed for AAP(2π) and CAP(2π) designs are summarized in Table 5.1. For the AAP(1π) design, the angular coverage range is only half that of the other two designs, thus the data fidelity term is also approximately half that of the other designs covering a 2π angular range. Thus, the candidate regularization parameters were also selected to be half of those for the other two designs.

The reconstructed $\boldsymbol{\beta}$ and $\boldsymbol{\delta}$ estimates corresponding to varying regularization parameters are shown in Figure 5.8 and Figure 5.9. A zoomed-in view of the bar region is shown in Figure 5.10 and Figure 5.11, and a similarly zoomed-in view of the circle region is shown in Figure 5.12 and Figure 5.13.
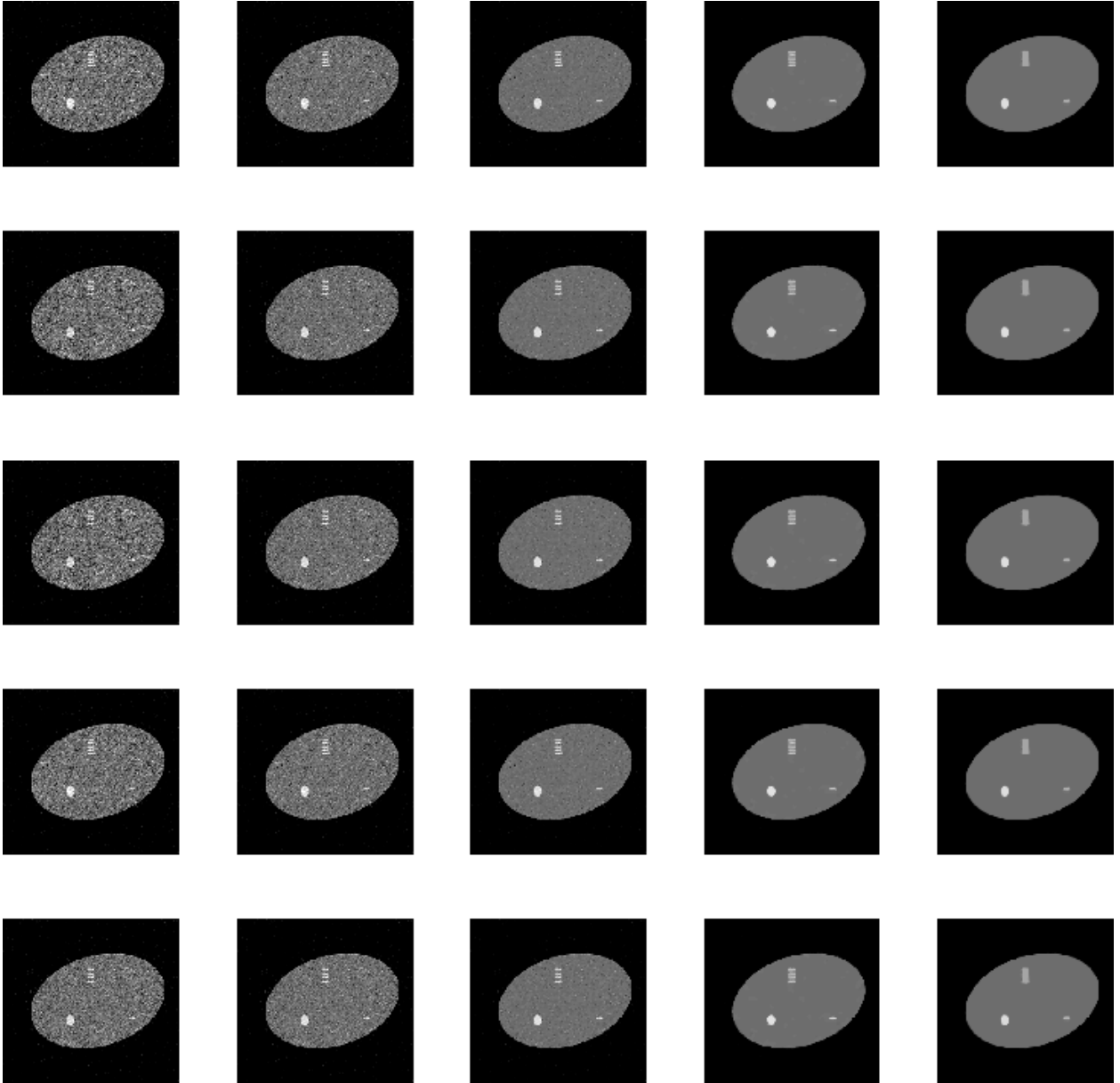
Figure 5.8: The reconstructed $\boldsymbol{\beta}$ image of the analytical geometric phantom for the AAP (2π) design with the different regularization parameters specified in Table 5.1. From left to right, the regularization parameter for $\boldsymbol{\beta}$ is increasing. From top to bottom, the regularization parameter for $\boldsymbol{\delta}$ is increasing.
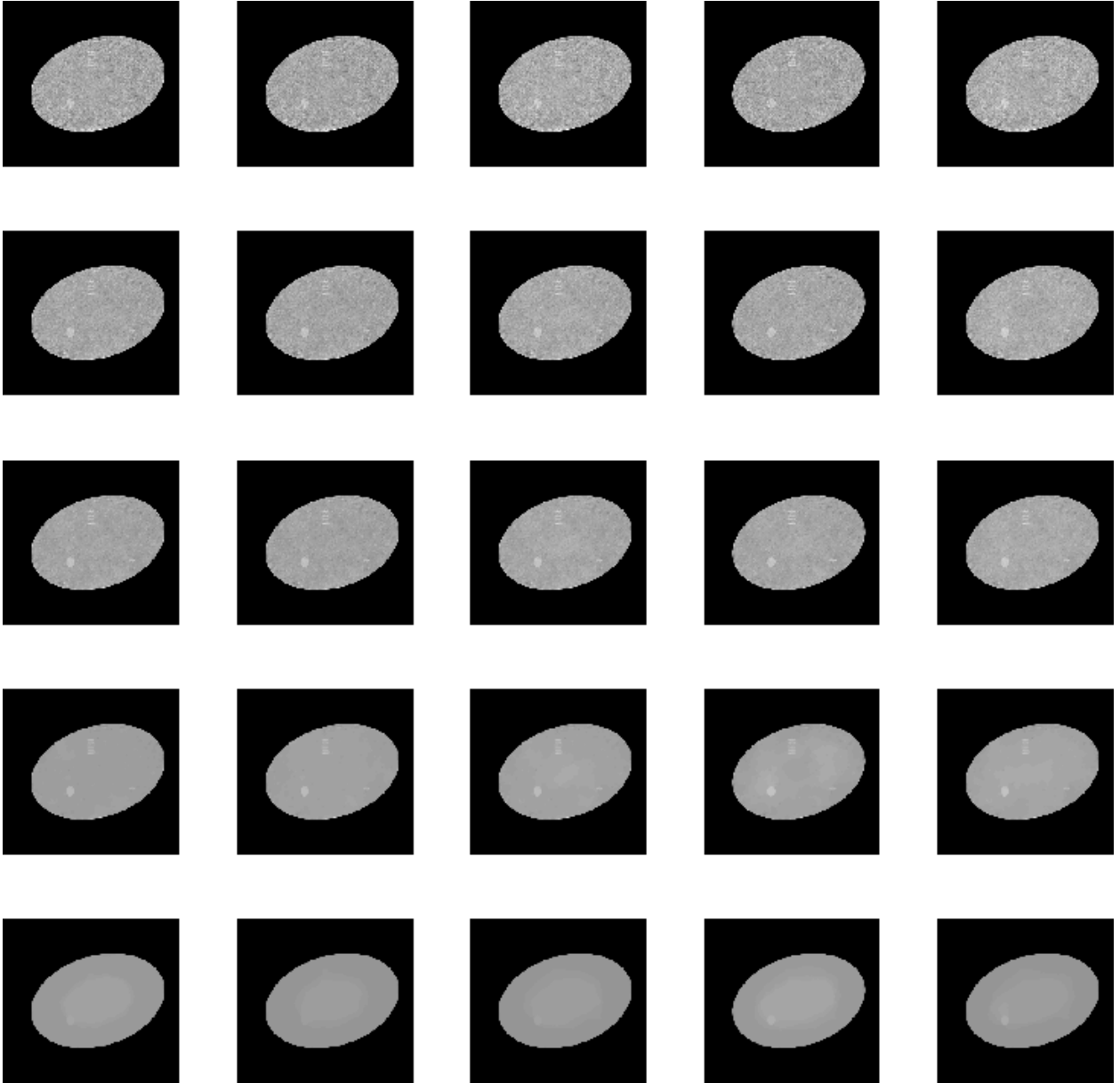
Figure 5.9: The reconstructed $\boldsymbol{\delta}$ image of the analytical geometric phantom for the AAP (2π) design with the different regularization parameters specified in Table 5.1. From left to right, the regularization parameter for $\boldsymbol{\beta}$ is increasing. From top to bottom, the regularization parameter for $\boldsymbol{\delta}$ is increasing.

Figure 5.10: The bar region of the reconstructed $\boldsymbol{\beta}$ image of the analytical geometric phantom for the AAP (2π) design with the different regularization parameters specified in Table 5.1. From left to right, the regularization parameter for $\boldsymbol{\beta}$ is increasing. From top to bottom, the regularization parameter for $\boldsymbol{\delta}$ is increasing.

Figure 5.11: The bar region of the reconstructed $\boldsymbol{\delta}$ image of the analytical geometric phantom for the AAP (2π) design with the different regularization parameters specified in Table 5.1. From left to right, the regularization parameter for $\boldsymbol{\beta}$ is increasing. From top to bottom, the regularization parameter for $\boldsymbol{\delta}$ is increasing.

The reconstructed images are intuitively consistent, in that higher regularization reduces noise, but setting the parameter too high can blur fine structures and reduce contrast. Moreover, the visual quality of the reconstructed absorption is mainly affected by the TV regularization parameter for $\boldsymbol{\beta}$, and that of the reconstructed refractive index decrement is mainly affected by the TV regularization parameter for $\boldsymbol{\delta}$. As a result, the parameters can be tuned separately.

Regularization parameters were chosen as a best compromise among their noise suppression effect, resolution, and contrast: $\alpha_1 = 1 \times 10^6$ for $\boldsymbol{\beta}$ and $\alpha_2 = 1000$ for $\boldsymbol{\delta}$. The same procedure was repeated for the CAP(2π) and AAP(1π) data-acquisition designs, and the same set of regularization parameters were determined to be optimal for CAP(2π). The optimal parameters for AAP(1π) are $\alpha_1 = 5 \times 10^5$ for $\boldsymbol{\beta}$ and $\alpha_2 = 500$ for $\boldsymbol{\delta}$.

5.4.2   Comparing data-acquisition designs based on image quality

The reconstructed images obtained by the identified regularization parameters in each candidate design were employed to compare the data-acquisition designs. A zoomed-in view of the bar region is given in Figure 5.14, and that for the circle region is given in Figure 5.16.

Judging from the visual appearance of the bar and circle regions, all of the designs resulted in images that revealed the bars and the circle clearly, with the reconstructed $\boldsymbol{\delta}$ image corresponding to the AAP (1π) design having a higher level of noise than other two designs. The MSE of the reconstructed images, as summarized in Table 5.2, also supports this finding. In addition, the shape of the boundary of the bar region is more distorted, indicating poorer reconstruction quality.

To better analyze the resolution, the profiles of the bar region along the vertical direction were averaged to produce the averaged profile shown in Figure 5.15. The averaging operation
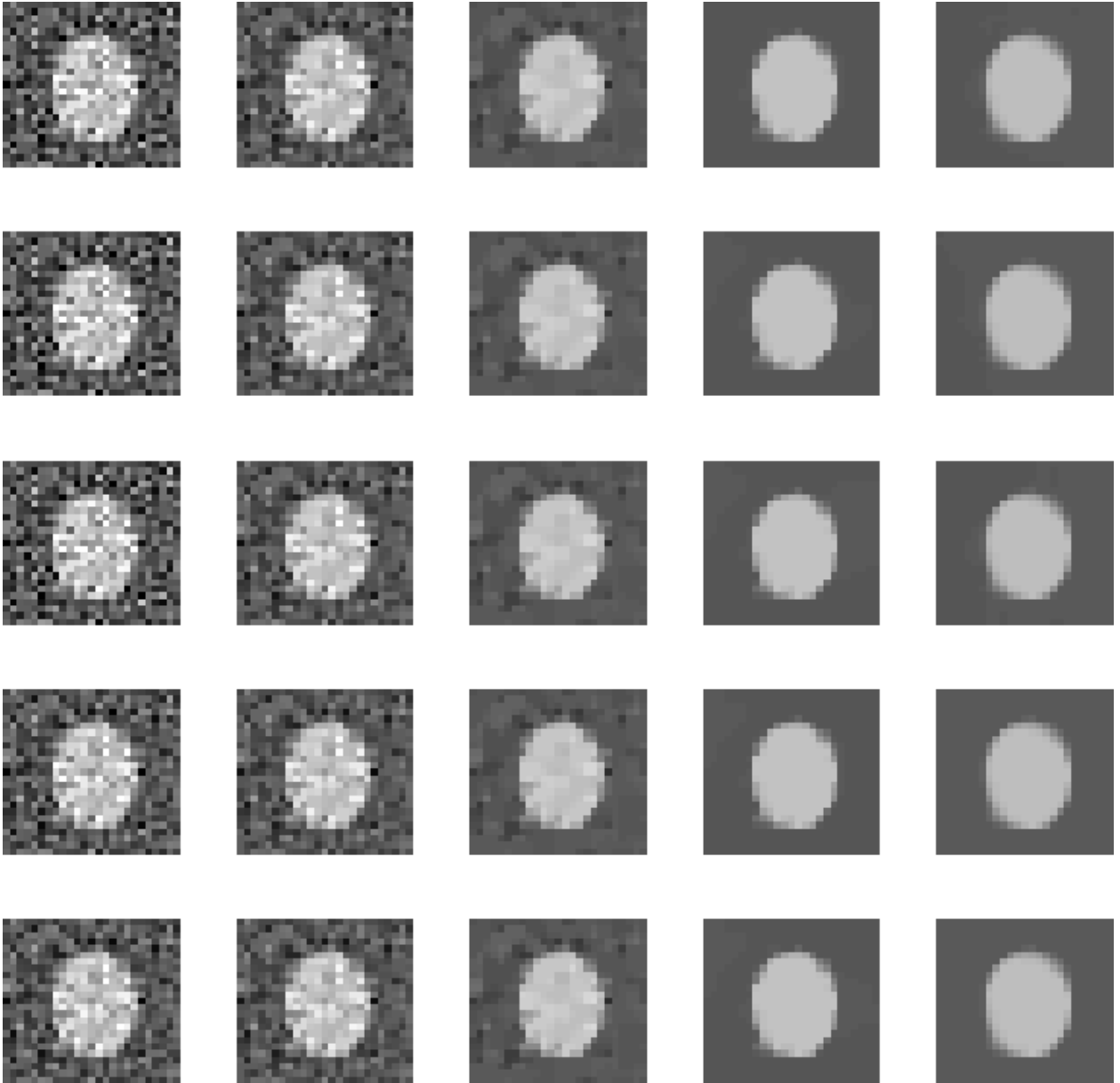
Figure 5.12: The circle region of the reconstructed $\boldsymbol{\beta}$ image of the analytical geometric phantom for the AAP (2π) design with the different regularization parameters specified in Table 5.1. From left to right, the regularization parameter for $\boldsymbol{\beta}$ is increasing. From top to bottom, the regularization parameter for $\boldsymbol{\delta}$ is increasing.
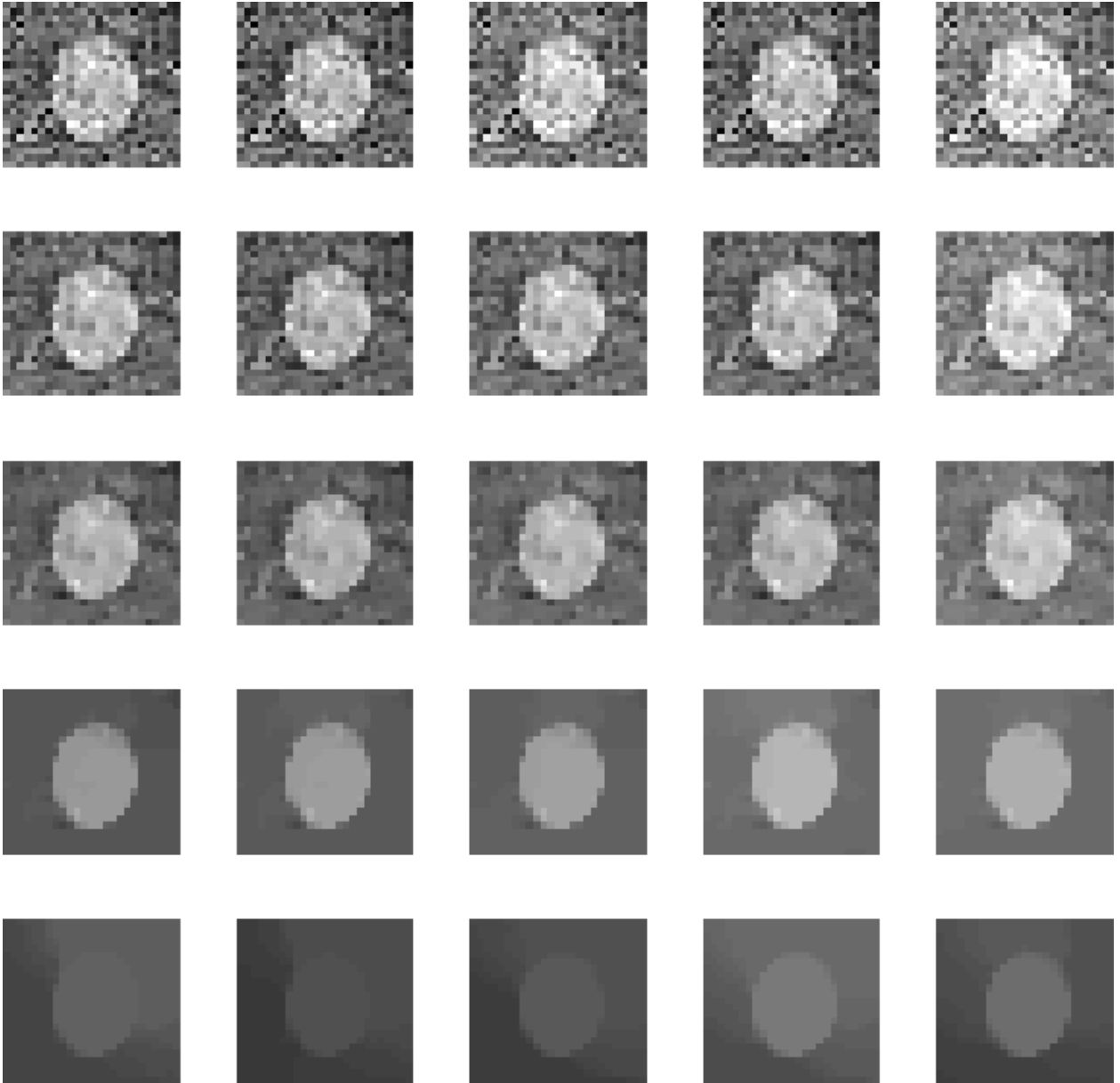
Figure 5.13: The circle region of the reconstructed $\boldsymbol{\delta}$ image of the analytical geometric phantom for the AAP (2π) design with the different regularization parameters specified in Table 5.1. From left to right, the regularization parameter for $\boldsymbol{\beta}$ is increasing. From top to bottom, the regularization parameter for $\boldsymbol{\delta}$ is increasing.
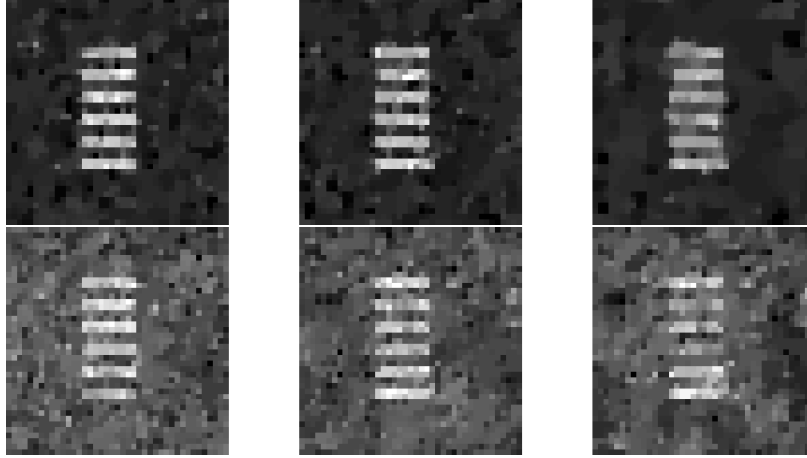
Figure 5.14: The bar region of the reconstructed absorption distribution (top) and refractive index decrement distribution (bottom) of the analytical geometric phantom for the CAP (2π), AAP (2π), and AAP (1π) designs (from left to right), with an optimal regularization parameter.

Table 5.2: MSEs for reconstructed images with the optimal regularization parameters

Distribution	CAP(2π)	AAP(2π)	AAP(1π)
β	9.86×10^{-10}	9.90×10^{-10}	1.49×10^{-9}
δ	4.82×10^{-6}	4.77×10^{-6}	6.08×10^{-6}

minimizes the effect of noise on the analysis of resolution. According to the profiles, the resolutions obtained by all three candidate designs are similar.

In summary, the image obtained by the AAP (1π) design shows slightly inferior noise statistics in terms of resistance to measurement data noise, but its resolution is mainly unaffected by the data-acquisition designs.
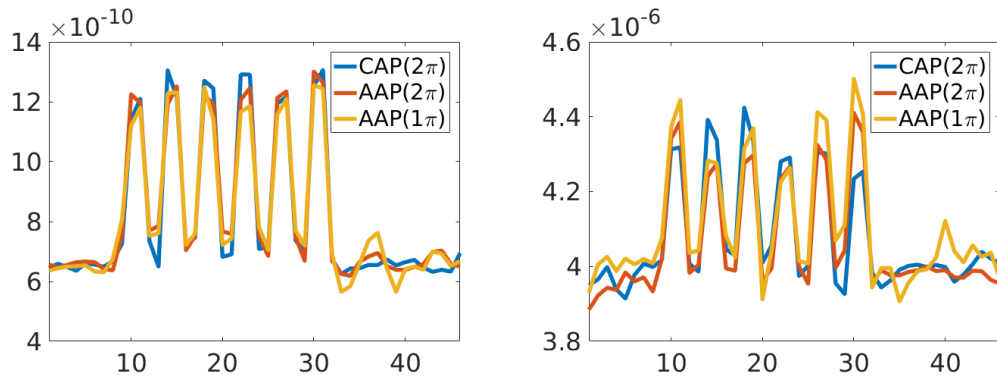
Figure 5.15: The averaged profile of the bar region of the reconstructed absorption distribution (left) and refractive index decrement distribution (right) of the analytical geometric phantom for the CAP (2π), AAP (2π), and AAP (1π) designs, with an optimal regularization parameter.
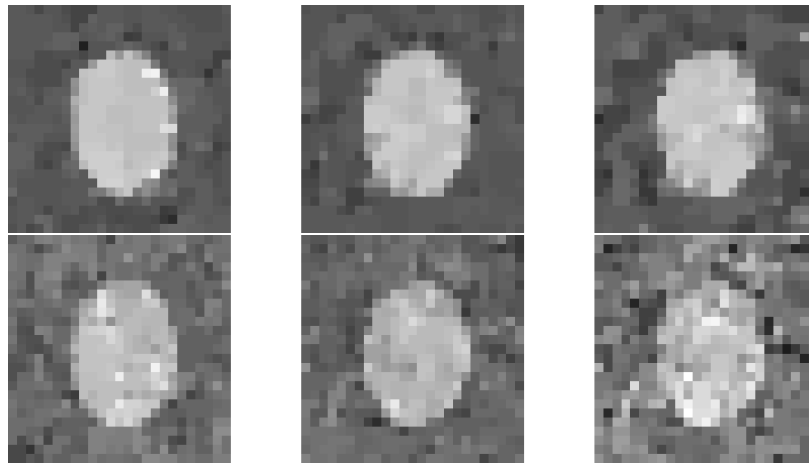
Figure 5.16: The circle region of the reconstructed absorption distribution (top) and refractive index decrement distribution (bottom) of the analytical geometric phantom for the CAP (2π), AAP (2π), and AAP (1π) designs (from left to right), with an optimal regularization parameter.

5.5   Experimental verification

The JR method was applied to the experimentally acquired data and the reconstructed images are shown in Figure 5.17. Consistent with the simulation studies, the AAP (1π) design was more affected by noise, but the structure shapes can all be reliably reconstructed, which is clearly demonstrated especially by the fine details in the paraffin film region.

Note that there are dark artifacts in the center of the reconstructed refractive index decrement image corresponding to the CAP (2π) data-acquisition design, which are possibly due to the non-uniformity of the illumination curves across the whole field of view. Techniques such as local phase retrieval [61] may alleviate these artifacts. In comparison, the AAP designs benefit from the diversity in their data that is caused by frequent movement of the sample mask, and thus are less affected by the model mismatch problem in practice.
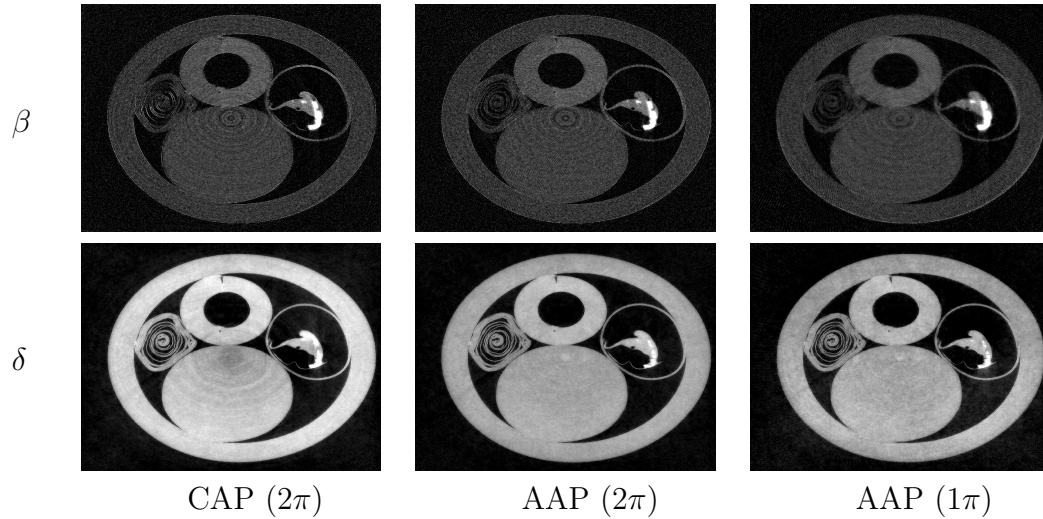
Figure 5.17: The reconstructed absorption (first row) and refractive index decrement (second row) distributions using three data-acquisition designs.

5.6 Conclusion

This work investigated a series of flexible data-acquisition designs for EIXPCT enabled by a JR method. The designs differ in terms of their data-acquisition simplicity and reconstruction stability and quality. The data-acquisition simplicity mainly refers to whether the mask position needs to be moved. Three representative designs were selected for the low artifact level of their reconstructed images from an idealized noise-free simulated measurement dataset. The three designs were further investigated for cross-talk, reconstructed image noise level, resolution, and ultimately tested on real experimental data. Table 5.3 summarizes the data-acquisition properties of the three single-shot methods.

Different data-acquisition designs have different advantages. The CAP(2π) design has the simplest data-acquisition procedure because the masks do not need to be moved, but it may be more affected by model mismatch in practice. The AAP(2π) design demonstrated the highest fidelity reconstructed images and is less affected by the model mismatch problem. However, it requires extra mask movement and therefore makes the data-acquisition process

79

	CAP (2π)	AAP (2π)	AAP (1π)	CVN (2π)	CVN (1π)
Minimum angular range	2π	2π	1π	2π	1π
Change mask position	No	Yes	Yes	Yes	Yes
Image obtained per view	1	1	1	2	2
Number of acquired images	2V	2V	V	4V	2V
Model matchness	Poor	Good	Good	Good	Good
Cross-talk effect by JR	Weak	Weak	Medium	/	/
Noise level by JR	Good	Good	Poor	/	/
Resolution by JR	Good	Good	Good	/	/

Table 5.3: A comparison of the five methods (in the table, V is the number of views obtained for π angular range)

more complex. The AAP(1π) design requires the minimum amount of images due to its small angular coverage range and single-shot design. However, images reconstructed from data acquired by the AAP(1π) design can be susceptible to noise amplification. Ultimately, the selection of a data-acquisition design should be optimized based on the specific needs of the application.

Chapter 6

A Partial-Dithering Strategy for Edge-Illumination X-Ray Phase-Contrast Tomography Inspired by Joint Reconstruction Algorithm

6.1 Introduction

The spatial resolution of the reconstructed EIXPCT images is influenced by several experimental factors that include the detector pitch and the mask periods. If a higher resolution is desired, upgrading the detector and the masks is the most straight-forward solution, but also the most expensive. However, spatial resolution can also be improved by employing a data-acquisition strategy called dithering [20, 21], without changing the detector or the masks. In this strategy, multiple images corresponding to different sub-pixel-translated object

81

positions are acquired at a given tomographic view angle. These images can be stitched together to form a single high-resolution image that estimates one that would have been measured with a higher-resolution system. Ultimately, the reconstructed β and δ images will have enhanced spatial resolution as well.

Although the dithering technique boosts the spatial resolution of the reconstructed images, implementing dithering is time-consuming and thus hinders *in vivo* or radiation sensitive applications. In this study, motivated by the flexibility in data-acquisition designs enabled by a recently developed joint reconstruction (JR) method [9], a novel partial-dithering strategy is proposed. The core idea of partial-dithering is to implement dithering at only a subset of the tomographic view angles while obtaining no-dithering measurements at the rest of the view angles. The technique achieves a balance between image quality and data-acquisition time, improving image resolution over the no-dithering strategy and reducing the data-acquisition time over the full-dithering strategy.

6.2 Background

6.2.1 Forward imaging model considering dithering

As described in Chapter 2, in EIXPCT imaging [36, 39, 42], phase information is obtained by employing a sample mask (or sample aperture), A_1, and a detector mask (or detector aperture), A_2, both of which are shown in Figure 6.1(a). The object is placed immediately after A_1. When the relative positions of the two parallel masks are changed, different portions of the incident X-ray beam fall onto the sensitive areas of the detectors. Thus, the differential phase information is encoded in the X-ray wave intensity. EIXPCT imaging measures the wave intensity, from which the absorption and refractive index decrement distributions can

both be estimated. The distance from the source to A_1 is denoted as l_{so}, and the distance between A_1 and A_2 is denoted as l_{od}. A_1 can be translated to achieve optimal phase contrast detectability. The displacement of the two masks after the translation is denoted by $\Delta\xi$. The imaged object can also be translated in the direction parallel to the masks over a distance of Δy. This movement is mainly used in the dithering step to be described in Sec.6.2.3, so Δy is referred to as the dithering offset.

Let $A(\theta, y) \in \mathbb{L}_2(\mathbb{R}^2)$ (or $\phi(\theta, y) \in \mathbb{L}_2(\mathbb{R}^2)$) denote he line integral of the continuous distribution β (or δ) along a beam trajectory, which is specified by the tomographic view angle θ and the detector location y:

$$A(\theta, y) = \int_{\theta, y} \beta(x, y) dl, \tag{6.1}$$

$$\phi(\theta, y) = \int_{\theta, y} \delta(x, y) dl. \tag{6.2}$$

Also, let $\phi_d(\theta, y) \in \mathbb{L}_2(\mathbb{R}^2)$ denotes the first order derivative of $\phi(\theta, y)$ with respect to y:

$$\phi_d(\theta, y) = \frac{\partial}{\partial y} \phi(\theta, y). \tag{6.3}$$

The imaging process can thus be approximately described as [9, 36]:

$$I(\theta, y_r, \Delta\xi, \Delta y) = \exp\left[-\frac{2\pi}{\lambda} A(\theta, y_r + \Delta y)\right] \tag{6.4}$$
$$\times \left[I_{TC}(\Delta\xi) - \frac{l_{od} l_{so}}{l_{so} + l_{od}} I'_{TC}(\Delta\xi) \phi_d(\theta, y_r + \Delta y)\right],$$

where $I(\theta, y_r, \Delta\xi, \Delta y)$ is the normalized measured intensity at the tomographic view angle θ, detector location y_r, mask-displacement $\Delta\xi$, and the object dithering offset Δy. The wavelength of the monochromatic incident beam is denoted by λ. A measurement vector can be obtained by concatenating all measured data points.
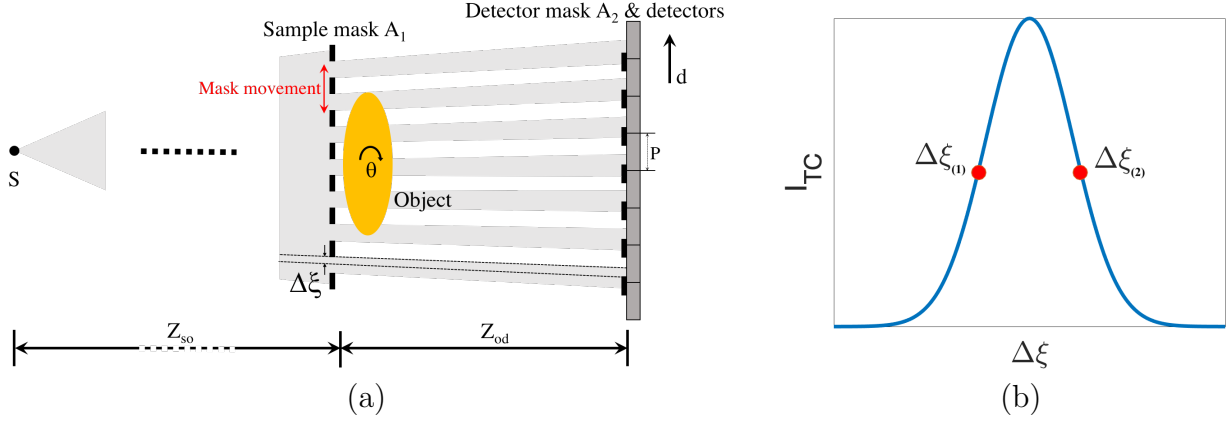
Figure 6.1: (a) Illustration of the EIXPCT system. (b) A typical illumination curve. The exposures are usually acquired at the two marked locations corresponding to half-maximum illumination level.

The imaging model given in Equation (6.4) is discretized for formulating the reconstruction problem as a finite-dimensional optimization problem. Let $\boldsymbol{\beta} \in \mathbb{R}^N$ denote the discretized absorption distribution where the elements in the vector are sampled values of absorption distribution at N vertices. Similarly, $\boldsymbol{\delta} \in \mathbb{R}^N$ denotes the discretized refractive index decrement distribution. The line integral of the continuous distribution β (or δ) along a beam trajectory is thus approximated by a weighted sum of all the elements in the discretized vector $\boldsymbol{\beta}$ (or $\boldsymbol{\delta}$). In other words, the Equation (6.1) and Equation (6.2) are rewritten as

$$A(\theta, y) = \sum_{i=1}^{N} \boldsymbol{h}_i(\theta, y) \boldsymbol{\beta}_i, \tag{6.5}$$

and

$$\phi(\theta, y) = \sum_{i=1}^{N} \boldsymbol{h}_i(\theta, y) \boldsymbol{\delta}_i, \tag{6.6}$$

where $\boldsymbol{h}_i(\theta, y)$ denotes the length of the intersection between the pixel corresponding to the i-th element in $\boldsymbol{\beta}$ (or $\boldsymbol{\delta}$) and the X-ray beam, which is specified by the tomographic view angle θ and the detector location y.

84

During the data-acquisition process, the view angle θ, detector location y_r, mask-displacement $\Delta\xi$, and the object dithering offset Δy can all be varied. For each X-ray exposure, the view angle θ, mask-displacement $\Delta\xi$ and dithering offset Δy are all fixed. The R different detector elements in the detector collect measurement data at R different detector locations, y_{rj} ($j = 1, 2, ..., R$). A typical tomographic dataset acquires images at V different view angles θ_i ($i \in \{1, 2, ..., V\}$), equally distributed over a 2π scanning angular range. The data-acquisition design for a tomographic scan includes two parts: picking the number of exposures at each view angle and selecting $\Delta\xi$ and Δy at each exposure. The selections of $\Delta\xi$ and Δy are independent.

6.2.2 Mask-displacement selection strategy and joint reconstruction method

The illumination curve informs selection of the mask-displacement, $\Delta\xi$. Figure 6.1(b) shows a typical illumination curve, I_{TC}, as introduced in Equation (6.4). Given Equation (6.4), the most efficient way to maximize the δ-signal contrast in the measured intensity signals is to adjust the mask to a special location where the derivative of the illumination curve is the largest. There are two locations satisfying this condition: the two half-maximum locations, $\Delta\xi_{(1)}$ and $\Delta\xi_{(2)}$, as shown in Figure 6.1(b).

A mask-displacement strategy selects one of these two locations. The selection of $\Delta\xi$ is closely related to the reconstruction method employed. The measurement data should be acquired so that the reconstruction algorithm is capable of accurately and stably estimating for the absorption and refractive index decrement distributions. The conventional reconstruction method employs a two-step approach [36] – a phase-retrieval step followed by a

tomographic reconstruction step. It requires taking exposures at both mask-displacements at each tomographic view angle.

The joint JR method described in Chapter 3 combines the phase-retrieval step with the tomographic reconstruction step and can enable different mask-displacement strategies. The JR method seeks to estimate the $\boldsymbol{\beta}$ and $\boldsymbol{\delta}$ distributions of the object by minimizing the summation of the least squares error and a penalty term as shown in Equation (3.8) [9]. It has been proven that the JR method requires taking exposures at only one mask-displacement at each view angle. Also, selecting which mask-displacement to use at each view angle can be flexible, and the selection strategy has been extensively discussed in previous works [8, 9].

In this chapter, the focus is on the dithering strategies for selecting Δy. One typical data-acquisition design is investigated as an example – the alternating aperture position plan covering an angular range of 2π (abbreviated as the AAP (2π) plan) as introduced in Chapter 6 [8]. With this design, the object is imaged at V tomographic view angles uniformly distributed over the 2π range: $\theta_i = 2\pi(i-1)/N$ $(i = 1, 2, ..., V)$. At each tomographic view angle θ_i, one mask-displacement, $\Delta\xi_i$, is selected from two optimal locations that correspond to maximum absolute gradients of the illumination curve. The displacement is $\Delta\xi_{(1)}$ for odd views, and $\Delta\xi_{(2)}$ for even views. The following discussion assumes the AAP (2π) design is employed.

6.2.3 Dithering technique

Dithering is the process of moving the object over sub-pixel distances and obtaining multiple images to artificially increase resolution [21]. Dithering can be incorporated in any data-acquisition design using a specific mask-displacement selection strategy. If K-step dithering is employed, K times as many exposures are obtained compared to the no-dithering situation.

In a K-step dithering strategy, K images are acquired at dithering offsets

$$\Delta y_k = \frac{k-1}{K} \frac{l_{so}}{l_{so} + l_{od}} P, (k = 1, 2, ..., K). \tag{6.7}$$

The K images are later stitched together to form a higher resolution measured image. If tomography is performed, a high resolution reconstructed images can be obtained from the resolution-enhanced measurement data, but at the cost of $K-1$ extra exposures per tomographic view angle.

6.3 Methods

A novel dithering strategy for EIXPCT called partial-dithering is proposed. For clarity of notation, the conventional dithering technique will be called full-dithering.

6.3.1 No-dithering, full-dithering, and partial-dithering

When there is no dithering employed, one exposure is acquired at each tomographic view angle: R detector elements collect R measured intensities at locations y_{rj} $(j = 1, 2, ..., R)$ with $\Delta y = 0$. The intensities $I(\theta_i, y_{rj}, \Delta \xi_i, \Delta y = 0)$ are measured for $i \in \{1, 2, ..., V\}$ and $j \in \{1, 2, ..., R\}$.

When K-step full-dithering is employed, at every view angle, K images are acquired, corresponding to $\Delta y = (k-1)P/K$ $(k = 1, 2, ..., K)$, where P is the period of the sample mask, A_1. In this situation, $I(\theta_i, y_{rj}, \Delta \xi_i, \Delta y_k)$ is measured for $i \in \{1, 2, ..., V\}$, $j \in \{1, 2, ..., R\}$, and $k \in \{1, 2, ..., K\}$.

In the novel partial-dithering strategy proposed in this work, instead of implementing dithering at every view angle, dithered measurement data are acquired only at every D views, and

Figure 6.2: A comparison between no-dithering, full-dithering and partial-dithering when $V = 6$ and $D = 3$. Each arc represents a tomographic view angle. The numbers on the arcs orange arcs denote the number of exposures taken at the view angle. The orange arc means K-step dithering is implemented at the view angle, while a blue arc means there is only 1 exposure taken.

thus there are V/D dithering views as well as $V - V/D$ non-dithered views. D is defined as the dithering interval. To simplify the discussion, V/D is assumed to be an integer in this work. The dithered view set is defined as $S_d = \{1, D+1, 2D+1, ..., V-D+1\}$, and the complementary non-dithered view set is defined as $S_n = \{1, 2, ..., V\} \setminus S_d$. Consequently, $I(\theta_i, y_{rj}, \Delta\xi_i, 0)$ is measured for $i \in S_n$, $j = 1, 2, ..., R$, and $I(\theta_i, y_{rj}, \Delta\xi_i, \Delta y_k)$ is measured for $i \in S_d$, $j \in \{1, 2, ..., R\}$, and $k \in \{1, 2, ..., K\}$. Figure 6.2 illustrates no-dithering, full-dithering, and partial-dithering. For an object with an absorption distribution $\boldsymbol{\beta}$ and refractive index decrement distribution $\boldsymbol{\delta}$, concatenating the simulated measured intensities from all dithering views yields the simulated dithered measurement vector, $\mathbf{I}_d(\boldsymbol{\beta}, \boldsymbol{\delta})$, and concatenating those from non-dithering views yields the simulated non-dithered measurement vector, $\mathbf{I}_n(\boldsymbol{\beta}, \boldsymbol{\delta})$. The total data-acquisition time is proportional to the number of exposures required during the data-acquisition process. For each combination of θ_i and Δy_k, one exposure is required. Thus the total number of required exposures is equal to the total number of $(\theta_i, \Delta y_k)$ combinations, which is $V + (V/D) \cdot (K - 1)$. Figure 6.3 depicts the
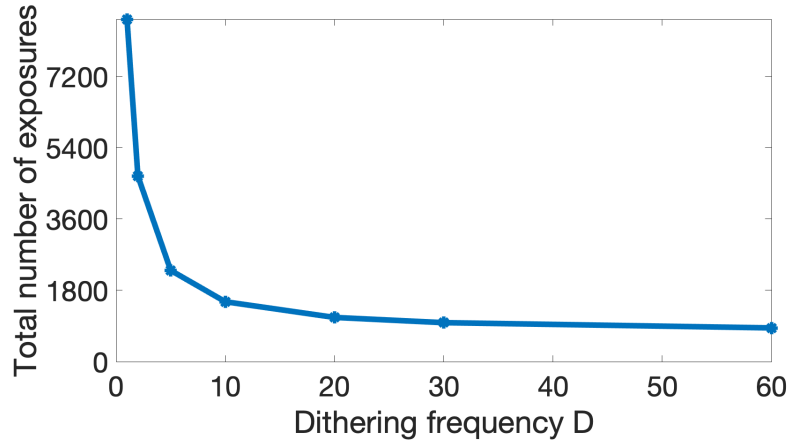
Figure 6.3: A demonstration of the time-saving effect of the partial-dithering strategy. It shows the total number of X-ray exposures for 12-step partial-dithering acquisition with 720 view angles as a function of dithering frequency D, which is a typical setup in experiments. The marked data points correspond to $D = 1, 2, 5, 10, 20, 30$, and 60. The number of exposures is proportional to the data-acquisition time. Merely increasing D from 1 to 2 can reduce the required number of exposures from 8640 to 4680, with a corresponding 46% reduction in the data-acquisition time.

number of exposures required for various dithering intervals. Merely increasing D from 1 to 2 can almost reduce the data-acquisition time by one-half.

6.3.2 Image reconstruction from partial-dithered measurement data

Conventional analytic two-step reconstruction methods for EIXPCT [36] are suboptimal for use with acquired images whose spatial resolution varies with view angle, such as produced with the partial-dithering strategy. To circumvent this, a modified version of the JR method is employed to reconstruct image estimates from measured intensity data that are dithered at only a subset of view angles. A modified cost function is defined as a weighted least squares data fidelity term with a total variation (TV) penalty term:

$$f = \alpha_n \|\mathbf{I}_{m,n} - \mathbf{I}_n(\boldsymbol{\beta}, \boldsymbol{\delta})\|^2 + \alpha_d \|\mathbf{I}_{m,d} - \mathbf{I}_d(\boldsymbol{\beta}, \boldsymbol{\delta})\|^2 + R(\boldsymbol{\beta}, \boldsymbol{\delta}), \quad (6.8)$$

89

where $\mathbf{I}_{m,n}$ and $\mathbf{I}_{m,d}$ denote the experimentally acquired measured intensities in all non-dithering and dithering views, respectively, and $R(\boldsymbol{\beta}, \boldsymbol{\delta})$ is the weighted TV penalty of $\boldsymbol{\beta}$ and $\boldsymbol{\delta}$. Here, α_n and α_d are the weights of non-dithering and dithering views in the data fidelity term.

The weights α_n and α_d can be tuned to achieve the desired reconstructed image quality. In general, increasing α_n puts more emphasis on the contribution from non-dithered measurement data; this approach yields faster solution convergence but lower image resolution. On the contrary, increasing α_d is expected to improve image quality, but has the disadvantage of slower algorithm convergence. To combine the merits of both approaches, two-phase iterative reconstruction is proposed. In the first phase, the value of α_n is high but the value of α_d is low, so a low-resolution converged solution can be obtained quickly, and the result can serve as the initial guess for the second phase. In the second phase, the value of α_n is low but the value of α_d is high, so the details can be better refined. The exact values of α_n and α_d are tuned empirically.

6.3.3   Simulation studies

The 2-dimensional (2D) geometric phantom shown in Figure 6.4 was employed in the computer-simulation studies. The elements within the phantom include a small ellipse, a bar, and a triangle region. The phantom assumes adipose tissue as the material for the big ellipse and soft tissue as that for the small ellipse, the bar, and the triangles [22]. The triangle region at the top is designed for analysis of resolution. All 6 of the small triangles have the same base 200 μm length and 4 mm height. The bases of all the small triangles are aligned vertically, and the distance between the bases of neighboring triangles is also 200 μm. A vertical line, denoted as a scan line, can be moved from the left to the right in the triangle region. The profile extracted from the scan line contains periodic patterns similar to that in Figure 6.7(a),

90
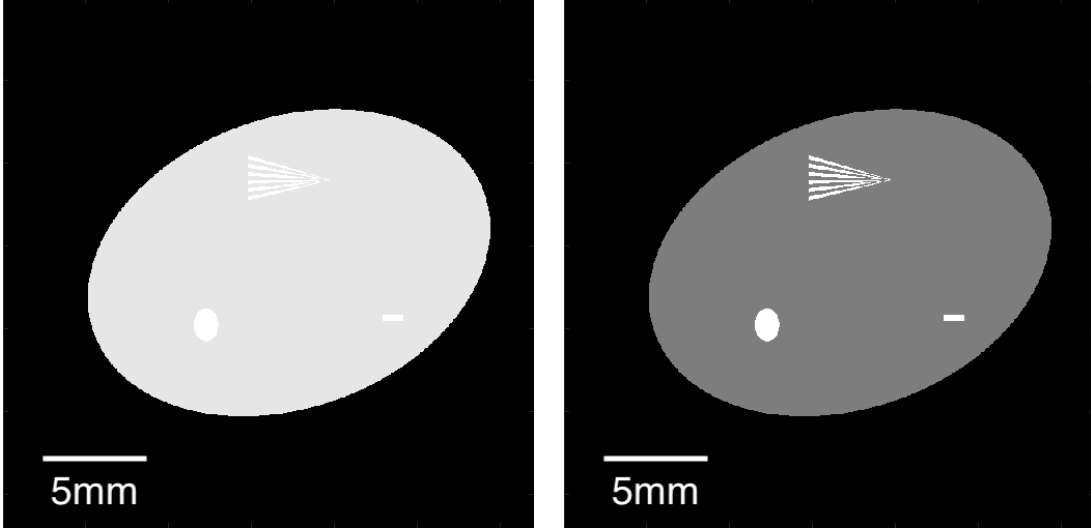
Figure 6.4: The refractive index decrement distribution phantom (left) and the absorption distribution phantom (right).

as if the profile is obtained for periodic bars. When the profiles are obtained at different horizontal locations, the bar width/gap will change from 200 μm to 0 μm. In order to analyze the system's resolution, the scan line is moved from left to right until the extracted profile is no longer capable of resolving the periodic patterns. In this way, the triangle pattern can provide insights about the resolution of the reconstructed images.

A monochromatic X-ray parallel beam of 5.17×10^{-11} m wavelength (i.e., 24 keV) was assumed to irradiate the object. The two masks were positioned so that $l_{so} = 1.6$ m and $l_{od} = 0.4$ m. Simulated measurement data were obtained from 720 tomographic views that were evenly distributed over 360 degrees. The detector contained a row of 400 pixels with a pixel size of 100 μm. Five-step dithering was implemented every D views. Dithering was performed with $\Delta y = 20$ μm. Several different dithering intervals were tested: $D = 1, 2, 5, 10, 20, 30,$ and 60, with $D = 1$ representing the full-dithering situation. A no-dithering situation was also included for comparison. The measurement data were simulated based on Equation (6.4), with an analytical integration step in the Radon transformation and Poisson noise added.

The illumination curve was modeled after a previous experiment [36]. At the optimal mask-displacements, $\Delta\xi_1 = -8\,\mu$m and $\Delta\xi_2 = 8\,\mu$m, the values of I_{TC} and the corresponding gradient I'_{TC} can be read from the illumination curve as $I_{TC1} = I_{TC2} = 0.5$ a.u. (arbitrary unit), and $I'_{TC1} = 4 \times 10^4\,\mathrm{m}^{-1}$, $I'_{TC2} = -4 \times 10^4\,\mathrm{m}^{-1}$. The phantom was reconstructed with a $2\,\mu$m pixel size. During the two-phase reconstruction, $\alpha_n = 1, \alpha_d = 0$ were selected for the first phase, and $\alpha_n = 0.1, \alpha_d = 1$ were selected for the second phase. To make sure the reconstructions at different dithering intervals received similar levels of TV regularization, the weight for the TV penalty was chosen to be proportional to the total number of measured data points. The fast iterative shrinkage-thresholding algorithm (FISTA) [9] was employed to minimize the cost defined in Equation (6.8). The iteration loop stops when the cost is below a certain threshold selected by trial and error.

6.3.4 Experimental validation

Experimental data acquired in a previous study [14] were employed to validate the feasibility of the proposed data-acquisition designs. The imaged object was a custom-built phantom consisting of a hollow plastic cylinder, a plastic rod, a smaller hollow plastic cylinder, rolled plastic paraffin film, and chalk inside a plastic container. Additional details of the imaging system and parameters can be found in the literature [14]. The rolled plastic paraffin film region contains many detailed structures, so those are the focus of our resolution analysis. In the partial-dithering strategy, several different D values were tested: $1, 2, 5, 10, 20, 30$, and 60. At the dithering views, a ten-step sub-pixel dithering ($K = 10$) of the imaged object was employed. During the two-phase reconstruction, α_n and α_d were set as 1 for the first phase, and $\alpha_n = 0, \alpha_d = 1$ were selected for the second phase. The weight for the TV penalty was also chosen to be proportional to the total number of measured data points. The pixel size of the reconstructed images was 8.8 μm.

6.4 Results

6.4.1 Computer-simulation studies

The triangle regions of the reconstructed estimates of $\boldsymbol{\delta}$ with different dithering intervals are shown in Figure 6.5. The boundaries of the triangles become clearer with increasing numbers of dithering views. The gaps between neighboring triangles shrink from left to right. When the number of dithering views increases, smaller gaps begin to be differentiated. The differentiation can be better shown in Figure 6.6, where the reconstructed profiles and the ground truth profiles are compared at different dithering intervals. The profiles are obtained from the same vertical scan line, along which the neighboring triangles have a gap of 80 μm. At this location, only the reconstructed profiles of D=1 and D=2 can unambiguously show the differentiation. The others are unable to reveal the pattern details.
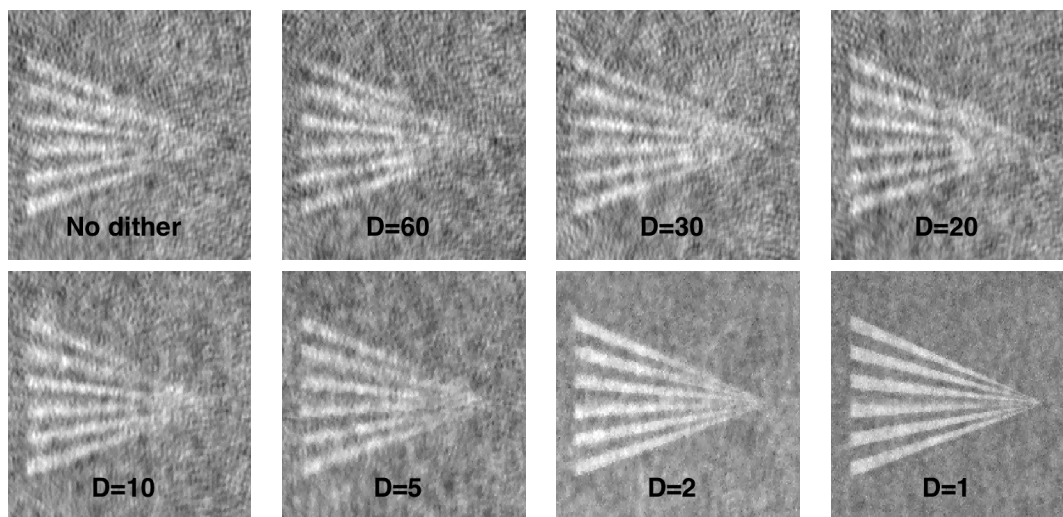
Figure 6.5: The triangle regions of the reconstructed refractive index decrement distributions when the interval of dithering changes. When dithering is implemented more frequently, it is easier to differentiate the triangles, indicating that the resolution increases.
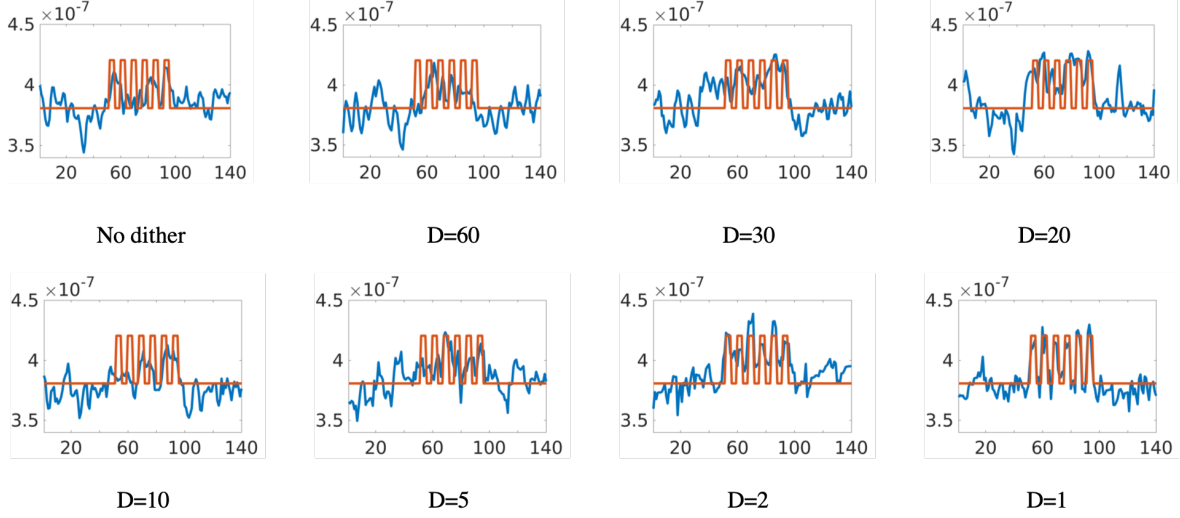
Figure 6.6: The profiles of the actual refractive index decrement distribution (red) and reconstructed refractive index decrement distribution (blue) along one vertical line in the triangle region when the interval of dithering changes. The gaps between the different triangles at this profile are all the same – 80μm. The different structures are most clearly separated when the dithering interval is 1 or 2.

For a more quantitative analysis, we introduced the peak-gap-ratio (PGR). For each profile extracted at one particular vertical scan line in the triangle region of the reconstructed image, the values of all the reconstructed pixels within the triangles, highlighted in red in Figure 6.7(a), were averaged and a peak value was obtained; then, the values of all the reconstructed pixels in the gap region between triangles, highlighted in blue in Figure 6.7(a), were averaged and a gap value was obtained. The ratio of the peak value to the gap value is defined as the PGR. When two peaks are separated clearly, the peak region is higher than the gap region so PGR is large. When two peaks are blurred out and undistinguishable, the peak and gap regions will share similar values so the PGR will be close to 1. In summary, a larger PGR indicates better differentiability.

A illustration of the PGR values as a function of dithering interval and gap size is shown in Figure 6.7(b), and a thresholded version is given in Figure 6.7(c). Figure 6.7(b) and
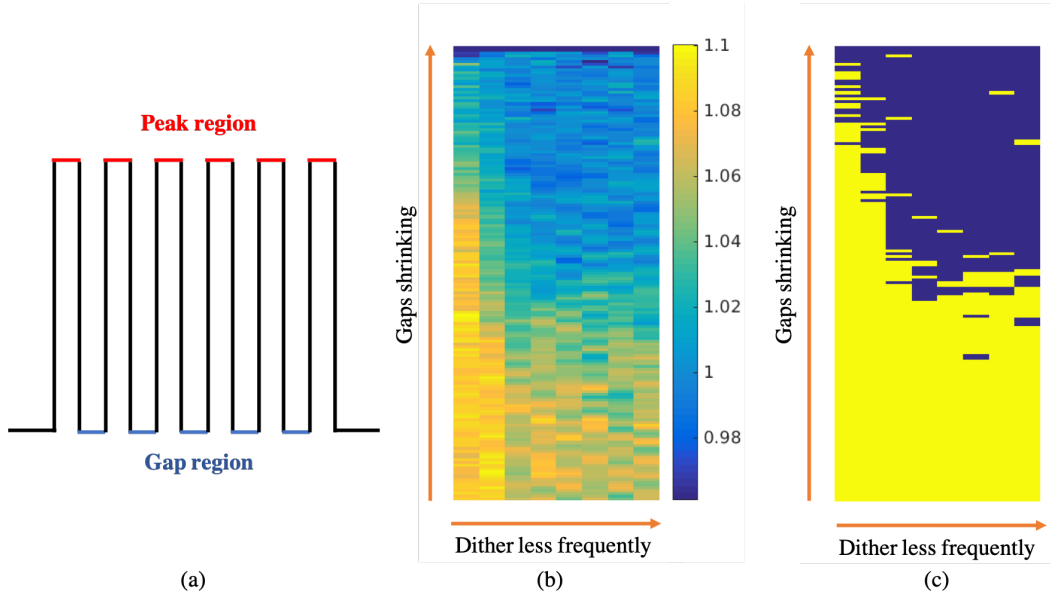
Figure 6.7: (a) Illustration of the peak region and the gap region. The entire line represents a typical line profile along one vertical line in the triangle region in the phantom. The red pixels represent the peak region and the blue pixels represent the gap region. (b) The PGRs calculated for the refractive index decrement distributions at different vertical lines, corresponding to different gaps between the triangle patterns. The horizontal direction corresponds to 8 different dithering intervals: 1, 2, 5, 10, 20, 30, 60, and no dither. For the same gap between triangle patterns, when dithering is implemented more frequently, the PGR is in general larger. (c) A thresholded PGR image. The yellow regions correspond to ratios larger than a pre-set threshold of 1.02.

Figure 6.7(c) both show that when dithering is more frequent, the PGR can maintain a relatively high value for a much smaller gap size, corroborating the conjecture that partial-dithering can help improve resolution.

6.4.2 Experimental validation

The rolled plastic paraffin film regions of the estimates of $\boldsymbol{\delta}$ reconstructed from the experimentally acquired data are shown in Figure 6.8. Zoomed-in views of a small region (the bottom left corner of the rolled plastic paraffin film region) are shown in Figure 6.9.

The separation of two closely located films, with a gap of approximately 12 μm, becomes clearer with more dithering views. The two films are clearly separated for $D \leq 5$. This trend indicates that better resolution can be obtained when D is smaller. Note that the artifacts in the no-dithering reconstructed image are related to the loss of reliability of the retrieved phase shift values caused by under-sampling [21]. Similar to the full-dithering strategy, partial-dithering also suppresses these artifacts by increasing the sampling rate at the dithered views.
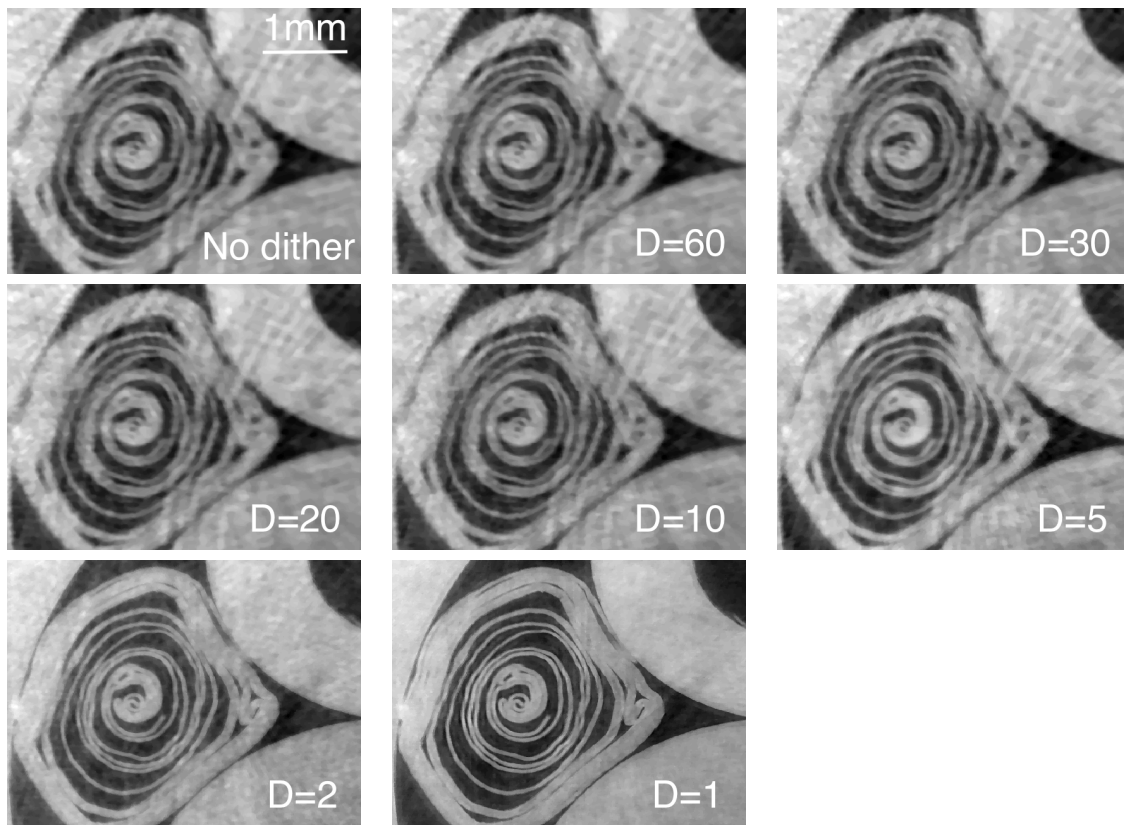
Figure 6.8: The rolled plastic paraffin film regions of the reconstructed refractive index decrement distributions when the interval of dithering changes. When the dithering interval is higher, the resolution improves and artifacts are diminished.
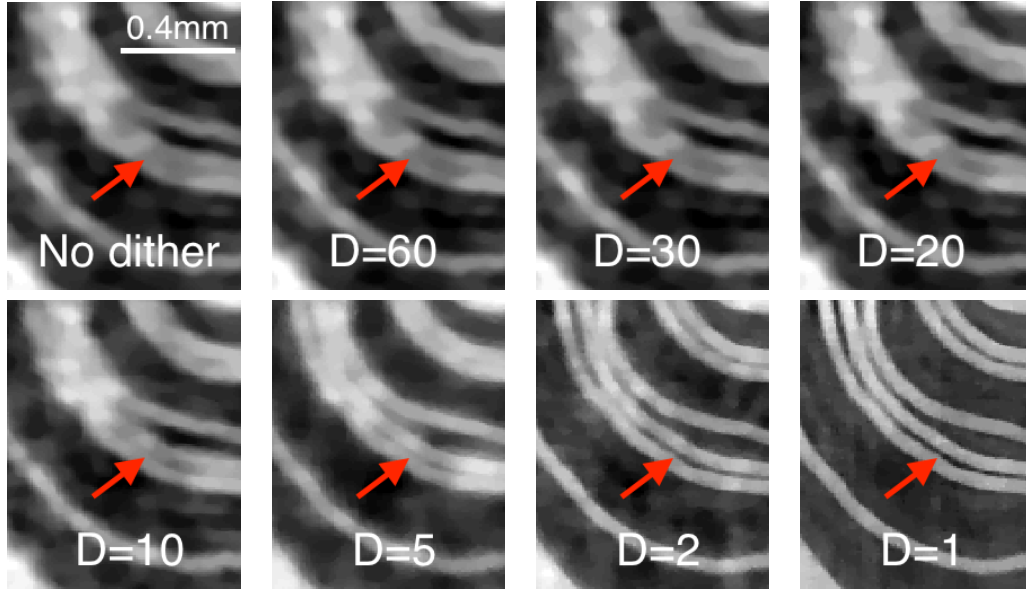
Figure 6.9: Zoomed-in views of the bottom left corner in the rolled plastic paraffin film region of the reconstructed refractive index decrement distributions when the interval of dithering changes. When the dithering interval is higher, the separation between two close films becomes clearer.

6.5 Conclusion

To enhance spatial resolution in EIXPCT, dithering can be employed. This technique moves the to-be-imaged object by a series of sub-pixel distances and acquires measurement data at the different dithering locations. The images acquired at each X-ray exposure are later synthesized into a higher-resolution image, from which an enhanced resolution reconstructed tomographic image can be computed. The main drawbacks of the dithering technique are prolonged data-acquisition times and increased radiation doses. In this article, a partial-dithering strategy was proposed for EIXPCT where dithering is applied periodically at a subset of tomographic view angles at which data were acquired. Compared with the conventional full-dithering technique, partial-dithering greatly reduces the data-acquisition

97

time, but improves spatial resolution over the no-dithering case. Partial-dithering can decrease data-acquisition time when high resolution is required in tomographic imaging.

Image reconstruction from partially-dithered measurement data was enabled by use of an iterative joint reconstruction (JR) method, which was implemented in two steps to improve reconstruction speed. The non-dithered views were weighted more heavily in the first JR phase so that a low-resolution converged solution can be quickly obtained. The dithered views were weighted more heavily in the second JR phase to maximize the spatial resolution improvement. It was demonstrated that, with partial-dithering, the image resolution was improved compared with no-dithering, and the data-acquisition time is shorter than that of full-dithering. Partial-dithering is a first exploration of novel dithering strategies, and, more flexible dithering strategies can be studied in the future. Moreover, the dithering strategy can also be combined with mask-displacement selection strategy [8]. Such creative designs could potentially provide better reconstructed image quality, with even shorter data-acquisition times.

Chapter 7

Edge-Illumination X-Ray Phase-Contrast Tomography Experimental Setup for *In Vivo* Small Animal Imaging

7.1 Challenges of *in vivo* small animal imaging

Previous bench-top EIXPCT imaging systems have required long data-acquisition times that have prevented routine *in vivo* imaging. No *in vivo* animal studies have been reported. This final component of research seeks to implement *in vivo* small animal EIXPCT. The biomaterial studies will have a significant impact on the fields of biomaterials, regenerative medicine and tissue engineering.

There are two different challenges posed by the task and the solutions are also different.

The first challenge is the data-acquisition time requirement imposed by the *in vivo* imaging application. Data-acquisition lasting hours long is not acceptable. Through combined use of a MetalJet (MJ) source and the joint reconstruction methods, we may potentially achieve *in vivo* imaging. The MJ source circumvents the brightness limitations of conventional micro-focus X-ray sources by replacing the solid anode target with a high-speed liquid metal jet that is already molten. The joint reconstruction method can reduce data-acquisition time significantly by allowing single-shot imaging. Dithering should be avoided for the *in vivo* imaging applications, because every second must be squeezed out for *in vivo* imaging but dithering always require longer data-acquisition time. When strict resolution requirement is imposed, the partial-dithering strategy can be employed as a compromise.

The second challenge is imposed by the object size, especially thickness. From a general perspective, thick objects presents many problems from different aspects for XPCT imaging. The most challenging problem is phase-wrapping [32, 33], where the phase-shift caused by refraction exceeds 2π, thus creating ambiguity about the exactly phase-shift. In a conventional two-step reconstruction method, the phase-wrapping often leads to stripes in the differential phase images obtained from the phase retrieval step, and require special processing methods [58] to generate the unwrapped sinogram for tomographic reconstruction. A solution for the phase-wrapping effect has not yet been developed for the JR method, and future work is required to solve this problem. We restrict the scope of this study to imaging objects that are free from phase-wrapping. In this study, we are only interested in imaging mouse and rat, which has the thickness of a few centimeters. These objects do not have phase-wrapping problems.

However, even if phase-wrapping is not involved, thick objects still introduce other problems. Thick objects tend to absorb much more strongly than thin objects, so, the intensity of the output X-rays after interaction with thick objects are weaker than those interacting with

thin objects, considering the same incident X-ray intensity. Weaker X-ray intensity can lead to higher noise level and thus degrade the quality of reconstructed images.

Also, in tomography, the object thickness in one view angle is the width from another view angle, so the entire system has to be made wider to contain the entire object inside the field of view (FOV). Wider masks make the production harder and also the mask alignment process more difficult. Wider cameras restrict the selection of X-ray detectors, excluding some high-end cameras which are small in size.

7.2   System design and implementation

7.2.1   Design goal

Phase contrast imaging techniques are mainly designed to exploit refractive information. Therefore, the quality of the reconstructed image of refractive index decrement distribution, δ, is more important than the absorption image. The designing for this system focuses on two aspects:

- Improving δ signal contrast;

- Reducing the noise level in δ image.

Based on Equation (2.15), considering all other conditions to be unchanged, the δ signal contrast increases when the derivative of illumination curve is increased. The δ contrast is based on the difference of absorption between the non-blocking region and blocking region of the mask. Ideally, the non-blocking region should not absorb any photon and the blocking region should absorb 100% of the photons, but this will not happen in reality. There are always photons absorbed by the non-blocking region and photons transmitting through the

blocking region. However, if the difference in transparency is large between the non-blocking region and the blocking region, the derivative of the illumination curve can still be quite large [40]. The design discussions tries to maximize the transparency difference.

The noise level in the image is mainly affected by the overall illumination level. When the illumination level is higher, or in other words, when the number of photons detected is higher, the noise level is lower. There are two aspects to consider for minimizing noise. First, use a bright source that generates high output. Second, tune the mask parameters to minimize the unnecessary absorption.

In this work, the designing of the system parameters will be mainly focusing on these two aspects.

7.2.2 Selection criteria of important system parameters

There are four main optical elements in the optical system: the source, two masks and a detector. Parameters of these components may affect the image quality.

- **Source output.** The source output should be maximized to the upper limit imposed by the source capacity. A brighter source increases the overall photon count and reduces noise without significant side effect. It also provides possibility of reducing exposure times and consequently, the radiation doses.

- **X-ray spectrum.** The laboratory-based X-ray source is usually a polychromatic source, so spectrum plays an important role in the quality of acquired images. The peak energy of the spectrum should not be too weak so that beam hardening becomes significant. However, having a too strong peak energy also has a side effect. Higher-energy X-rays are hard to absorb, and thus the transparency of the mask's blocking region can be

high, limiting the δ signal sensitivity. Also, the spectrum of the source should better match the optimized energy range of the detector to maximize the efficiency.

- **Mask substrate material and thickness.** The structure for a mask is given in Figure 7.1. Gold is deposited on the substrate in the designed regions. The substrate is necessary for mask production and providing support for the golden layer on top of it. Substrate does not help the EIXPCT imaging process, but it still affects the optical system by absorbing a portion of incident X-rays. Different vendors provide different options for the mask substrate. In this work, the choice was made between two options: a 0.3 mm thick silicon substrate and a 0.5 mm graphite.

Figure 7.1: The section of a typical mask. The gold is deposited onto the surface of some substrate.

- **Mask (gold) thickness.** For simplicity, when mask thickness is referred to, we mean the thickness of the golden layer in the mask. Mask thickness is one of the two most important parameters in an EIXPCT system. Mask thickness is a flexible parameter that can be tuned continuously. It directly affects the transparency of the blocking region of masks, and thus affects the δ signal sensitivity as well as the noise level [40, 41]. A thicker mask is more beneficial of δ signal sensitivity but reduces the overall photon throughput and thus increases the noise level. Selection of mask thickness should be a compromise of the two effects.

- **Mask gap ratio.** The gap ratio is defined to be the ratio between the gap width and the mask period. It is the other one of the two most important parameters. The period of the mask is usually the same as the detector pitch corrected for cone beam geometry, except for a special mask design called line-skipping [25] to be introduced below. Selection of the gap ratio is also a compromise. A smaller gap ratio increases the δ signal sensitivity but reduced the overall illumination level [40].

- **Detector spill-over and line-skipping.** Spill-over of signal denotes the effect that part of the signal that should have been collected only by one pixel diffuses to neighboring pixels. Spill-over effectively blurs the image and is harmful for δ signal detection and thus should be minimized [40], but people usually have limited control over it. We cannot continuously tune it and it can hardly be eliminated. Besides selecting a camera with little spill-over, an alternative way to mitigate the effect of spill-over is to employ a design called line-skipping [25]. Figure 7.2 compares the vanilla mask design and the line-skipping design. Using line-skipping technique, the mask period is twice the detector pitch corrected for cone beam geometry. The line-skipping design neglects the
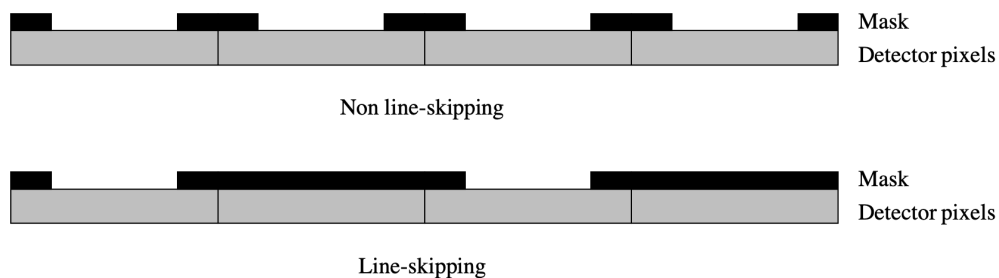
Figure 7.2: A non line-skipping design and a line-skipping design. In the line-skipping design, every other pixel is completely covered by the mask. Thus the pixel is "skipped".

skipped pixel, and thus is immune to the spill-over effect to the first neighbor pixel. Line-skipping is necessary for a detector with significant spill-over.

- **Other detector specs.** The size of the imaged animal requires the detector region to be large. Also, the strong absorption from thick objects requires a high dynamic range. Finally, an *in vivo* imaging application prefers the data-acquisition process without dithering. Thus, the resolution of the reconstructed image is largely dependent on the pitch size of the detector. A smaller pitch size is preferred for better resolution.

7.2.3   System design

Based on the discussions, a typical EIXPCT system was constructed in our lab designed for pre-clinical imaging applications. Photos of the optical system is shown in Figure 7.3.

The X-ray source was the Excillum MetalJet D2. The MetalJet source circumvents the brightness limitations of conventional microfocus X-ray sources by replacing the solid anode target with a high-speed liquid metal jet that is already molten. The MetalJet anode is composed of a gallium-based alloy with indium and tin components (Gallinstan). The indium Kalpha line at 24.2 keV is well-suited for the design energy range, and its presence with other lines produces a spectrum where the 20-30 keV flux is an order of magnitude higher than the corresponding 10-40 keV bremsstrahlung continuum fluxes. The spatial stability of the MetalJet source is very high with a characteristic spot centroid standard deviation of $< 0.1\,\mu$m over 24 hours corresponding to 5% of the absorption grating period in our imager design. A flat panel X-ray detector, Shad-o-Box 6K HS (Teledyne DALSA), was selected to be the detector of the EIXPCT system, mainly for its large size of detection area. The detector employs the CMOS X-ray sensor technology. It is optimized for the 40-160 kV energy range but cover both the low (10-50 kV) and extended (up to 225 kV) energy ranges. It has a wide dynamic range of 3000 : 1 and a large active area of 11.4×14.6 cm^2. The pitch is $49.5\,\mu$m, which is relatively small among flat panel detectors. A maximum of 9 frames can be obtained in a second.
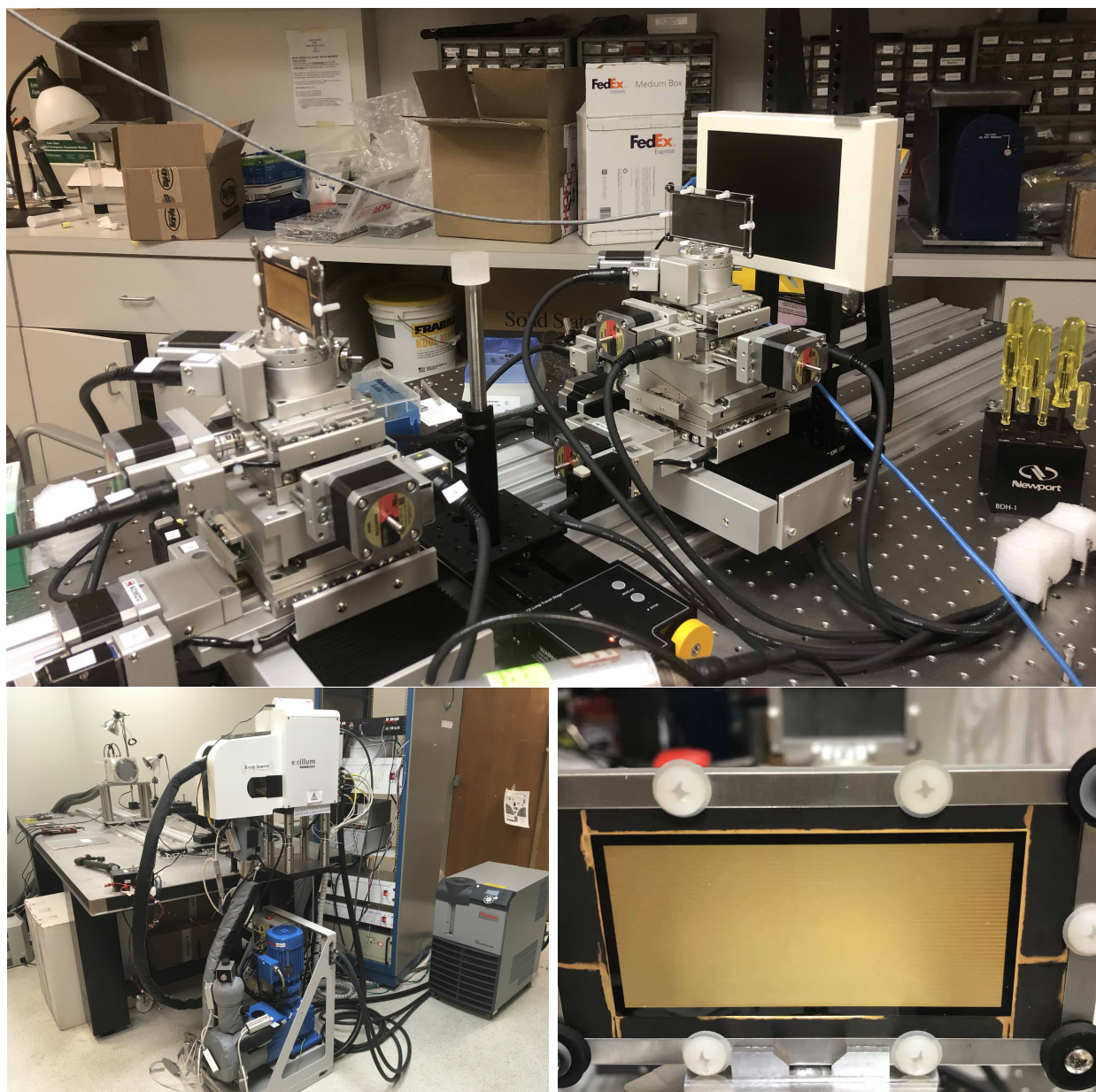
Figure 7.3: (Top) The laboratory-based EIXPCT setup showing the two masks, the rotation table and the Shad-o-Box detector. (Bottom left) The MetalJet source. (Bottom right) A close view of the sample mask

The sample and detector masks were made by CreaTv MicroTech. Because the spill-over is large for the detector, both of the masks employed line-skipping strategy. The sample mask was produced with $75.2\,\mu\mathrm{m}$ pitch and $15.0\,\mu\mathrm{m}$ gap with $60\,\mu\mathrm{m}$ gold on 0.5 mm thick graphite. The total size is approximately $3.2\,\mathrm{cm}\times7.0$ cm. The detector mask was produced with $95.0\,\mu\mathrm{m}$ pitch and $19.0\,\mu\mathrm{m}$ gap with $60\,\mu\mathrm{m}$ gold on 0.5 mm thick graphite. The total size is approximately $4.0\,\mathrm{cm}\times8.8$ cm. The masks were intentionally designed to be wide enough to cover the width of a rat. As a compromise, the height of the mask is relatively short but the object can be moved up and down to select the imaged region, and thus the entire object can be imaged. The periods of the masks were selected based on designed system geometry. The distance between the source and the detector is 2 m. The distance between the source and the first mask is 1.52 m, while that between the source and the second mask is 1.92 m. The gap ratio of 40% and the gold thickness is selected to maintain a balance between signal sensitivity and photon throughput [40]. A set of KOHZU precision position stages were employed for manipulation of mask location. These stages allow free movement in all 6 degree of freedom.

7.2.4   Mask alignment

Mask alignment seeks to place the two masks such that

- The mask planes and the detector plane are all parallel to each other;

- The gratings of the masks and the detector columns are all parallel to each other;

- The two masks are placed at the correct locations in the x-axis. This requirement means that one period in the mask will cast a shadow in the detector that has the width of a single detector pixel.

The standard mask alignment procedure mainly follows the approach proposed by Millard *et. al.*[34]. Larger masks impose higher requirements for mask alignment because the entire mask region need to satisfy the above requirements. Our alignment procedure made minor modifications to the standard procedure to include guidance for a few unaddressed situations in the original paper.

The alignment is a two-step process: one of the two masks is first aligned with the detector, and later on, the second mask is aligned with the first one. The alignment procedure is similar for the two processes, because the active area generated by the electrode in the detector pixel is non-uniform [45, 62]. Typically, the electron collection efficiency is higher in the center of each pixel and lower towards the edges. Thus, the manufacturing imperfectness works like a built-in mask for the detector, and thus aligning the first mask with the detector is similar to aligning the mask with the built-in mask. For simplicity, there will be no distinction made between the two alignment steps.

Theoretically, when masks are aligned perfectly, every pixel in the detector will provide a same measured intensity reading in an air scan. When one of the mask (denoted as the moving mask) is moved along the y-axis, the intensity changes. When the gap regions from the two masks overlap with each other, the maximum intensity is observed. In reality, the intensity readings from all pixels are never exactly the same because of many factors, including non-uniformity of mask thickness and artifacts along the optical path. The exact value of measured intensity is often too noisy to be useful, but the mask-displacement corresponding to the maximum intensity is much less noisy. The masks alignment is considered successful when all pixels obtain the maximum intensity at the same moving mask location.

The standard mask alignment procedure lets the moving mask move along the y-axis and stop at S different sub-period distances, Δy_i ($i = 1, 2, ..., S$), during which measured intensities,

$g(x, y; \Delta y_i)$, are obtained in the air scan. Later, the mask position for which the maximum intensity is obtained is extracted as

$$G(x, y) = \min_i g(x, y; \Delta y_i). \tag{7.1}$$

Ideally, $G(x, y)$ is a constant when the alignment is successful.

$G(x, y)$ will follow several different patterns. Analyzing the patterns will guide the mask movement for better alignment. Figure 7.4 demonstrates all the typical patterns. Except for the pattern in Figure 7.4(a), all patterns can be interpreted as a group of bars with different indices. If the indices are listed from the left-most bar to the right-most bar, it can be classified into monotonous index change and non-monotonous index change. The monotonous index change means that the listed indices are monotonously changing. Note that an index switch between S and 1 is caused by the periodical nature of the indices and is not considered to break the monotony. The non-monotonous index change means that the listed indices are non-monotonously changing. A typical example is $1, 2, 3, 4, 3, 2, 1$. The moving mask should be moved according to the following suggestions until a uniform $G(x, y)$ image is obtained:

- Figure 7.4(a): finger-tip patterns – move the masks along the optical axis to obtain any of the following patterns.

- Figure 7.4(b): curved bars, monotonous index change – rotate around the horizontal axis which is perpendicular to the optical axis. The bars will not be curved after appropriate correction.

- Figure 7.4(c): parallel tilted bars, monotonous index change – rotate around the optical axis. The bars will not be tilted after appropriate correction.

- Figure 7.4(d): parallel vertical bars with unequal spacing, monotonous index change – rotate around the vertical axis. The bars will have equal spacing after appropriate correction.

- Figure 7.4(e): parallel vertical bars with non-monotonous index change – rotate around the vertical axis. You will either see pattern (f) or observe a uniform $G(x,y)$ image after appropriate correction.

- Figure 7.4(f): parallel vertical bars with equal spacing, monotonous index change – move the mask along the optical axis. The bars may be wider and ultimately $G(x,y)$ becomes uniform.

The alignment procedure is implemented in a coarse to fine fashion. During the earlier alignment process, the gaps between neighboring Δy_i $(i = 1, 2, ..., S)$ are large, so a coarse alignment can be easily achieved. After the coarse alignment, the gaps between neighboring Δy_i $(i = 1, 2, ..., S)$ will be smaller and high accuracy alignment can be achieved.
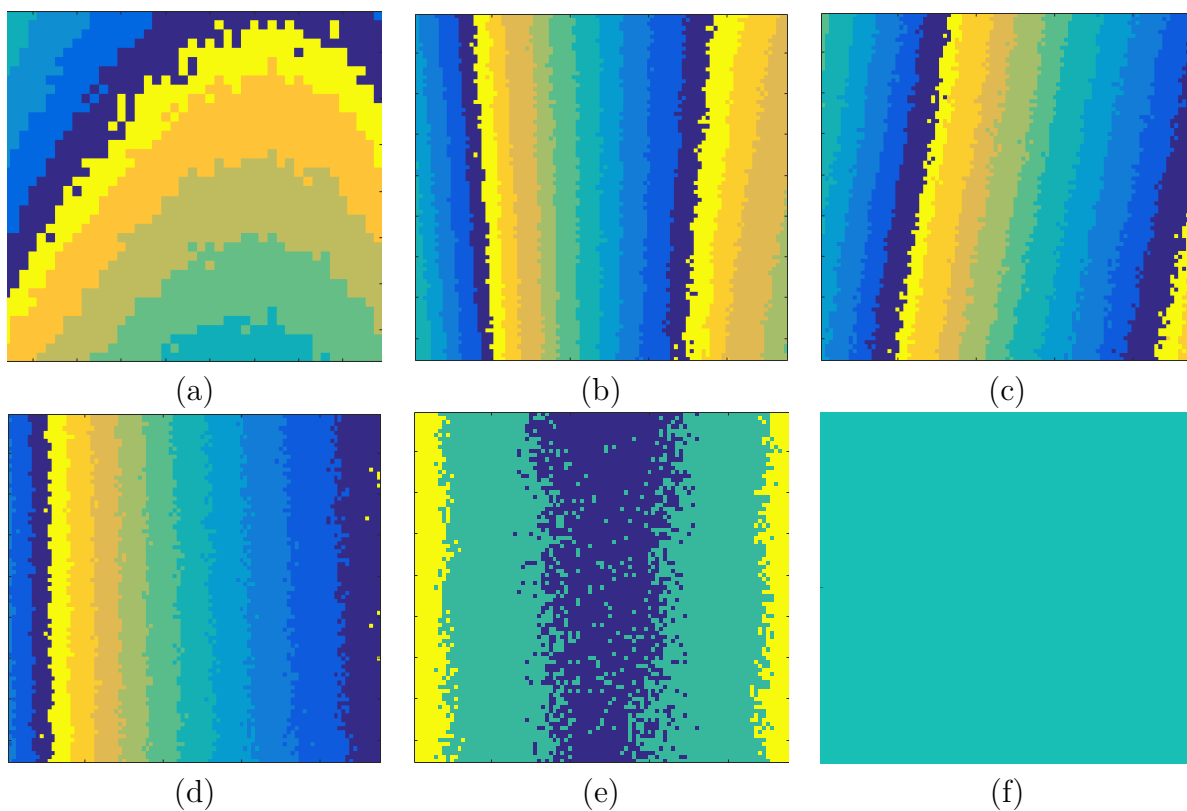
Figure 7.4: The G images for four different situations: (a) curved bars, (b) tilted bars, (c) unequal spacing, (d) converging to center. Note that these images are simply a demonstration of trend. If you follow our alignment procedure, you won't see so many bars (more than 10) as in (a)-(c). When you do see these many bars, you will be see the Moore pattern directly by eyes and it means you haven't done a good job in the rough alignment step. In this experiment, the moving mask stopped at 10 different Δy locations. The index of the locations is shown instead of the actual Δy values.

7.3 Preliminary imaging studies

7.3.1 Methods

A preliminary imaging study was conducted to verify the performance of the constructed system. There are two types of imaged objects: artificial phantoms and biological samples. Figures of all the objects imaged are shown in Figure 7.5.

PMMA phantom A phantom made from Poly(methyl methacrylate) (PMMA), also known as acrylic, shown in Figure 7.5(a) is employed in this study. The cylindrical object has the diameter of 3 cm, close to that of a mouse. The material has similar absorption properties to water and soft tissue in general. Through holes of varying sizes are made in the phantom for better analyzing resolution. The phantom was imaged inside a syringe where the internal holes were filled with liquid. Liquid options include water and isopropyl alcohol. The theoretical properties of the relevant materials can be found in Tab. 7.1.

3D printed ABS phantoms Theoretically, arbitrary-shaped multi-material objects can be printed using 3D printing technology. Recently, 3D printing has been explored as an option for generating tissue phantoms for phase contrast imaging [17, 26]. In this work, the possibility of using 3D printed objects was briefly explored. ABS material was employed in printing the 3D phantom for its resemblance to water in terms of refractive index decrement values [23, 26, 50]. The shape of this printed phantom shown in Figure 7.5(b) was a large cylinder with four cylinder-shaped blind holes. The diameter of the large cylinder was 3 cm, close to that of a mouse. The diameters of the small holes were all 1 cm. Liquids were filled in the blind holes to mimic different tissue types. The filling liquids were selected to be ethanol-water mixtures. Four options were employed: pure ethanol, ethanol 75%, ethanol

| (a) | (b) | (c) | (d) |
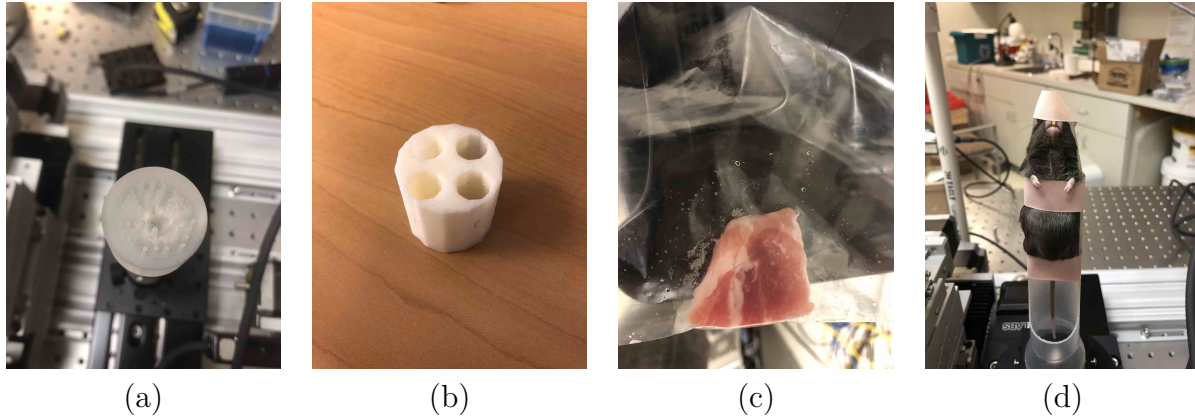
Figure 7.5: A collection of objects being imaged in EIXPCT system. From left to right: (a) PMMA phantom, (b) 3D printed ABS phantom, (c) pork sample, (d) a sacrificed mouse.

50%, and pure water. Here, ethanol is mixed with water based on volume. The ethanol 75% mixture is produced by mixing 15 ml ethanol with 5 ml water. The ethanol 50% mixture is produced by mixing 10 ml ethanol with 10 ml water. the theoretical properties of ABS and the four mixtures can be found in Tab. 7.1. The refractive index decrements of water and ABS are close, but the absorptions are quite different from each other. The absorptions of ethanol and ABS are close, but the refractive index decrements are quite different from each other.

Pork sample A pork sample was imaged with the EIXPCT system and is shown in Figure 7.5(c). The pork contained lean meat as well as fat meat. There was also a small piece of bone inside the sample.

Sacrificed mouse A sacrificed mouse shown in Figure 7.5(d) was also imaged with the system to test the system's capability to image a complicated biological object. The head and upper lung components of the mouse was imaged.

Table 7.1: The theoretical properties of the relevant materials are listed in this table, including composition, density, refractive index decrement (δ) value, and absorption (β) value [3, 22, 28, 29, 52].

Name	Composition	density (g/cm^3)	δ ($\times 10^{-7}$)	β ($\times 10^{-10}$)
ABS	$C_{15}H_{17}N$	1.07	4.16	1.49
Ethanol	C_2H_6O	0.79	3.21	1.37
Ethanol 75%		0.86	3.47	1.60
Ethanol 50%		0.91	3.69	1.83
Isopropyl alcohol	C_3H_8O	0.79	3.21	1.30
PMMA	$C_5H_8O_2$	1.18	4.63	2.01
Water	H_2O	1.00	4.00	2.27

The two artificial phantoms were imaged in a tomographic setting. The source power was selected to be 100W and the voltage was 70kV. The source focal spot was a $40\,\mu$m$\times 10\,\mu$m rectangle. In this preliminary imaging process, image quality was prioritized over data-acquisition time. Thus, images were acquired at both of the optimal mask locations at all tomographic view angles, which were evenly distributed in a 2π range with a $1°$ interval in every neighboring view angles. Each exposure lasted for 5 seconds.

The two biological samples were imaged only for a single view angle. Ten images were also acquired at each of the two optimal mask locations, and each exposure lasted 10s. All of the 10 images acquired at the same location were averaged to minimize noise. Phase retrieval was applied to these averaged images to obtain an absorption projection image and a differential phase image as defined in Equation (2.21) and Equation (2.22), respectively. The source power was selected to be 70W and the voltage is 45kV. The source focal spot was a $40\,\mu$m$\times 10\,\mu$m rectangle.
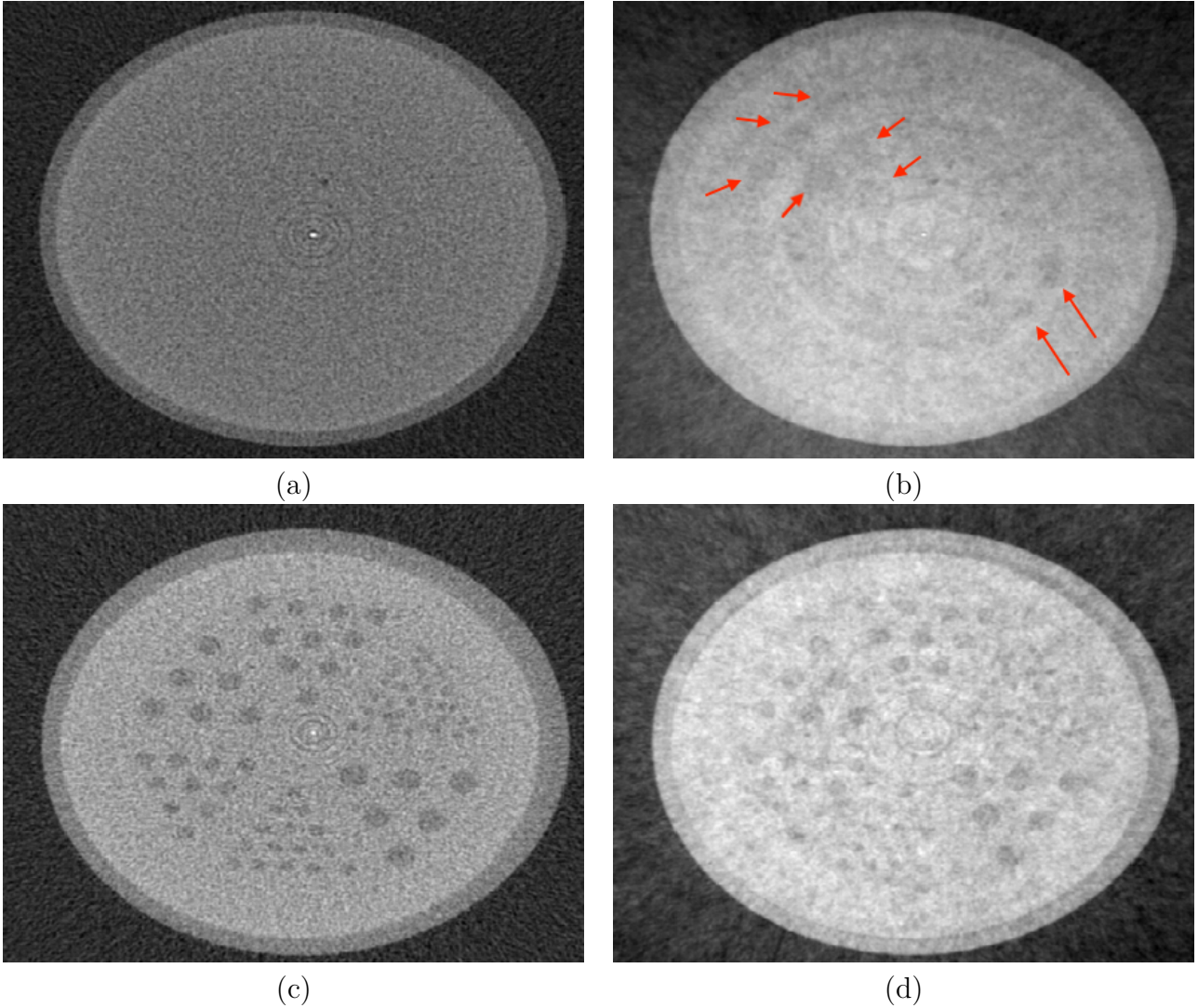
Figure 7.6: The reconstructed absorption distribution (a, c) and refractive index decrement distribution (b, d) of the PMMA with different water (a, b) or alcohol (c, d). The differentiation of isopropyl alchhol and PMMA is clear from both β image and δ image. The differentiation of water and PMMA is more clear in δ image than in β image.

7.3.2 Results: Phantoms

The reconstructed β and δ images of the PMMA phantom are shown in Figure 7.6. The system is capable of doing tomographic imaging of the phantom with 3 cm thickness. In general, the β image suffers more from high-frequency noise and δ image suffers more from low frequency noise. It is easy to differentiate between the alcohol and the PMMA material from both absorption and refractive index decrement distributions. However, differentiating between PMMA and water is much harder. From the reconstructed absorption image, the two materials are completely mixed. From the reconstructed refractive index decrement image, some large holes containing water can still be differentiated from the PMMA background, showcasing the benefit of phase imaging.

The reconstructed images of the ABS phantom are shown in Figure 7.7. The reconstructed images can show all the designed structures and some air gaps between the printed materials, showing defects of the 3D printing process. Among the four different ethanol-water mixtures, the β images can differentiate pure water and ethanol 50% mixture but not the other two, and the δ image can differentiate pure ethanol and ethanol 75% mixture but not the other two. In general, an ethanol-water mixture with more water components can only be differentiated from the ABS background in β image, and that with more ethanol components can only be differentiated from the ABS background in δ image. This study demonstrates the necessity of obtaining both δ and β images in provide material differentiation. Generating more ethanol-water mixture can help identify the minimum δ or β difference that the current system can resolve.
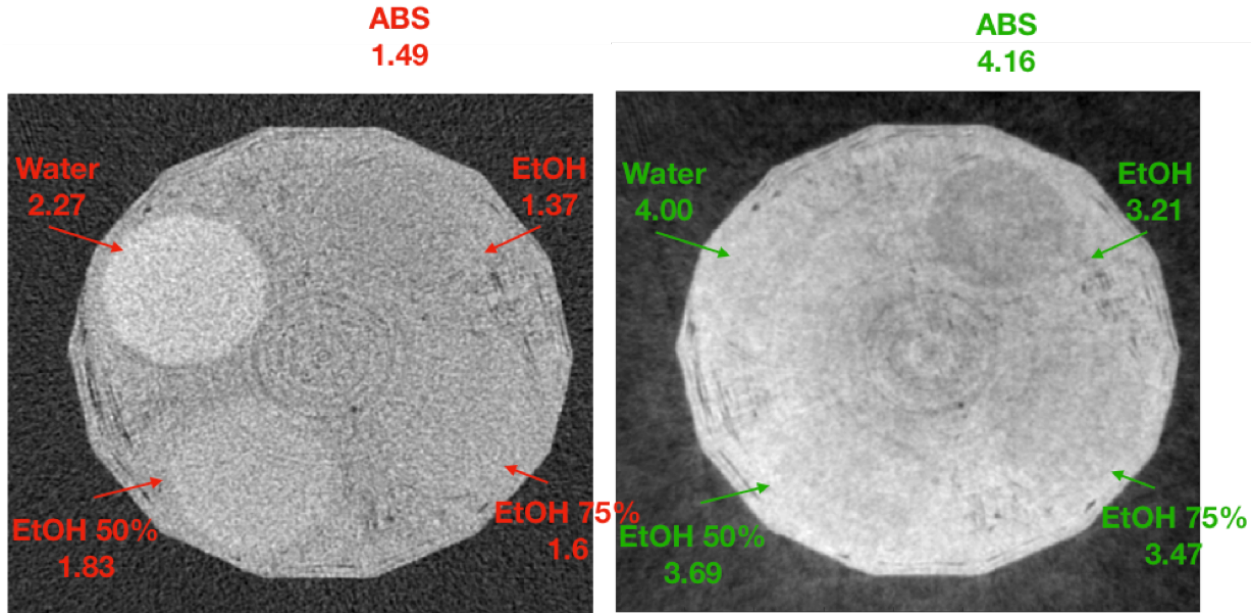
Figure 7.7: The reconstructed absorption distribution (left) and refractive index decrement distribution (right) of the 3D printed ABS phantom. The filling liquids and their corresponding theoretical β (red, in the unit of $\times 10^{-10}$) and δ (green, in the unit of $\times 10^{-7}$) values are marked in the figure. Here EtOH represents pure ethanol. EtOH 75% (or EtOH 50%) represent an ethanol-water mixture with a volume ratio of 3:1 (or 1:1). The absorption image provides easier differentiation between ABS and water. The refractive index decrement image provides easier differentiation between ABS and ethanol.

7.3.3   Results: Biological tissues

The absorption projection image and the differential phase image of the pork sample is shown in Figure 7.8. The absorption projection image shows the bone region more clearly, but the differential phase image is better at resolving the structures of the soft tissue, which is especially clear in the region marked by the red arrows.

The absorption projection image and the differential phase image of the mouse sample shown in Figure 7.9 show a similar relationship. The differential phase image shows the trachea

117
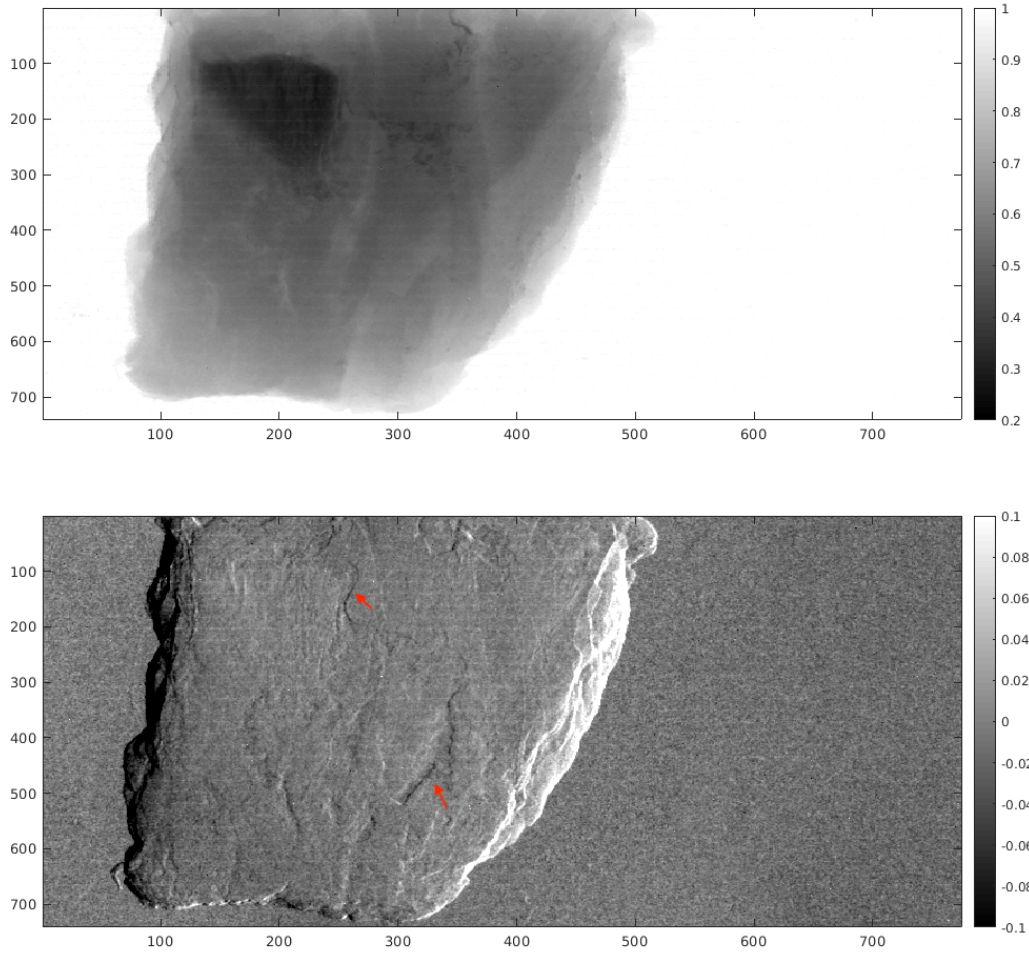
Figure 7.8: The retrieved absorption projection image (top) and the differential phase image (bottom) of a pork sample. From the differential phase image, many tissue interfaces become clearer.
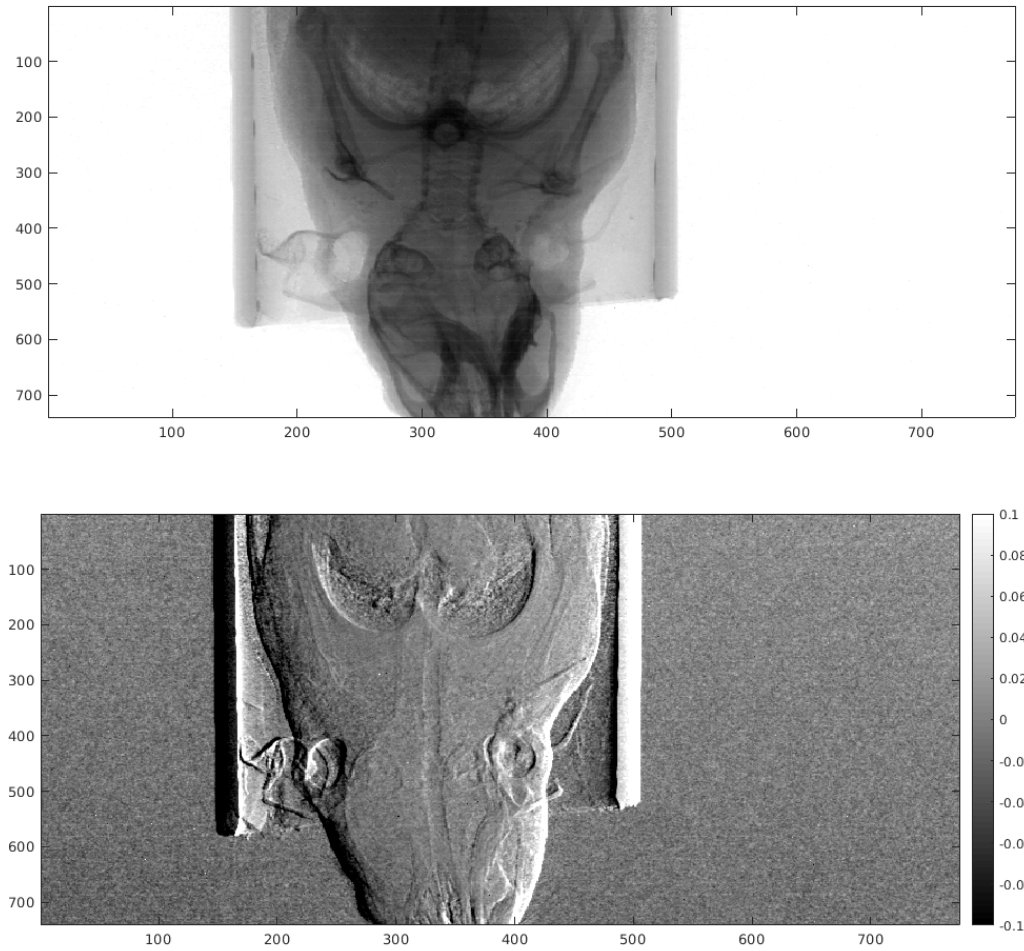
Figure 7.9: The retrieved absorption projection image (top) and the differential phase image (bottom) of a mouse sample. The lung region in the differential phase image becomes much more detail-enriched than that in the absorption image.

region much more clearly. Moreover, the lung region of the differential phase image contains much more details than the absorption image.

These differential phase images of the biological samples are promising. However, these images are integrated from multiple exposures, and thus such image quality requires long data-acquisition times. An exposure time of approximately 3s is too short to resolve so many details. All the structures will be immersed in noise. The tomographic reconstruction is also still highly contaminated in noise. In future upgrade of the system, noise suppression should be a priority to make *in vivo* tomographic δ imaging more realistic.

7.4   Conclusion

In this work, an EIXPCT system has been designed and implemented for pre-clinical applications. The key components of the system include a bright MetalJet source, two large masks, and a Shad-o-Box flat panel detector that has large field-of-view, small pitch size and high dynamic range. The revised mask alignment procedure has been proposed and implemented in the laboratory system successfully.

The phantom imaging study and biological tissue imaging study performed in the lab have shown that the EIXPCT system is capable of imaging biological object with 3 cm thickness without encounter severe problems posed by object thickness. The comparison between the absorption image and refractive index decrement image showcased the necessary of obtaining refractive index decrement image alongside with absorption image for material differentiation. For some materials, the refractive index decrement difference may be larger and easier to detect than the absorption difference.

The current system, however, still suffers from high noise level in the retrieved δ information when the exposure time is restricted for *in vivo* applications, and thus may obscure detailed structure in the δ images. In the future, the system design can be further improved to suppress noise, with potential strategies like adjusting mask thickness and gap ratio.

Chapter 8

Summary

In this dissertation, a novel joint reconstruction (JR) method was proposed enabling single-shot edge-illumination X-ray phase-contrast tomography (EIXPCT). The JR method was formulated as an optimization problem that can be solved by gradient-based algorithms. The proposed method possesses advantages over previously-proposed single-shot methods for EIXPCT. The method does not require the assumption of a single material object [12]. Moreover, it does not require a parallel-beam geometry [19] and can be applied to the case of a cone-beam geometry where the incident beam divergence must be considered. Additionally, the method does not require use of an energy-sensitive detector [10] and can be employed with readily available integrating X-ray detectors.

The numerical properties of the JR method were explored to gain a deeper understanding of this method. The optimization problem was shown to be non-convex, but the accurate reconstructed images of random phantoms suggests that the non-convexity will not be a significant obstacle if zero initial guesses are employed. This conclusion guides the selection of initial guesses in the JR algorithm. During the JR process, the two channels (absorption, β,

and refractive index decrement, δ) exhibit little cross-talk effect, which suggests the robustness and reliability of the algorithm. Finally, the noise statistics of reconstructed images were studied and compared. JR with proper regularization yields smaller reconstruction error compared with conventional methods due to its iterative nature of implicit phase retrieval as well as its regularization. This observation demonstrates the advantage of the JR method over the conventional two-step approach.

Moreover, a series of flexible data-acquisition designs are enabled by the JR method. The JR method was combined with a variety of data-acquisition designs that differ from each other in terms of mask-displacement strategy and the tomographic scanning angular range. As a result, these investigated designs differed in terms of their data-acquisition time (proportional to the number of images acquired), data-acquisition simplicity (the need to move the mask position), and reconstruction stability and quality. The feasibility of these designs were investigated, and three representative designs were selected for the low artifact level of their reconstructed images from an idealized noise-free simulated measurement dataset. Later, the numerical properties of the reconstruction method were revisited in combination with the three representative data-acquisition designs, including cross-talk, reconstructed image noise level, and resolution. Different data-acquisition designs have different advantages. The CAP(2π) design has the simplest data-acquisition procedure because the masks do not need to be moved, but it may be more affected by model mismatch in practice. The AAP(2π) design demonstrates the highest quality reconstructed image because it has low noise and is less affected by the model mismatch problem, but it requires extra mask movement and a relatively long data-acquisition time. The AAP(1π) design has the shortest data-acquisition time due to its small angular coverage range and single-shot design. However, images reconstructed from data acquired by the AAP(1π) design are slightly degraded by noise. Consequently, the

selection of a data-acquisition design should be optimized based on the specific needs of the application.

The JR method also allows flexible design about another component of the data-acquisition design, which is related to the dithering technique that was proposed to enhance the image resolution produced by EIXPCT systems. In the dithering technique, the sample is translated by a series of sub-pixel distances and measurement data are taken at the dithering locations. The measurements are later synthesized into a higher-resolution image, from which an enhanced resolution reconstructed image can be obtained. The main drawbacks of the dithering technique are prolonged data-acquisition times and increased radiation doses. To mitigate these, a partial-dithering strategy was proposed for EIXPCT systems where dithering is applied periodically at a subset of tomographic view angles. Partial-dithering is the first exploration of novel dithering strategies. Compared with the conventional full-dithering technique, partial-dithering greatly reduces data-acquisition time but improves spatial resolution over the no-dithering case. Partial-dithering provides a viable solution to decrease data-acquisition time when high resolution is required in tomographic imaging. The JR reconstruction was slightly modified to include two steps for optimal reconstruction speed. The dithered views are weighted more heavily in the second JR step to maximize the image quality improvement. It has been demonstrated that, with partial-dithering, the image resolution can be much improved with smaller increase in data-acquisition time compared with full-dithering.

An EIXPCT system was designed and implemented for pre-clinical application. The key components of the system include a bright MetalJet source, two large masks, and a Shad-o-Box flat panel detector that has large field-of-view, small pitch size and high dynamic range. The revised mask alignment procedure has been proposed and implemented in the laboratory system successfully. The phantom imaging study and biological tissue imaging

study performed in the lab have shown that the EIXPCT system is capable of imaging biological object with 3 cm thickness. The comparison between the absorption image and refractive index decrement image showcased the advantage of obtaining refractive index decrement image alongside with absorption image for material differentiation. For some materials, the refractive index decrement difference may be larger and easier to detect than the absorption difference.

Despite current progress, many aspects remain to be investigated from both the software side and the hardware side. From the software side, in the future, more flexible mask-displacement strategy and dithering strategy can be explored with the help of the JR method. These two strategies can even be combined to allow more flexible data-acquisition process, and these creative designs have the potential of obtaining better reconstructed image quality and even shorter data-acquisition time. From the hardware side, the current *in vivo* animal model imaging system still suffers from high noise level in the retrieved δ information, and thus may obscure detailed structure in the δ images. In the future, the system design can be further improved to suppress noise, and thus supports fast imaging with high quality.

References

[1] Amir Beck and Marc Teboulle. "A fast iterative shrinkage-thresholding algorithm for linear inverse problems". In: *SIAM journal on imaging sciences* 2.1 (2009), pp. 183–202.

[2] Dimitri P Bertsekas. *Nonlinear programming*. Athena scientific Belmont, 1999.

[3] S Brennan and PL Cowan. "A suite of programs for calculating x-ray absorption, reflection, and diffraction performance for a variety of materials at arbitrary wavelengths". In: *Review of scientific instruments* 63.1 (1992), pp. 850–853.

[4] Xavier Bresson and Tony F Chan. "Fast dual minimization of the vectorial total variation norm and applications to color image processing". In: *Inverse problems and imaging* 2.4 (2008), pp. 455–484.

[5] Tony Chan, Selim Esedoglu, Frederick Park, and A Yip. "Recent developments in total variation image restoration". In: *Mathematical Models of Computer Vision* 17.2 (2005).

[6] Tony F Chan, Gene H Golub, and Pep Mulet. "A nonlinear primal-dual method for total variation-based image restoration". In: *SIAM journal on scientific computing* 20.6 (1999), pp. 1964–1977.

[7] Yujia Chen and Mark A Anastasio. "Properties of a Joint Reconstruction Method for Edge-Illumination X-ray Phase-Contrast Tomography". In: *Sensing and Imaging* 19.1 (2018), p. 7.

[8] Yujia Chen, Weimin Zhou, and Mark A Anastasio. "Joint-reconstruction-enabled data acquisition design for single-shot edge-illumination x-ray phase-contrast tomography". In: *Medical Imaging 2018: Physics of Medical Imaging*. Vol. 10573. International Society for Optics and Photonics. 2018, p. 1057322.

[9] Yujia Chen, Huifeng Guan, Charlotte K Hagen, Alessandro Olivo, and Mark A Anastasio. "Single-shot edge illumination x-ray phase-contrast tomography enabled by joint image reconstruction". In: *Optics Letters* 42.3 (2017), pp. 619–622.

[10] Mini Das and Zhihua Liang. "Spectral x-ray phase contrast imaging for single-shot retrieval of absorption, phase, and differential-phase imagery". In: *Optics letters* 39.21 (2014), pp. 6343–6346.

[11] TJ Davis, D Gao, TE Gureyev, AW Stevenson, and SW Wilkins. "Phase-contrast imaging of weakly absorbing materials using hard X-rays". In: *Nature* 373.6515 (1995), p. 595.

[12] Paul C Diemoz et al. "Single-image phase retrieval using an edge illumination X-ray phase-contrast imaging setup". In: *Journal of synchrotron radiation* 22.4 (2015), pp. 1072–1077.

[13] PC Diemoz, A Bravin, and P Coan. "Theoretical comparison of three X-ray phase-contrast imaging techniques: propagation-based imaging, analyzer-based imaging and grating interferometry". In: *Optics express* 20.3 (2012), pp. 2789–2805.

[14] PC Diemoz, CK Hagen, M Endrizzi, M Minuti, R Bellazzini, L Urbani, P De Coppi, and A Olivo. "Single-Shot X-Ray Phase-Contrast Computed Tomography with Nonmicrofocal Laboratory Sources". In: *Physical Review Applied* 7.4 (2017), p. 044029.

[15] Belma Dogdas, David Stout, Arion F Chatziioannou, and Richard M Leahy. "Digimouse: a 3D whole body mouse atlas from CT and cryosection data". In: *Physics in Medicine & Biology* 52.3 (2007), p. 577.

[16] Marco Endrizzi, Alberto Astolfo, Fabio A Vittoria, Thomas P Millard, and Alessandro Olivo. "Asymmetric masks for laboratory-based X-ray phase-contrast imaging with edge illumination". In: *Scientific reports* 6 (2016).

[17] G Esposito et al. "240. Evaluation of 3D printing materials for breast phantoms for phase contrast imaging". In: *Physica Medica* 56 (2018), p. 210.

[18] Charlotte K Hagen et al. "Quantitative edge illumination x-ray phase contrast tomography". In: *SPIE Optical Engineering+ Applications*. International Society for Optics and Photonics. 2014, pp. 921205–921205.

[19] Charlotte K Hagen, Marco Endrizzi, Paul C Diemoz, and Alessandro Olivo. "Reverse projection retrieval in edge illumination x-ray phase contrast computed tomography". In: *Journal of Physics D: Applied Physics* 49.25 (2016), p. 255501.

[20] CK Hagen, PRT Munro, M Endrizzi, PC Diemoz, and A Olivo. "Low-dose phase contrast tomography with conventional x-ray sources". In: *Medical physics* 41.7 (2014), p. 070701.

[21] CK Hagen, PC Diemoz, M Endrizzi, and A Olivo. "The effect of the spatial sampling rate on quantitative phase information extracted from planar and tomographic edge illumination x-ray phase contrast images". In: *Journal of Physics D: Applied Physics* 47.45 (2014), p. 455401.

[22] BL Henke, EM Gullikson, and JC Davis. *Atomic Data and Nuclear Data Tables Vol. 54*. 1993.

[23] Julia Herzen, Tilman Donath, Franz Pfeiffer, Oliver Bunk, Celestino Padeste, Felix Beckmann, Andreas Schreyer, and Christian David. "Quantitative phase-contrast tomography of a liquid phantom using a conventional x-ray tube source". In: *Optics express* 17.12 (2009), pp. 10010–10018.

[24] John H Hubbell and Stephen M Seltzer. *Tables of X-ray mass attenuation coefficients and mass energy-absorption coefficients 1 keV to 20 MeV for elements Z= 1 to 92 and 48 additional substances of dosimetric interest.* Tech. rep. National Inst. of Standards and Technology-PL, Gaithersburg, MD (United States). Ionizing Radiation Div., 1995.

[25] K Ignatyev, PRT Munro, RD Speller, and A Olivo. "Effects of signal diffusion on x-ray phase contrast images". In: *Review of Scientific Instruments* 82.7 (2011), p. 073702.

[26] Danail Ivanov et al. "Suitability of low density materials for 3D printing of physical breast phantoms". In: *Physics in Medicine & Biology* 63.17 (2018), p. 175020.

[27] Avinash C Kak, Malcolm Slaney, and Ge Wang. "Principles of computerized tomographic imaging". In: *Medical Physics* 29.1 (2002), pp. 107–107.

[28] Sunghwan Kim et al. "PubChem 2019 update: improved access to chemical data". In: *Nucleic acids research* 47.D1 (2018), pp. D1102–D1109.

[29] Lynn Kissel, B Zhou, SC Roy, SK Sen Gupta, and RH Pratt. "The validity of form-factor, modified-form-factor and anomalous-scattering-factor approximations in elastic scattering calculations". In: *Acta Crystallographica Section A: Foundations of Crystallography* 51.3 (1995), pp. 271–288.

[30] Anastasios Konstantinidis. "Evaluation of digital X-ray detectors for medical imaging applications". PhD thesis. UCL (University College London), 2011.

[31] C Kottler, F Pfeiffer, O Bunk, C Grünzweig, and C David. "Grating interferometer based scanning setup for hard x-ray phase contrast imaging". In: *Review of scientific instruments* 78.4 (2007), p. 043710.

[32] Simon Maretzke. "A uniqueness result for propagation-based phase contrast imaging from a single measurement". In: *Inverse Problems* 31.6 (2015), p. 065003.

[33] Simon Maretzke. "Regularized Newton methods for simultaneous Radon inversion and phase retrieval in phase contrast tomography". In: *arXiv preprint arXiv:1502.05073* (2015).

[34] TP Millard, M Endrizzi, K Ignatyev, CK Hagen, PRT Munro, RD Speller, and A Olivo. "Method for automatization of the alignment of a laboratory based x-ray phase contrast edge illumination system". In: *Review of Scientific Instruments* 84.8 (2013), p. 083702.

[35] Peter RT Munro, Luigi Rigon, Konstantin Ignatyev, Frances CM Lopez, Diego Dreossi, Robert D Speller, and Alessandro Olivo. "A quantitative, non-interferometric x-ray phase contrast imaging technique". In: *Optics express* 21.1 (2013), pp. 647–661.

[36] Peter RT Munro, Charlotte K Hagen, Magdalena B Szafraniec, and Alessandro Olivo. "A simplified approach to quantitative coded aperture x-ray phase imaging". In: *Optics express* 21.9 (2013), pp. 11187–11201.

[37] Peter RT Munro, Konstantin Ignatyev, Robert D Speller, and Alessandro Olivo. "Source size and temporal coherence requirements of coded aperture type x-ray phase contrast imaging systems." In: *Optics express* 18.19 (2010), pp. 19681–19692.

[38]   A Olivo and R Speller. "Experimental validation of a simple model capable of predicting the phase contrast imaging capabilities of any x-ray imaging system". In: *Physics in Medicine & Biology* 51.12 (2006), p. 3015.

[39]   A Olivo and R Speller. "Image formation principles in coded-aperture based x-ray phase contrast imaging". In: *Physics in medicine and biology* 53.22 (2008), p. 6461.

[40]   A Olivo and R Speller. "Modelling of a novel x-ray phase contrast imaging technique based on coded apertures". In: *Physics in Medicine & Biology* 52.22 (2007), p. 6555.

[41]   A Olivo, K Ignatyev, PRT Munro, and RD Speller. "Design and realization of a coded-aperture based x-ray phase contrast imaging for homeland security applications". In: *Nuclear Instruments and Methods in Physics Research Section A: Accelerators, Spectrometers, Detectors and Associated Equipment* 610.2 (2009), pp. 604–614.

[42]   Alessandro Olivo and Robert Speller. "A coded-aperture technique allowing x-ray phase contrast imaging with conventional sources". In: *Applied Physics Letters* 91.7 (2007), p. 074106.

[43]   Alessandro Olivo and Robert D Speller. "A novel x-ray imaging technique based on coded apertures making phase contrast imaging feasible with conventional sources". In: *Nuclear Science Symposium Conference Record, 2008. NSS'08. IEEE*. IEEE. 2008, pp. 1447–1450.

[44]   Xiaochuan Pan, Emil Y Sidky, and Michael Vannier. "Why do commercial CT scanners still employ traditional, filtered back-projection for image reconstruction?" In: *Inverse problems* 25.12 (2009), p. 123009.

[45]   G Pang, Wei Zhao, and JA Rowlands. "Digital radiology using active matrix readout of amorphous selenium: Geometrical and effective fill factors". In: *Medical physics* 25.9 (1998), pp. 1636–1646.

[46]   M Persson, D Bone, and Håkan Elmqvist. "Total variation norm for three-dimensional iterative reconstruction in limited view angle tomography". In: *Physics in Medicine & Biology* 46.3 (2001), p. 853.

[47]   Franz Pfeiffer, Timm Weitkamp, Oliver Bunk, and Christian David. "Phase retrieval and differential phase-contrast imaging with low-brilliance X-ray sources". In: *Nature physics* 2.4 (2006), p. 258.

[48]   Leonid I Rudin, Stanley Osher, and Emad Fatemi. "Nonlinear total variation based noise removal algorithms". In: *Physica D: nonlinear phenomena* 60.1-4 (1992), pp. 259–268.

[49]   A Ruhlandt, M Krenkel, M Bartels, and T Salditt. "Three-dimensional phase retrieval in propagation-based phase-contrast imaging". In: *Physical Review A* 89.3 (2014), p. 033847.

[50]   Adrian Sarapata et al. "Quantitative imaging using high-energy X-ray phase-contrast CT with a 70 kVp polychromatic X-ray spectrum". In: *Optics Express* 23.1 (2015), pp. 523–535.

[51]   Alex Sawatzky, Qiaofeng Xu, Carsten O Schirra, and Mark A Anastasio. "Proximal ADMM for multi-channel image reconstruction in spectral X-ray CT". In: *IEEE transactions on medical imaging* 33.8 (2014), pp. 1657–1668.

[52]   Troy A Scott Jr. "Refractive Index of Ethanol–Water Mixtures and Density and Refractive Index of Ethanol–Water–Ethyl Ether Mixtures." In: *The Journal of physical chemistry* 50.5 (1946), pp. 406–412.

[53]   Emil Y Sidky, Chien-Min Kao, and Xiaochuan Pan. "Accurate image reconstruction from few-views and limited-angle data in divergent-beam CT". In: *Journal of X-ray Science and Technology* 14.2 (2006), pp. 119–139.

[54]   David Stout. "Creating a whole body digital mouse atlas with PET, CT and cryosection images". In: *Mol. Imaging Biol.* 4.4 (2002), S27.

[55]   Zhou Wang, Alan C Bovik, Hamid R Sheikh, Eero P Simoncelli, et al. "Image quality assessment: from error visibility to structural similarity". In: *IEEE transactions on image processing* 13.4 (2004), pp. 600–612.

[56]   Timm Weitkamp, Ana Diaz, Christian David, Franz Pfeiffer, Marco Stampanoni, Peter Cloetens, and Eric Ziegler. "X-ray phase imaging with a grating interferometer". In: *Optics express* 13.16 (2005), pp. 6296–6304.

[57]   SW Wilkins, T Ei Gureyev, D Gao, A Pogany, and AW Stevenson. "Phase-contrast imaging using polychromatic hard X-rays". In: *Nature* 384.6607 (1996), p. 335.

[58]   Leslie Ying. "Phase unwrapping". In: *Wiley Encyclopedia of Biomedical Engineering* (2006).

[59]   Anna Zamir, Paul C Diemoz, Fabio A Vittoria, Charlotte K Hagen, Marco Endrizzi, and Alessandro Olivo. "Edge illumination X-ray phase tomography of multi-material samples using a single-image phase retrieval algorithm". In: *Optics Express* 25.10 (2017), pp. 11984–11996.

[60]   Anna Zamir, Charlotte Hagen, Paul C Diemoz, Marco Endrizzi, Fabio Vittoria, Yujia Chen, Mark A Anastasio, and Alessandro Olivo. "Recent advances in edge illumination x-ray phase-contrast tomography". In: *Journal of Medical Imaging* 4.4 (2017), p. 040901.

[61]   Anna Zamir, Marco Endrizzi, Charlotte K Hagen, Fabio A Vittoria, Luca Urbani, Paolo De Coppi, and Alessandro Olivo. "Robust phase retrieval for high resolution edge illumination x-ray phase-contrast computed tomography in non-ideal environments". In: *Scientific Reports* 6 (2016).

[62]   Wei Zhao and John A Rowlands. "X-ray imaging using amorphous selenium: Feasibility of a flat panel self-scanned detector for digital radiology". In: *Medical physics* 22.10 (1995), pp. 1595–1604.

[63]   Peiping Zhu et al. "Low-dose, simple, and fast grating-based X-ray phase-contrast imaging". In: *Proceedings of the National Academy of Sciences* 107.31 (2010), pp. 13576–13581.

Appendix A

Derivation of the derivatives

A.1 Adjoint operator of derivative with respect to δ

First, we start with the derivative of $\mathcal{I}$ with respect to δ – $\mathcal{I}'_\delta$. First, we denote the linear space in which δ and β resides as $\mathbb{U}$, and thus $\mathbb{U} = \mathbb{L}^2(\mathbb{R}^2)$. Also, let $\mathbb{V}$ denote the linear space that $\mathcal{I}$ maps to, and thus $\mathbb{V} = \mathbb{L}^2([0, 2\pi) \times \mathbb{R})$. Define $s \in \mathbb{U}$. When s is infinitely close to 0, based on the definition of derivative, we have

$$\mathcal{I}'_\delta(s) = \mathcal{I}(\beta, \delta + s) - \mathcal{I}(\beta, \delta). \tag{A.1}$$

The right-side of this equation can be expanded:

$$\mathcal{I}'_\delta(s) = \exp\left(-\frac{4\pi}{\lambda}\mathcal{H}(\beta)\right)\left[-\frac{l_{od}}{M}I'_{TC}(\Delta\xi)\mathcal{D}(s)\right]. \tag{A.2}$$

According to the definition of adjoint operator, for any vector $\epsilon \in \mathbb{V}$,

$$(\epsilon, \mathcal{I}'_\delta(s))_{\mathbb{V}} = (\mathcal{I}'^*_\delta(\epsilon), s)_{\mathbb{U}} \tag{A.3}$$

$$\text{Left} = \int_{\mathbb{V}} \epsilon[\mathcal{I}'_\delta(s)] \tag{A.4}$$

$$= \int_{\mathbb{V}} \epsilon \exp\left(-\frac{4\pi}{\lambda}\mathcal{H}(\beta)\right)\left[-\frac{l_{od}}{M}I'_{TC}(\Delta\xi_i)\mathcal{D}(s)\right] \tag{A.5}$$

$$= \int_{\mathbb{V}} y(Ds) = \int_{\mathbb{U}} (D^*y)s, \tag{A.6}$$

where

$$y = -\frac{l_{od}}{M}I'_{TC}(\Delta\xi)\exp\left(-\frac{4\pi}{\lambda}\mathcal{H}(\beta)\right)\epsilon. \tag{A.7}$$

The last step used the definition of adjoint operator D^*. As a result,

$$\mathcal{I}'^*_\delta(\epsilon) = D^*y = -\mathcal{D}^*\left[\frac{l_{od}}{M}I'_{TC}(\Delta\xi)\right]\exp\left(-\frac{4\pi}{\lambda}\mathcal{H}(\beta)\right)\epsilon. \tag{A.8}$$

A.2   Adjoint operator of derivative with respect to β

Similar to the previous section, let $s \in \mathbb{U}$. Again, for $\mathcal{I}'^*_\beta$, when s is infinitely close to 0, we have

$$\mathcal{I}'_\beta(s) = \mathcal{I}(\beta + s, \delta) - \mathcal{I}(\beta, \delta). \tag{A.9}$$

The right side can also be expanded:

$$\mathcal{I}'_\beta(s) = \mathcal{I}(\beta + s, \delta) - \mathcal{I}(\beta, \delta) \tag{A.10}$$

$$= -\frac{4\pi}{\lambda} \exp\left(-\frac{4\pi}{\lambda}\mathcal{H}(\beta)\right)\left[I_{TC}(\Delta\xi) - \frac{l_{od}}{M}I'_{TC}(\Delta\xi_i)\mathcal{D}(s)\right]\mathcal{H}(s) \tag{A.11}$$

$$= -\frac{4\pi}{\lambda}\mathcal{I}(\beta, \delta)\mathcal{H}(s). \tag{A.12}$$

According to the definition of adjoint operator, for any vector $\epsilon \in \mathbb{V}$,

$$(\epsilon, \mathcal{I}'_\beta(s))_{\mathbb{V}} = (\mathcal{I}'^*_\beta(\epsilon), s)_{\mathbb{U}} \tag{A.13}$$

$$\text{Left} = \int_{\mathbb{V}} \epsilon \mathcal{I}'_\beta(s) \tag{A.14}$$

$$= -\frac{4\pi}{\lambda}\int_{\mathbb{V}} \epsilon \mathcal{I}(\beta, \delta)\mathcal{H}(s) \tag{A.15}$$

$$= -\frac{4\pi}{\lambda}\int_{\mathbb{V}} x\mathcal{H}(s) = -\frac{4\pi}{\lambda}\int_{\mathbb{U}} \mathcal{H}^*(x)s \tag{A.16}$$

where

$$x = \mathcal{I}(\beta, \delta)\epsilon. \tag{A.17}$$

The last step used the definition of adjoint operator $\mathcal{H}^*$. As a result,

$$\mathcal{I}'^*_\beta(\epsilon) = -\frac{4\pi}{\lambda}\mathcal{H}^* x = -\frac{4\pi}{\lambda}\mathcal{H}^*\left[I_{TC}(\Delta\xi) - \frac{l_{od}}{M}I'_{TC}(\Delta\xi)\mathcal{D}(\delta)\right]\exp\left(-\frac{4\pi}{\lambda}\mathcal{H}(\beta)\right)\epsilon. \tag{A.18}$$

Appendix B

Proof the convexity of optimization problem for δ

For the subproblem of reconstructing $\boldsymbol{\delta}$ alone, we can simplify the notation for the forward model as:

$$\boldsymbol{I}_i(\boldsymbol{\beta}, \boldsymbol{\delta}) = a_i - b_i[\boldsymbol{D}\boldsymbol{\delta}]_i \ (i = 1, 2, ..., PQ), \tag{B.1}$$

where

$$a_i = \exp\left(-\frac{4\pi}{\lambda}[\boldsymbol{H}\boldsymbol{\beta}]_i\right) I_{TC}(\Delta\xi_i), \tag{B.2}$$

$$b_i = \exp\left(-\frac{4\pi}{\lambda}[\boldsymbol{H}\boldsymbol{\beta}]_i\right)\frac{l_{od}}{M}I'_{TC}(\Delta\xi_i) \ (i = 1, 2, ..., PQ), \tag{B.3}$$

are irrelevant of δ, so they can be regarded as constants.

Let

$$\boldsymbol{D} = [\boldsymbol{d}_1^T, \boldsymbol{d}_2^T, ..., \boldsymbol{d}_{PQ}^T]^T, \tag{B.4}$$

where vector $\boldsymbol{d}_i \in \mathbb{R}^{1 \times N}$ $(i = 1, 2, ..., PQ)$ is the i-th line of matrix $\boldsymbol{D}$. Then

$$b_i[\boldsymbol{D}\boldsymbol{\delta}]_i = b_i \boldsymbol{d}_i^T \boldsymbol{\delta}. \tag{B.5}$$

Construct $\boldsymbol{E}$ as

$$\boldsymbol{E} = [b_1 \boldsymbol{d}_1^T, b_2 \boldsymbol{d}_2^T, ..., b_{PQ} \boldsymbol{d}_{PQ}^T]^T. \tag{B.6}$$

Then the forward model can be written as

$$\boldsymbol{I}(\boldsymbol{\beta}, \boldsymbol{\delta}) = \boldsymbol{a} - \boldsymbol{E}\boldsymbol{\delta}. \tag{B.7}$$

As a result, the second-order derivative (Hessian matrix) of the cost function $f_{1\delta}(\boldsymbol{\delta})$ would be $\boldsymbol{E}^\dagger \boldsymbol{E}$. Because $\boldsymbol{E}$ is a linear operator, the Hessian matrix is positive semi-definite. Thus the subproblem is quadratic and convex.